8-1-2018

Large eddy simulations of ventilated micro-hydrokinetic turbine and pump-turbines

COSAN DASKIRAN
Lehigh University, cod213@lehigh.edu

Large eddy simulations of ventilated micro-hydrokinetic turbine and pump-turbines

by

Cosan Daskiran

A Dissertation

Presented to the Graduate and Research Committee

of Lehigh University

in Candidacy for the Degree of

Doctor of Philosophy

in

Mechanical Engineering

Lehigh University

(August 2018)

Approved and recommended for acceptance as a dissertation in partial fulfillment of the requirements for the degree of Doctor of Philosophy

Cosan Daskiran
Large eddy simulations of ventilated micro-hydrokinetic turbine and pump-turbines

_____
Defense Date

_____
Dissertation Director
Dr. Alparslan Oztekin

_____
Approved Date

Committee Members:

_____
Dr. Jacob Kazakia

_____
Dr. Natasha Vermaak

_____
Dr. Richard Weisman

ACKNOWLEDGMENTS

I would like to express my sincere appreciation to my advisor Dr. Alparslan Oztekin for his continuous support and guidance through my research. Without his help, this work would not have been possible. I am also grateful to my committee members, Dr. Jacob Kazakia, Dr. Natasha Vermaak, and Dr. Richard Weisman for their help in preparation of this dissertation. Thanks to my colleagues; Dr. William C. Schleicher, Dr. Jacob Riglin, Dr. I-Han Liu, Mr. Bashar Attiya and Mr. Muhannad Altimemy for their collaboration, encouragement, and companionship during my study at Lehigh University. Working with them as a team has helped me get through those difficult times in research. In addition, I would like to thank my wife for her unconditional love and support in my life.

TABLE OF CONTENTS

LIST OF TABLES

LIST OF FIGURES

NOMENCLEATURE

A	Area
B	Gate height
C	Molar concentration
C_D	Drag coefficient
$C_{D,b}$	Bubble drag coefficient
d_i	Inlet bubble diameter
d_S	Sauter mean bubble diameter
d_h	Hole diameter at sparger
D	Diffusion coefficient
D_{ref}	Reference diameter
DO	Dissolved oxygen
F_D	Drag force
F_{int}	Gas-liquid interfacial forces
H	Plate height
He	Henry constant
K	Adjustable parameter
k_l	Liquid side mass transfer coefficient
L	Plate length
M	Meridional length
M_{o_2}	Molar mass of oxygen

M_{H_2O}	Molar mass of water
$\dot{m}_{gl}$	Mass transfer from gas to liquid
$\dot{m}_{lg}$	Mass transfer from liquid to gas
n	Rotation speed
N	Number of cells
P	Partial pressure
p	Pressure
Q	Q-criterion
$\dot{Q}$	Flow rate
Re	Reynolds number
$\vec{S}$	Rate of the strain tensor
SGS	Sub-grid scale
Sc	Schmidt number
t	Time
T	Thrust
$\vec{U}$	Phase velocity
$\vec{U}_{gl}$	Interfacial velocity
u_t	Bubble fluctuation velocity
u_r	Bubble terminal velocity
w	Plate width
We	Weber number
$\times_i$	Position vector

x	Mass fraction
y	Mole fraction
y^+	Dimensionless wall distance

Greek Symbols

α	Volume fraction
α_{gmax}	Dense packing limit of volume fraction
α_i	Interfacial area concentration
β	Relative flow angle
β'	Blade angle
θ	Wrap angle
λ	Non-dimensional time
ε	Permutation symbol
μ	Dynamic viscosity
ν	Kinematic viscosity
ρ	Density
σ	Solidity
σ_s	Surface tension coefficient
ω	Vorticity
Ω	Rotation tensor
τ_{st}	Stress-strain tensor
$\widetilde{\omega}$	Normalized vorticity

Subscripts

cr	Critical
dr	Drift
g	Gas phase
g, l	Gas or liquid phase
i, j, k	Tensor indices
l	Liquid phase
m	Mixture
O_2, eq	Equilibrium property of oxygen in liquid phase
O_2, g	Property of oxygen in gas phase
O_2, l	Property of oxygen in liquid phase
Slip	Relative between phases
T	Turbulent
μ	Viscous
∞	Free-stream

ABSTRACT

Large eddy simulations of ventilated hydrokinetic turbine and pump-turbine are conducted. The mathematical modeling of oxygen dissolution and the flow model employed were validated by comparing predicted dissolved oxygen concentration against reported experimental measurements. A parametric study is performed to investigate the influence of interfacial forces, surface tension and bubble breakage and coalescence terms. It is demonstrated that aeration via hydrokinetic turbines can be used to improve the dissolved oxygen level in rivers for better water quality. It is also shown that aeration can effectively be achieved via the pump-turbine system to provide the desired dissolved oxygen level for the microorganisms' growth during the wastewater treatment process. Air injection is applied to the wake region of each unit. The influence of aeration on the turbine performance, flow induced vibration and oxygen dissolution characteristics are investigated. The numerical predictions reveal that the aeration can be utilized in both hydro systems without experiencing a significant penalty in power generations. Aeration significantly reduces the flow induced vibration in the pump turbine system. The pressure pulsation on the draft tube surface of the pump-turbine is reduced significantly with both central and peripheral aeration. In hydrokinetic turbine, the variation in the standard deviation of power, which is related to the vibration of the turbine unit, is strongly dependent on the turbine operating conditions. Draft tube aeration provided 30% greater amount of dissolved oxygen and 3.2 times higher dissolution efficiency inside the draft tube as compared to the central aeration. The mathematical approaches and the numerical

methods employed here can be used to design and optimize the aeration process in these systems.

CHAPTER 1 INTRODUCTION

Motivation

Water in rivers, lakes, reservoirs and underground aquifers are vitally important to the everyday life of people and ecological systems. Water quality is a major issue for the use of water for different purposes. The dissolved oxygen (DO) concentration in water is a critical indicator to determine the water quality. The low level of the oxygen concentration in water results in a significant influence on aquatic life including bacteria, fish, and plants. According to the criterion assigned by the United States Environmental Protection Agency, the dissolved oxygen level in water should not be less than 3 mg/l for fish survival [1].

The water passing through the hydro turbines in dams contains a low level of dissolved oxygen and is considered as the primary reason for decreased water quality in rivers. During the summer seasons, the water in the reservoirs are divided into different layers based on their DO content. The DO level decreases with the water depth. The layers closer to the free surface contain a higher DO level. Generally, the turbine intakes are located far away from the free surface, therefore the turbines discharge water with a low DO content. The most popular method to address this issue is to aerate water during the discharging process from the turbine. A total of 178 turbines at 58 hydropower facilities in the U.S. provide aeration [2].

Although low dissolved oxygen problems can be solved using ventilated hydro turbines, an only small portion of the dams in the U.S. involves aerating turbines. Another solution to enhance the dissolved oxygen in the water streams is to aerate water through

hydrokinetic turbines. Hydrokinetic turbines operate underwater and use the kinetic energy of streaming water to generate power. In the present study, the micro-hydrokinetic turbine is ventilated to mitigate the low dissolved oxygen concentration in rivers while the turbine is generating power at the same time.

The DO content is very important in the wastewater treatment process. Wastewater requires proper treatment before it is released back to the environment. The wastewater treatment process consists of two stages: a primary and secondary stage. In the primary stage, suspended solids are removed physically with screens and skimming. The secondary stage involves biological treatment in which the micro-organisms convert the organic compounds in the wastewater into inorganic compounds. This conversion produces energy that is good for micro-organism growth. The United States Environmental Protection Agency (EPA) states that almost 90% of the organic waste in wastewater is removed by the secondary stage [3]. The micro-organisms need dissolved oxygen (DO) in the wastewater during the treatment process to decompose the organic wastes.

Pump-turbines are typically used for energy storage in conjunction with intermittent energy sources, such as wind and solar power; allowing for uninterrupted power generation to the grid. In this study, in addition to energy storage, wastewater treatment is studied within a modular pump-turbine scheme. During the turbine regime as the wastewater is released from the upper reservoir to the lower reservoir, air injection will be applied over the pump-turbine to provide sufficient amount of dissolved oxygen for active aerobic bacteria activity during the wastewater treatment.

Literature Review

Previous numerical and experimental studies on multiphase flows including oxygen mass transfer from air to water have primarily focused on the prediction of bubble size distribution and dissolved oxygen concentration in the flow field. Several studies have considered bubble column reactors, stirred tanks and ventilated hydrofoils to observe the bubble size and oxygen absorption characteristics. Bubble column reactors are mostly used in chemical and biochemical industries for various applications such as dissolution, fermentation, and wastewater treatment. Jia et al. [4] and Zhou et al. [5] performed computational fluid dynamics (CFD) simulations to predict the bubble size and the mass transfer in a bubble column using Eulerian multiphase model and multiple-size group (MUSIG) bubble size model. They validated their mathematical model and the numerical method by comparing predicted results against their experimental measurements. The bubble diameter at a gas inlet boundary of a bubble column is studied experimentally by Akita and Yoshida [6]. They reported an empirical correlation of the bubble diameter as a function of the inlet gas velocity and the orifice diameter.

Similarly, stirred tanks are used to improve the dissolution performance through the momentum mixing of one or multiple impellers. Kerdouss et al. [7] conducted CFD simulations for a double impeller stirred tank to obtain the gas volume fraction and the bubble diameter in the tank. Their predictions agree well with experimental observations and numerical predictions. Smaller bubble size is observed around the impeller discharge as a result of a bubble breakup by small eddies induced by the impeller. CFD simulations of three-impeller agitators with a constant and a variable bubble diameter were carried out

by Min et al. [8]. They concluded that a single bubble size assumption which ignores the bubble breakup and the coalescence is not capable of capturing a local gas holdup in the stirred tank accurately. Their findings with the variable bubble diameter model are consistent with documented experimental measurements.

Recently, experimental analyses of a ventilated hydrofoil were performed in a closed loop water channel by Karn et al. [9, 10, 11, 12] to investigate bubble size characteristics and the dissolved oxygen level. Karn et al. [9] proposed a dispersion theory for the bubble size prediction and obtained reasonably good agreement with experimental observations within low air injection rate in the breakup dominated region. They observed that the bubble size is influenced by breakage effects in the near wake region and by coalescence effects in the far wake region. Karn et al. [11] studied the influence of the free stream velocity, the injected air flow rate, and the angle of attack of the hydrofoil on both the bubble size distribution and the oxygen mass transfer rate. They reported that Sauter mean bubble diameter depends strongly on the free stream water velocity. The influence of the air injection rate and the angle of attack ranging from 0° to 8° on the bubble size is not as strong. These investigators also reported their mass transfer analyses are applicable to similar bubbly flows. Moreover, their experiments reveal that an increase in water velocity results in a greater bubble breakup while an increase in air injection rate leads to a greater bubble coalescence in the hydrofoil wake region [12].

In addition to the experiments of the single ventilated hydrofoil, aeration is investigated for full hydro turbines to study the influence of air introduction on oxygen dissolution and turbine efficiency. As reported by March and Fisher [13] and March [14],

auto venting aeration technology is applied for two units at Norris Dam using different aerating methods as central, distributed and peripheral aeration. The study reveals that the single unit can increase the zero incoming DO level up to 5.5 mg/l with combined operation of aeration options. The typical turbine efficiency loss at Norris ranges from -0.2% to 4.0% and the impact of aeration on turbine efficiency from the highest to lowest is arranged as central, peripheral and distributed aeration. The auto-venting turbines at Bull Shoals, Norfolk and Table Rock Dams are modified to increase the amount of induced air for aeration purposes [15]. Following the site-specific modifications such as baffle installation, adding new air openings, adding air supply piping aid in increasing the induced air flow rate and improved the DO level up to 2-3 mg/l at Bull Shoals, 2.5-3 mg/l at Norfolk and 2-3 mg/l at Table Rock Dams with the single turbine operation. The influence of the modifications and resulted higher air flow rate on the turbine power generation was minimal.

Moore [16] describes the aeration system installation to three turbines at Lloyd Shoals Dam located in Georgia to meet the state DO criteria. The draft tube aeration provided the desired amount of DO level and the pre-installed aerating weir, which requires costly repairs, are removed. After the installation of aeration systems, a minor reduction in turbine efficiency is observed. The elevated DO level also decreased the dissolved manganese concentration in the river which otherwise needed to be removed during the water treatment process. Papillon et al. [17] provide experimental test results of central and peripheral turbine aeration. The air introduced from the center of the runner cone formed a central vortex core while the peripheral draft tube aeration technique provided well-

distributed, small-sized bubbles yielding higher oxygen dissolution rate. They also reported that the influence of the peripheral aeration on efficiency is much lower than that of central aeration.

In this study, aeration is applied to two different hydro turbine systems for different purposes. In hydrokinetic turbine simulations, the main goal of aeration is to mitigate the low dissolved oxygen problem in rivers. However, for pump-turbine, the main objective is to aerate the streaming water through the pump-turbine and treat the wastewater inside the draft tube. The well-known method for wastewater treatment is using oxidation ditches. As reported by Water Environment Federation, there are more than 9,200 oxidation ditches to treat the municipal wastewater in the United States [18]. Aeration can be provided to the oxidation ditches using floating brush rotors and disc aerators and submerged fine bubble diffusers [19]. Oxidation ditches offer several advantages such as less sludge production, cost-effectiveness, and simplicity [20]. However, they require a large settlement area and high energy input [21].

In addition to the environmental aspect of aeration, air injection benefits reducing the pressure pulsation inside the draft tube of hydro turbines. Several researchers studied the influence of air injection on pressure fluctuation experimentally [22, 23] and numerically [24, 25]. Turkmenoglu [22] reported more than 11% improvement in power generation and roughly 28% reduction in turbine vibration after the central aeration. Nakanishi and Tsuneo [23] provided the amplitude of pressure fluctuation at the draft tube inlet as a function of air flow rate for three different turbines. As the air flow rate exceeds a certain fixed value, the pulsation reduces suddenly, however introducing air flow higher

than needed causes efficiency reduction. They reported an optimum value for the air flow rate in the range of 1.5% to 2.5% of the total discharge from the turbine. The suppression of pressure fluctuation is achieved by aerating Francis turbine from the center of the main shaft by Yu et al. [24]. They injected air with different flow rates changing between 0.5% and 4.0% of water flow rate. The smallest air injection of 0.5% increases the amplitude of pressure fluctuation marginally compared against no aeration case. Major reduction in the amplitude of pressure fluctuation is observed with air injection rate of 4%. They also observed that the difference between the minimum and maximum pressure level on the monitoring section is reduced with air injection rate of 4.0%.

Objective

The primary goal of the present study is to investigate the effects of aeration on the turbine performance and the flow fields and reveal the dissolution characteristics of oxygen under various operating conditions. The mixture and Eulerian multiphase models and Reynolds-Averaged Navier Stokes (RANS) and Large Eddy Simulations (LES) turbulence models are employed to predict the flow field and dissolved oxygen concentration.

The design and off-design operating conditions are considered for the ventilating micro-hydrokinetic turbines. The primary goal with ventilated hydrokinetic turbine system is to improve the water quality through the dissolution of oxygen. The influence of air introduction on power generation, thrust force and standard deviations of these performance parameters is presented. Time-averaged contours of air volume fraction and dissolved oxygen concentration are depicted for various operating conditions.

For the pump-turbine, central aeration and two types of draft tube aeration are studied. The main goal of aeration is to provide sufficient amount of dissolved oxygen for microorganisms which convert organic wastes into inorganic compounds and desire dissolved oxygen during this process. The power generation with and without aeration is compared to reveal the effect of aeration on the pump-turbine performance. The predicted mean DO concentration and dissolution efficiency inside the draft tube are compared for different aeration methods. Moreover, the effect of aeration on pressure pulsation or relevant pump-turbine vibration is investigated. Spatial and temporal characteristics of the turbulent flow field are presented and discussed in detail.

CHAPTER 2 MATHEMATICAL MODEL

Turbulence Modeling

2.1.1 Reynolds Averaged Navier-Stokes Modeling, RANS

Menter's *k*-*ω* shear stress transport (*k*-*ω* SST) [26, 27] model is implemented as a RANS method to characterize the turbulent flow field. For multiphase flow of the dilute mixture, dispersed turbulence model equations, which are detailed in Ref. [28], are solved for the primary phase - liquid phase. Turbulence parameters of the secondary phase are not computed by solving turbulence transport equations. They are obtained through the Tchen theory of discrete particles dispersion by continuous turbulence [29]. The difference between standard *k*-*ω* SST model and dispersed model is the inclusion of additional terms of interfacial turbulent momentum transfer. The *k*-*ω* SST model is more effective to predict adverse pressure gradient near wall region than standard *k*-*ω* and *k*-*ε* models. The *k*-*ω* model performs better near solid boundaries while *k*-*ε* model is preferred for wake regions and free shear flows. The *k*-*ω* SST model combines the advantages of both *k*-*ω* model and *k*-*ε* model through the blending functions.

The equations for the eddy viscosity (ν_T), the turbulent kinetic energy (k), and the specific dissipation rate (ω) are shown below for k-ω SST model:

$$\nu_T = \frac{a_1 k}{\max(a_1\omega, \Omega F_2)} \tag{1}$$

$$\frac{\partial k}{\partial t} + u_j \frac{\partial k}{\partial x_j} = \tau_{ij} \frac{\partial u_i}{\partial x_j} - \beta^* k\omega + \frac{\partial}{\partial x_j}\left[(\nu + \sigma_k \nu_T)\frac{\partial k}{\partial x_j}\right] \tag{2}$$

$$\frac{\partial \omega}{\partial t} + u_j \frac{\partial \omega}{\partial x_j} = aS^2 - \beta\omega^2 + \frac{\partial}{\partial x_j}\left[(\nu + \sigma_\omega \nu_T)\frac{\partial \omega}{\partial x_j}\right] + 2(1 - F_1)\sigma_{\omega 2}\frac{1}{\omega}\frac{\partial k}{\partial x_i}\frac{\partial \omega}{\partial x_i} \quad (3)$$

Here, Ω is the vorticity magnitude, ν is the kinematic viscosity, , a_1, β, β^*, σ_k, σ_ω, σ_{ω_2} are model constants, S is the invariant measure of strain rate, and F_1 and F_2 are blending functions. Details of the *k-ω* SST turbulence model are explained by Wilcox [30].

2.1.2 Large Eddy Simulations, LES

For LES, a spatial filtering is applied to the Navier-Stokes equations. The momentum transfer induced by large eddies are resolved without modeling. Since the turbulent mixing of phases is induced mainly by larger eddies, LES turbulence model becomes desirable for multiphase flows.

The filtered form of the Navier-Stokes equations is written as follows:

$$\frac{\partial \bar{u}_j}{\partial x_j} = 0 \quad (4)$$

$$\frac{\partial \rho \bar{u}_i}{\partial t} + \frac{\partial \rho \bar{u}_j \bar{u}_i}{\partial x_j} = -\frac{\partial \bar{p}}{\partial x_i} - \frac{\partial \tau_{ij}}{\partial x_j} + \mu \frac{\partial^2 \bar{u}_i}{\partial x_j \partial x_j} + \rho g \quad (5)$$

Here, $\bar{u}_j = u_j - \acute{u}_j$ represents the filtered velocity vector, and $\bar{p}$ is the resolved pressure.

LES model resolves large scale eddies while eddies smaller than the cell size are modeled using the sub-grid-scale (SGS) model. The sub-grid-scale tensor, τ_{ij} appears in Eq.(5) because of SGS modeling. The wall-adapting local eddy-viscosity (WALE) method is used to model the turbulent SGS viscosity ν_t, which is given by Nicoud and Ducros [31]. The SGS turbulent stress is computed by employing the Boussinesq hypothesis as follows:

$$\tau_{ij} - \frac{1}{3}\tau_{kk}\delta_{ij} = -2\nu_t \bar{S}_{ij} \quad (6)$$

Here, δ_{ij} is the Kronecker delta; ν_t is the SGS eddy viscosity which is computed using WALE model below; and $\bar{S}_{ij} = \frac{1}{2}\left(\frac{\partial \bar{u}_i}{\partial x_j} + \frac{\partial \bar{u}_j}{\partial x_i}\right)$ is the rate-of-strain tensor.

$$\nu_t = L_s^2 \frac{\left(S_{ij}^d S_{ij}^d\right)^{3/2}}{\left(\bar{S}_{ij}\bar{S}_{ij}\right)^{5/2} + \left(S_{ij}^d S_{ij}^d\right)^{5/4}} \tag{7}$$

$$S_{ij}^d = \frac{1}{2}\left(\left(\frac{\partial \bar{u}_i}{\partial x_j}\right)^2 + \left(\frac{\partial \bar{u}_j}{\partial x_i}\right)^2\right) - \frac{1}{3}\delta_{ij}\left(\frac{\partial \bar{u}_k}{\partial x_k}\right)^2 \tag{8}$$

$$L_s = min\left(\kappa y, C_w \mathrm{V}^{1/3}\right) \tag{9}$$

Here, L_s represents the subgrid scales mixing length, κ represents the von Karman constant, y represents the shortest distance to the wall, C_w is the WALE constant which is 0.325, and V is the mesh cell volume. Details of the WALE model are documented by Nicoud and Ducros [31]"

Multiphase Model

2.2.1 The Eulerian and the Mixture Model

The multiphase Eulerian and the mixture models are two effective methods to simulate interpenetrating phases in the flow field. The mixture model is a simplified version of the Eulerian multiphase model. The mixture model utilizes averaged continuity and momentum equations to characterize the flow field of mixtures. The volume fraction equation of dispersed phase is solved to determine the distribution of each phase. Eulerian multiphase model employs the continuity and the momentum equation separately for each

phase to characterize the flow field. Therefore, the Eulerian model is more accurate, but it requires more computational resources compared to the mixture model.

2.2.1.1 The Eulerian Model

Mass and momentum conservation equations including mass transport between the phases are provided in Eqs. (10) and (11) [28].

The continuity equation for phase *a* is:

$$\frac{\partial}{\partial t}(\alpha_a \rho_a) + \nabla.\left(\alpha_a \rho_a \vec{U}_a\right) = \dot{m}_{ba} \tag{10}$$

where α_a, ρ_a, and $\vec{U}_a$ are the volume fraction, the density and the velocity of phase *a*, respectively. The term $\dot{m}_{ba}$ represents the mass transfer from phase *b* to phase *a*. Subscripts *a* and *b* denote liquid phase (*l*) or gas phase (*g*). The mass transferred from gas phase to liquid phase must be equal to the mass absorbed by liquid phase in order to prevent gas phase accumulation at the gas/liquid interface, which results in the following relation for the mass balance, $\dot{m}_{gl} = -\dot{m}_{lg}$. Liquid and gas phases share the same cell in proportion to the volume of each phase, therefore the relation $\alpha_l + \alpha_g = 1$ is satisfied.

The momentum equation for phase *a* is:

$$\frac{\partial}{\partial t}\left(\alpha_a \rho_a \vec{U}_a\right) + \nabla.\left(\alpha_a \rho_a \vec{U}_a \vec{U}_a\right) = -\alpha_a \nabla p + \nabla.\tau_{st,a} + \alpha_a \rho_a \vec{g} \pm \vec{F}_{int} + \dot{m}_{ba}\vec{U}_{ba} \tag{11}$$

where p is the pressure shared by both phases, $\tau_{st,a}$ is the stress-strain tensor of phase *a*, $\vec{g}$ is the gravitational acceleration, $\vec{F}_{int}$ is the interfacial forces between phase *a* and *b*, and $\vec{U}_{ba}$ is the interfacial velocity obtained as:

$\vec{U}_{ba} = \vec{U}_b$ for $\dot{m}_{ba} > 0$ (mass is transferred from phase *b* to phase *a*)

$\vec{U}_{ba} = \vec{U}_a$ for $\dot{m}_{ba} < 0$ (mass is transferred from phase *a* to phase *b*)

The lift coefficient model introduced by Tomiyama [32] and modified by Frank et al. [33] , the wall-lubrication model introduced by Antal et al. [34], the turbulent dispersion model introduced by De Bertodano [35] are used in the present study in addition to the drag coefficient model of Schiller and Naumann [36] to take interfacial forces between phases into account.

2.2.1.2 The Mixture Model

The mixture model can be used to simulate multiphase flows where the phases are allowed to move at different velocities by implementing the concept of slip velocities, while assuming local equilibrium over short spatial length scales. The mixture flow field is predicted by solving mixture continuity and mixture momentum equations. The mixture continuity equation used in this model is given by:

$$\frac{\partial \rho_m}{\partial t} + \nabla.\left(\rho_m \vec{U}_m\right) = 0 \tag{12}$$

where, $\rho_m = \sum_{k=g,l} \rho_k \alpha_k$ represents the mixture density and $\vec{U}_m = \frac{\sum_{k=g,l} \alpha_k \rho_k \vec{U}_k}{\rho_m}$ is the mass-averaged velocity. The mixture momentum equation implemented in this model is given by:

$$\frac{\partial (\rho_m \vec{U}_m)}{\partial t} + \nabla.\left(\rho_m \vec{U}_m \vec{U}_m\right) = -\nabla p + \nabla.\left[\tau_\mu + \tau_{dr}\right] + \rho_m \vec{g} \tag{13}$$

where, τ_μ represents the viscous stress tensor of the mixture, $\tau_{dr} = \alpha_g \rho_g \vec{U}_{dr} \vec{U}_{dr}$ is the drift stress tensor where $\vec{U}_{dr}$ is the drift velocity of the gas phase given by : $\vec{U}_{dr} = \vec{U}_g -$

$\vec{U}_m$. In this study, water is considered the primary phase, the injected air is considered the secondary phase.

The continuity equation for volume fraction of gas phase is solved as follows:

$$\frac{\partial}{\partial t}(\alpha_g \rho_g) + \nabla.(\alpha_g \rho_g \vec{U}_m) = -\nabla(\alpha_g \rho_g \vec{U}_{dr}) - \dot{m}_{gl} \quad (14)$$

In the above equation, $\dot{m}_{gl}$ represents the mass transfer from gas phase to liquid phase. The mixture model solves algebraic equations to evaluate the relative (slip) velocity between the phases. The slip velocity between the water and the injected air is calculated through the model introduced by Manninen et al. [37]. The algebraic equations for the slip velocity and the drift velocity are detailed in [37, 38].

2.2.2 Bubble Size Prediction – Interfacial Area Concentration (IAC)

The prediction of the local bubble size represents a very crucial part in the gas/liquid mass transfer calculations at the interface and the interfacial momentum exchange between two phases. Different models are available to accurately calculate the bubble size. A constant bubble diameter inside the flow field is considered as a low fidelity model. To obtain a higher accuracy, the population balance model (PBM) solves transport equation(s) that includes both sink and source terms to account for the breakage and the coalescence phenomenon. The two most widely used PBM based models are the single-group average bubble number density (ABND) model and the multiple-size group (MUSIG) model. However, the usage of MUSIG method require higher computational resources when compared to the ABND method and this is due to the fact that the transport equation must be solved for each bubble size group when the MUSIG method is used.

The bubble size in the present study is predicted using interfacial area concentration (IAC) model. The similar to BND model, the IAC model solves one conservation equation for the interfacial area concentration. The IAC transport equation with the sink and the source term is developed by Hibiki and Ishii [39] and Wu et al. [40] to predict the bubble size in a vertical bubble column. The validation of the proposed model is accomplished by Wu et al. [40] comparing against experimental results.

The interfacial area concentration, α_i, is defined in Eq. (15). α_i is a function of the gas phase volume fraction, α_g, and the Sauter mean bubble diameter, d_S. The Sauter mean bubble diameter is described as the diameter of a sphere that has the same volume to surface area ratio with the corresponding bubble.

$$\alpha_i = \frac{6\alpha_g}{d_S} \tag{15}$$

The transport equation of the interfacial area concentration for the gas phase can be written as follows [28]:

$$\frac{\partial(\rho_g \alpha_i)}{\partial t} + \nabla . \left(\rho_g \vec{U}_g \alpha_i\right) = \frac{2}{3}\frac{\dot{m}_{lg}}{\alpha_g}\alpha_i + \rho_g(Si_{RC} + Si_{WE} + So_{TI}) \tag{16}$$

The first term on the right-hand side of the Eq. (16) accounts for the effect of the mass transfer. $\dot{m}_{lg}$ is the mass transfer rate into the gas phase. Si_{RC} and Si_{WE} are coalescence terms for a random collision and a wake entrainment and So_{TI} is the breakage term for the turbulent impact modeled by Wu et al. [40] and Ishii and Kim [41]. In this approach, the turbulence intensifies random collision between bubbles resulting in coalescence. Furthermore, the acceleration of a bubble in the wake of a leading bubble may yield a collision and a coalescence. The bubble breakage occurs as a result of the eddy-

bubble collision. Equations for random collision, wake entrainment, and turbulent impact are given by:

$$Si_{RC} = -\frac{1}{3\pi} K_{RC} u_t {\alpha_i}^2 \left[\frac{1}{{\alpha_{gmax}}^{\frac{1}{3}}({\alpha_{gmax}}^{\frac{1}{3}} - {\alpha_g}^{\frac{1}{3}})}\right]\left[1 - \exp(-K\frac{{\alpha_{gmax}}^{\frac{1}{3}}{\alpha_g}^{\frac{1}{3}}}{{\alpha_{gmax}}^{\frac{1}{3}} - {\alpha_g}^{\frac{1}{3}}})\right] \quad (17)$$

$$Si_{WE} = -\frac{1}{3\pi} K_{WE} u_r {\alpha_i}^2 {C_{D,b}}^{1/3} \quad (18)$$

$$So_{TI} = \frac{1}{18} K_{TI} u_t \frac{{\alpha_i}^2}{\alpha_g}(1 - \frac{We_{cr}}{We})^{1/2}\exp(-\frac{We_{cr}}{We}) \quad (19)$$

where Weber number is defined by

$$We = \frac{\rho_l u_t^2 d_S}{\sigma_s} \quad (20)$$

Here, K_{RC}, K_{WE}, K_{TI} and K are adjustable parameters, u_t is the bubble fluctuation velocity, u_r is the bubble terminal velocity, $C_{D,b}$ is the bubble drag coefficient, σ_s is the surface tension coefficient, α_{gmax} is the dense packing limit of volume fraction for cases that have approximately infinite coalescence rate, and We_{cr} is the critical Weber number that is assumed to be 2.3 for air-water flow [42]. The turbulent impact breakage rate, So_{TI} equals zero when $We < We_{cr}$.

2.2.3 Oxygen Dissolution Modeling

Both liquid and gas phase consist of two components: the liquid phase including oxygen and water and the gas phase including oxygen and nitrogen. Imposing the conservation of mass, the sum of mass fractions for each phase must be equal to unity. The density and the dynamic viscosity of each phase is approximated by the volume-weighted-

mixing law and mass-weighted-mixing law, respectively. The phase density is calculated as $\rho_{g,l} = \frac{1}{\sum_n \frac{x_n}{\rho_n}}$ and the phase dynamic viscosity is computed as $\mu_{g,l} = \sum_n x_n \mu_n$, where x_n is the mass fraction, ρ_n is the density, and μ_n is the dynamic viscosity of species n.

The mass fraction of oxygen in both phases is determined by solving the mass transport equation of species. At t = 0, the mass fraction of oxygen in the liquid phase ($x_{O_2,l}$) is 0 and the mass fraction of oxygen in the gas phase ($x_{O_2,g}$) is 0.233. The mass transport equations for oxygen in both phases are written as follows:

$$\frac{\partial}{\partial t}\left(\alpha_l \rho_l x_{O_2,l}\right) + \nabla.\left(\alpha_l \rho_l \vec{U}_l x_{O_2,l}\right) = \nabla.\left[\alpha_l\left(\rho_l D_{O_2,l}\right)(\nabla x_{O_2,l})\right] + \dot{m}_{gl} \tag{21}$$

$$\frac{\partial}{\partial t}\left(\alpha_g \rho_g x_{O_2,g}\right) + \nabla.\left(\alpha_g \rho_g \vec{U}_g x_{O_2,g}\right) = \nabla.\left[\alpha_g\left(\rho_g D_{O_2,g}\right)(\nabla x_{O_2,g})\right] - \dot{m}_{gl} \tag{22}$$

Here, $D_{O_2,l}$=1.9×10^{-9} m^2/s is the mass diffusion coefficient of oxygen in the liquid phase, $D_{O_2,g}$=1.98×10^{-5} m^2/s is the mass diffusion coefficient of oxygen in the gas phase [43]. Sc_T=0.7 is the turbulent Schmidt number which appears in filtered form of the equation, and $\dot{m}_{gl}$ is the oxygen mass transfer from the gas phase to the liquid phase. The mass diffusion coefficient of oxygen in each phase is assumed to be constant and independent of the phase composition during the mass transfer process.

The oxygen mass transfer between phases is modeled through the modified version of two-film theory [44] for low soluble gases. The liquid film has relatively high resistance against the mass transfer due to lower solubility of oxygen in water and greater oxygen diffusivity in air [45]. As a result, the oxygen mass transfer is dominated by the mass

transfer coefficient on the liquid side. The equation governing the transferred mass is given by

$$\dot{m}_{gl} = k_l \alpha_i M_{o_2} (C_{O_2,eq} - C_{O_2,l}) \tag{23}$$

where, k_l is the mass transfer coefficient in the liquid side, M_{o_2} is the molar mass of the oxygen and $C_{O_2,l}$ is the molar concentration of the oxygen within the liquid phase. The equilibrium molar concentration of oxygen within the liquid phase, $C_{O_2,eq}$ is evaluated by using the following equation.

$$C_{O_2,eq} = y_{O_2,eq} C_{eq} \tag{24}$$

where

$$y_{O_2,eq} = \frac{P_{O_2,g}}{He} \tag{25}$$

where, $y_{O_2,eq}$ stands for the oxygen equilibrium molar fraction within the liquid phase which is computed through Henry's law, as shown in Eq. (25). C_{eq} represents the total molar concentration of all given species within the liquid phase at the equilibrium state, $P_{O_2,g}$ represents the partial oxygen pressure within the gas phase, and finally He stands for the Henry's constant and it has a fixed value of 4.357 GPa at 25 ℃ [46].

Higbie' s penetration theory [47] and Danckwert' s surface renewal model [48] are common theories that are used to calculate the mass transfer coefficient. Ranganathan and Sivaraman [49] considered various models to determine the mass transfer coefficient in a gas-liquid stirred tank. Predicted values of the mass transfer coefficient are compared to prior experimental measurements [50]. It is demonstrated that Higbie's penetration theory and Danckwert's surface renewal model combined with the surface renewal rate model of

Lamont and Scott [51] agrees reasonably well with experimental results. Gimbun et al. [52] provided normalized dissolved oxygen rate in a stirred tank as a function of time by using aforementioned penetration and surface renewal theory. They reported that the surface renewal model predicts higher volumetric mass transfer coefficient ($k_l\alpha_i$) around an impeller due to higher turbulent dissipation rate in this region. On the other hand, the penetration theory predicts higher $k_l\alpha_i$ for regions far away from the impeller where the dissipation rate is low.

In the present study, Higbie' s penetration theory combined with Calderbank [53]'s contact time assumption based on the slip velocity and the bubble size is used to calculate the mass transfer coefficient by employing the following equation:

$$k_l = \frac{2}{\sqrt{\pi}}\sqrt{\frac{D_{O_2,l}U_{slip}}{d_S}} \tag{26}$$

Here, $U_{slip} = \left|\vec{U}_g - \vec{U}_l\right|$ is the magnitude of the relative velocity between the gas phase and the liquid phase. The volumetric mass transfer coefficient ($k_l\alpha_i$) is implemented into the CFD software through the user defined functions (UDF), see Appendix for UDF.

CHAPTER 3 VALIDATION OF OXYGEN DISSOLUTION MODEL – PARAMETRIC STUDY

This chapter focuses on the validation of oxygen dissolution model by comparing numerical predictions in a bubble column to prior experimental measurements reported by Zhou et al. [5]. Following the validation, a parametric study is conducted to reveal the influence of interfacial forces, surface tension and bubble breakage and coalescence terms. The parametric study is conducted by injecting air over the surfaces of submerged, translating blade. The parametric study is conducted in two-dimensional geometry. Gas-liquid flow in the validation and the parametric study is modeled by employing the Eulerian multiphase model, and the turbulence structure is modeled by using k-ω SST turbulence model. It is also presented here oxygen dissolution characteristics in three-dimensional geometries of a single blade and an array of blades with free ends. Mixture multiphase model with LES turbulence model is employed for three-dimensional transient simulations. The results presented in this chapter are published in Ref. [54].

Validation of the oxygen dissolution model

In order to validate the mathematical model and the numerical method, transient simulation is conducted in a three-dimensional bubble column using RANS-Eulerian model. Predicted results for the dissolved oxygen concentration are compared against experimental results documented by Zhou et al. [5]. Zhou et al. [5] conducted measurements in a bubble column having a square cross-section of 0.2 m by 0.2 m and the height of 1.2 m. Dimensions of the computational domain match with dimensions of the

bubble column used in the experiment. Air is introduced from a distribution plate centered at the bottom of the column. The distribution plate has dimensions of 0.05 m by 0.05 m.

The average of the area-averaged dissolved oxygen concentration calculated at the cross sections 0.3 m and 0.5 m away from the inlet is determined, and it is plotted as a function of time in Figure 1. These cross-sections are where DO sensors are located in the experiment. The evolution of the dissolved oxygen concentration predicted here agrees well with that measured by Zhou et al. [5] at the early stage of the aeration. At the later stage of the process, however, there is a difference in the predicted and the measured dissolved oxygen level. The average value of the dissolved oxygen concentration at t = 150 s is predicted to be 8.64 mg/l, but it is measured to be 7.2 mg/l [5]. At this instant, the oxygen level in experiments reaches nearly the equilibrium value. Based on the temperature (20 ºC) and the pressure (1 atm) selected, the equilibrium value for the simulation is about 9.55 mg/l [55]. On the other hand, the experimentally observed equilibrium value is indicating that it is roughly 7.5 mg/l. There is a wide range of variation in the equilibrium oxygen level for the given temperature and pressure [55, 56, 57]. In order to achieve a good agreement between the predicted dissolved oxygen level and the measured level documented in [5] at later stages of the aeration, we must select the equilibrium dissolved oxygen level close to 7.5 mg/l. There could be several other factors possibly contributing to the difference observed in the dissolved oxygen level. Zhou et al. [5] documented that the room temperature is not well controlled during the experiment. The equilibrium value of the dissolved oxygen is very sensitive to the temperature selected; i.e. the equilibrium value is reduced to 8.67 mg/l as the temperature is increased to 25 ºC

[55]. Furthermore, Zhou et al. [5] reported that the dissolved oxygen level in the column reduces slightly during the experiment due to substrate and biomass consumption which is not considered in the simulation. It is important to note that the time evolution of the dissolved oxygen, as shown in Fig 2, is very similar to that reported in [5]. These results presented here validate the oxygen dissolution model.

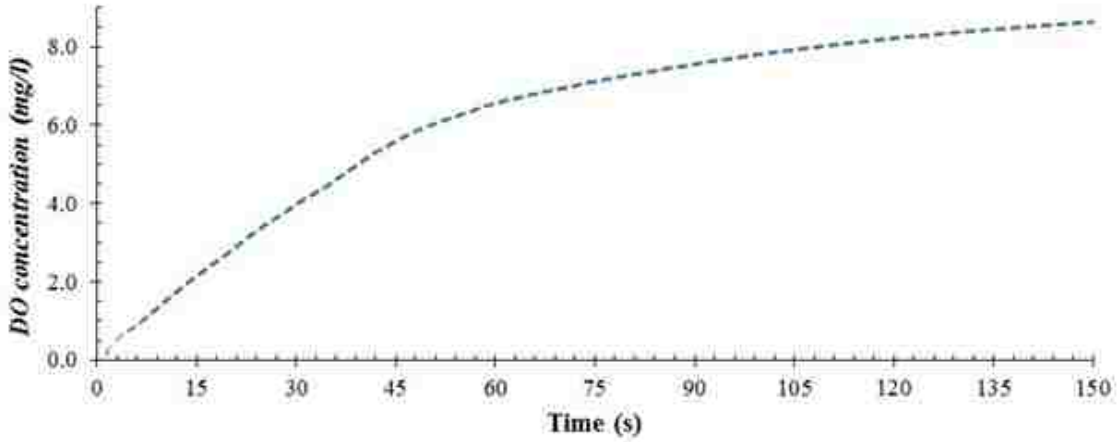

Figure 1. Predicted dissolved oxygen concentration as a function of time in the bubble column.

Parametric Study – Ventilated Translating Blades

3.2.1 Numerical methodology and computational domain

Reynolds-averaged Navier-Stokes (RANS) and LES turbulence model are employed to conduct CFD simulations in two-dimensional and three-dimensional geometries, respectively. Pressure-velocity coupling is applied by using a pressure based coupled solver (Coupled) in two-dimensional domains, and by using a pressure based segregated solver (SIMPLE) in three-dimensional domains. Numerical simulations are performed by employing the pressure staggering option (PRESTO!) scheme for the pressure correction. The second order upwind scheme is used to calculate turbulence

parameters, the interfacial area concentration and species' transports, while the QUICK scheme is used to discretize the volume fraction. The discretization of momentum equation is achieved with the second-order upwind scheme in two-dimensional domains and the bounded central differencing scheme is applied to discretize momentum equation in three-dimensional domains.

Computational domains are depicted in Figure 2. Figure 2(a) shows the front view of the three-dimensional flow geometry. Figure 2(b) shows the side view of the two-dimensional and the three-dimensional computational domain. Figure 2(c) presents the top view of multiple yawed plates in a staggered arrangement with the yaw angle of 45º. The gas phase inlet is colored with red in Figure 2(c). Plates in three-dimensional analyses have a finite length of $10H$ in the span-wise direction. The single plate is placed perpendicular to the flow direction and it is located $12H$ away from the inlet boundary to allow the turbulent flow to be fully developed. The outlet boundary is placed at $23H$ away from the plate. For flows past multiple yawed plates, as shown in Figure 2(c), the distance from the inlet to the closest upstream plate is $10H$ and from the outlet to the closest downstream plate is $36H$ to prevent the influence of outlet boundary conditions on the flow field near plates. The distance between the top and the bottom boundary of computational domains is $16H$. The distance between plate ends and side boundaries in the span-wise direction is $3H$ in a single plate case and $6H$ in a multiple yawed plate case. Side boundaries are located far away from the plate to minimize the effect of the boundary on the near wake velocity and the concentration fields.

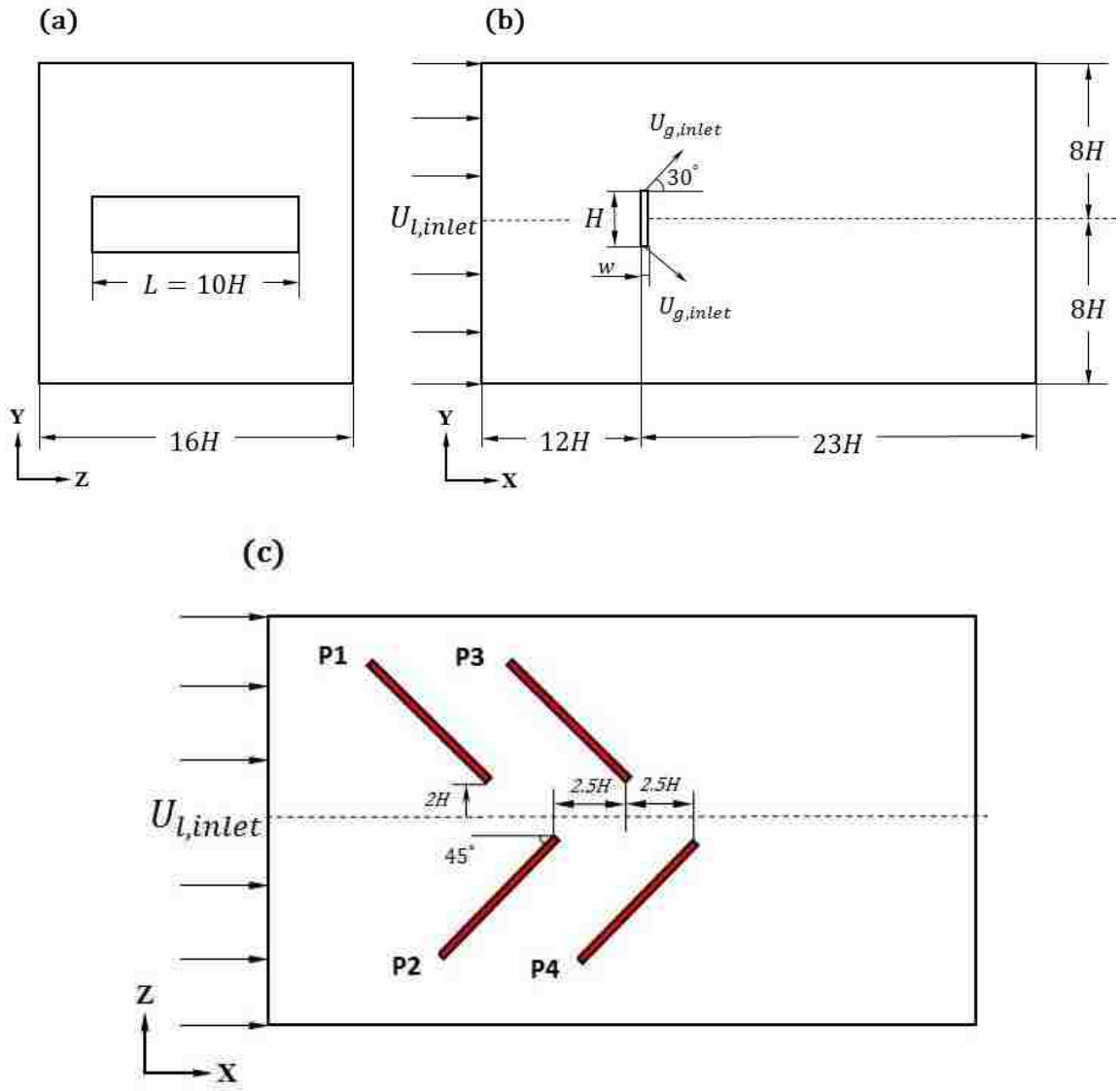

Figure 2. (a) Front view and (b) side view of the single plate computational domain. (c) Top view of the multiple yawed plate configuration.

At the inlet of the computational domain, a uniform velocity $U_{l,inlet}$=0.5 m/s is applied with a turbulent intensity of 2.9% for RANS simulations. At the outlet, outflow boundary condition that assigns zero gradient condition normal to the outlet boundary for all flow variables except for the pressure, is applied. Air is injected with the flow rate of $\dot{Q}_{g,inlet}$=7.5×10^{-5} m^3/s at the top and the bottom surfaces of each plate with an angle of 30^o

to the primary flow direction of water, as shown in Figure 2(b). No-slip boundary condition is imposed at the top and the bottom surfaces of the computational domain and at the sides of the plate. The symmetry boundary condition is applied at side boundaries of the computational domain. Parameters used in the present study and the geometric details shown in Figure 2(c) are listed in Table 1, where ρ is the density and μ is the dynamic viscosity of oxygen-gas (O_2, g), nitrogen-gas (N_2, g), oxygen-liquid (O_2, l) and water-liquid (H_2O, l).

Table 1. Parameters used in the simulations.

Parameter	***Value***	***Unit***						
$\boldsymbol{w}$	0.01	[m]	$\boldsymbol{\rho_{O_2,g}}$	1.300	[kg/m^3]	$\boldsymbol{\mu_{O_2,g}}$	1.919×10^{-5}	[kg/ms]
$\boldsymbol{H}$	0.1	[m]	$\boldsymbol{\rho_{N_2,g}}$	1.138	[kg/m^3]	$\boldsymbol{\mu_{N_2,g}}$	1.663×10^{-5}	[kg/ms]
$\boldsymbol{L}$	1	[m]	$\boldsymbol{\rho_{O_2,l}}$	1,142	[kg/m^3]	$\boldsymbol{\mu_{O_2,l}}$	1.958×10^{-4}	[kg/ms]
$\boldsymbol{Re}$	50,000	[-]	$\boldsymbol{\rho_{H_2O,l}}$	998.2	[kg/m^3]	$\boldsymbol{\mu_{H_2O,l}}$	1.003×10^{-3}	[kg/ms]

The bubble diameter needs to be calculated at the gas inlet, a sparger surface including holes. The bubble diameter at the inlet is determined from a correlation by assuming a hole size of the sparger. The hole diameter is assumed to be 1 mm in the present study. The correlation for the inlet bubble size is proposed by Miyahara et al. [58]. For the present study, $\frac{d_h U_{g,inlet} \rho_l g^{0.5}}{\sigma} \leq 1$. Here d_h is the hole diameter at the sparger and $U_{g,inlet}$ is the air velocity at the inlet. The bubble diameter then is calculated by:

$$d_i = 2.9 \left[\frac{\sigma d_h}{g \rho_l}\right]^{1/3} \tag{27}$$

At the gas inlet, the bubble diameter is determined to be 5.56 mm. Inside the flow field, the bubble diameter is calculated at each time step using the interfacial area concentration equation and is assumed to be in the range of 1 mm to 15 mm.

Simulations utilizing RANS and LES are carried out at Reynolds number of 50,000. *Re* is defined by

$$Re = \frac{\rho_l U_{l,inlet} H}{\mu_l} \tag{28}$$

where $U_{l,inlet}$ is the free stream velocity of liquid phase, H is the plate height and μ_l is the dynamic viscosity of liquid phase.

3.2.2 Spatial and Temporal Convergence Study – Two-dimensional Analysis

Spatial and temporal convergence study is carried out in a two-dimensional computational domain. The domain is discretized using hexahedral cells. A refined mesh is used in regions near the plate and the wake to capture the flow structure inside the boundary layer, flow separation, and the vortex shedding phenomena. For numerical simulations of multiphase flows including bubbles, the limitation on the cell size should be taken into consideration. Milelli et al. [59] demonstrated that the cell size for LES simulations must be at least 1.5 times the bubble size (Milelli condition) for accurate results. Similarly, Law et al. [60] showed that the RANS simulations produce unrealistic solutions when the bubble diameter exceeds the cell size. This restriction in the cell size is considered in the discretization process.

The mesh optimization study is conducted by refining the mesh in regions near the plate and the wake. The total number of elements used in three meshes for the spatial

convergence study are: $N_1 = 99{,}200$, $N_2 = 138{,}080$, and $N_3 = 159{,}840$. The averaged y^+ values calculated on the plate surface for N_1, N_2 and N_3 are 7.2, 5.4, and 3.3, respectively. The corresponding drag coefficients are calculated to be 3.59, 3.80 and 3.84, respectively. The drag coefficient is defined as $C_D = 2F_D/(\rho_l A U_{l,inlet}^2)$ where F_D is the drag force acting on the plate and A is the area projected perpendicular to the direction of free stream. The deviation in C_D obtained by N_1 and N_2 is 5.6%, while the difference is 1.1% between C_D obtained by N_2 and N_3. It is illustrated here that $N_3 = 159{,}840$ is sufficient to attain a spatial convergence.

Temporal convergence study is performed using non-dimensional time steps of 0.016, 0.008, and 0.004 with the grid size N_3. Non-dimensional time step and non-dimensional flow time are described as $\Delta\lambda = \Delta t U_{l,inlet}/H$ and $\lambda = t U_{l,inlet}/H$, respectively, where Δt is the time step and t is the flow time. The drag coefficient predicted for three time steps mentioned above is 3.97, 3.86 and 3.84, respectively. It is shown that non-dimensional a time step of 0.008 or smaller is adequate to attain a temporal convergence. Simulations here are conducted using a non-dimensional time step of 0.004.

3.2.3 Parametric Study

There are various types of interfacial momentum exchange forces between phases: the drag force, the lift force, the wall-lubrication force, and the turbulent dispersion force. As pointed out by Kerdouss et al. [7] and Gimbun et al. [52], the drag force, which is proportional to the relative velocity between phases, is typically a dominant interfacial force between phases. In order to determine the influence of interfacial forces on the power

generation and the aeration, two sets of simulations are conducted: one considers the drag force as the only interfacial force, the other one includes all four interfacial forces. The averaged dissolved oxygen concentration inside the channel and the averaged drag coefficient predicted are compared between the two sets of simulations using mesh grid size, $N_1 = 99{,}200$ cells. The averaged dissolved oxygen concentration is increased slightly from 2.11×10^{-3} mg/l to 2.19×10^{-3} mg/l, and the drag coefficient is increased from 3.59 to 3.65 with the addition of non-drag interfacial forces. It is clear that the lift, the wall-lubrication , and the turbulent dispersion forces have little influence on the aeration characteristics and the drag force. Results presented here are obtained by considering the drag as the only interfacial force between phases to minimize the computational time and to prevent the numerical instability.

The effect of coalescence and the breakage on mass transfer characteristics and the drag coefficient of the plate is investigated next. Simulations are conducted for three cases: the constant bubble diameter, the variable bubble diameter without the breakage and the coalescence effects (WOBC), and the variable bubble diameter with the breakage and the coalescence effects (WBC). The bubble diameter in certain areas exceeds the cell size while using the mesh grid $N_3 = 159{,}840$ resulting in divergence due to the cell size limitation mentioned above. In order to avoid such problems, simulations in this part are conducted with the mesh $N_1 = 99{,}200$ cells.

Figure 3 depicts the drag coefficient and the dissolved oxygen concentration as a function of non-dimensional time for three cases. The averaged drag coefficients are predicted to be 3.59, 3.71, and 3.64, and the averaged dissolved oxygen concentration in

the channel is determined to be 2.11×10^{-3} mg/l, 1.58×10^{-3} mg/l, and 1.61×10^{-3} mg/l for constant bubble size, variable bubble size WOBC and variable bubble size WBC, respectively. The drag coefficient for the single-phase flow is also depicted in Figure 3(a) as a reference. The averaged drag coefficient is calculated to be 3.66. The time signature of the drag coefficient obtained by multiphase flow simulations is similar to that of single-phase flow simulation. The amount of dissolved oxygen predicted with the constant bubble size assumption is significantly higher compared to that predicted with variable bubble size. The combined effects of flow field and mass transfer modeled through the interfacial area concentration have a significant influence on the level and dynamics of the dissolved oxygen, as shown in Figure 3(b) and 3(c). It is also important to note that the bubble breakage and the coalescence effects have a little influence on the dissolved oxygen level and the drag coefficient, see Figure 3(c) and 3(d).

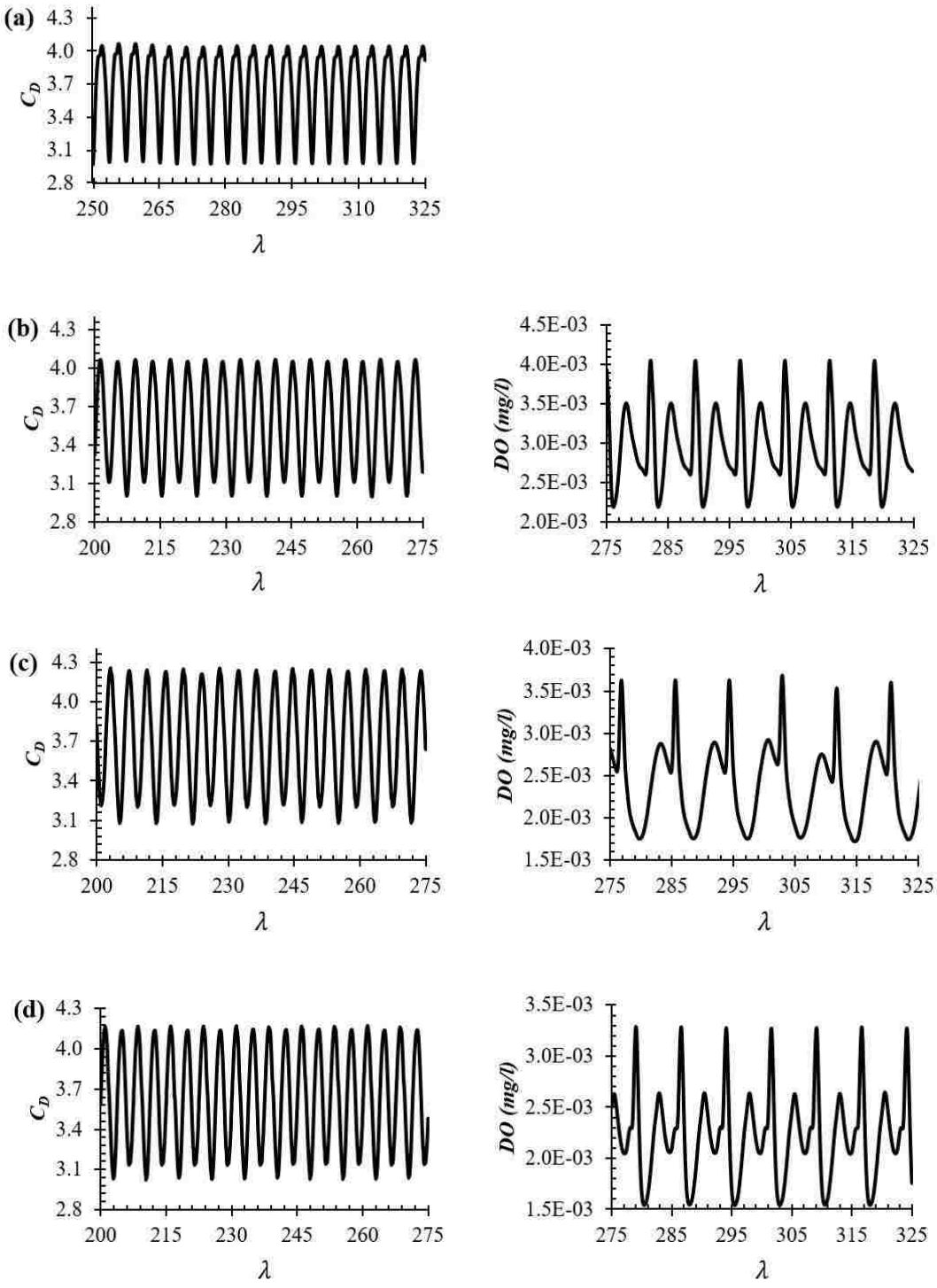

Figure 3. Drag coefficient (left column) and line-averaged dissolved oxygen concentration at $10H$ downstream of the plate (right column) as a function of non-dimensional time for the case of (a) single-phase, (b) constant bubble size and (c)-(d) variable bubble size without/with breakage and coalescence, respectively.

In addition to the effects of interfacial forces and the breakage and the coalescence, the influence of the surface tension on the averaged drag coefficient and the averaged dissolved oxygen concentration is investigated. The surface tension is modeled through the continuum surface force approach proposed by Brackbill et al. [61]. The averaged drag coefficient is changed less than 1% and the averaged dissolved oxygen concentration using WBC is hardly changed when the surface tension is included. For the sake of simplification, the effect of surface tension is neglected in the present study.

The influence of variable bubble size and the breakage/coalescence on the flow field is not strong. Two-dimensional flow field predicted by the single-phase model and the multiphase model with constant bubble diameter is depicted in Figure 4. Contours of instantaneous velocity, pressure, and vorticity field are compared in Figure 4 for *Re* = 50,000 at $\lambda = 274$. The pressure field of the mixture, the velocity and vorticity field of the liquid phase are illustrated in Figure 4. The velocity, the pressure, and the vorticity are normalized as follows:

$$\widetilde{U} = \frac{\left|\vec{U}\right|}{U_{l,inlet}} \tag{29}$$

$$\tilde{p} = \frac{p - (p_{min})}{p_{max} - p_{min}} \tag{30}$$

$$\widetilde{\omega} = \frac{\left|\varepsilon_{ijk}\frac{\partial U_k}{\partial \times_j}\right| H}{U_{l,inlet}} \tag{31}$$

where $\widetilde{U}$ is the normalized velocity magnitude, $\tilde{p}$ is the normalized static pressure excluding hydrostatic pressure, and $\widetilde{\omega}$ is the normalized vorticity magnitude. p_{min} and p_{max} are the minimum and maximum static pressure, respectively, for cases presented in

Figure 4(b). Images on the left column depict the flow field predicted by the single-phase model while images on the right column depict the flow field predicted by the multiphase model. There is no discernible difference in the flow field except at the near wake of the plate. Velocity, pressure, and vorticity field in the near wake region are influenced slightly by the introduction of air and the dissolution of the oxygen, as illustrated in Figure 4. Vortex shedding patterns and the induced flow field are similar in both single and multiphase flow, as evidence by the velocity and the vorticity field. That explains the weak influence of the aeration on the drag coefficient, as shown in Figure 3.

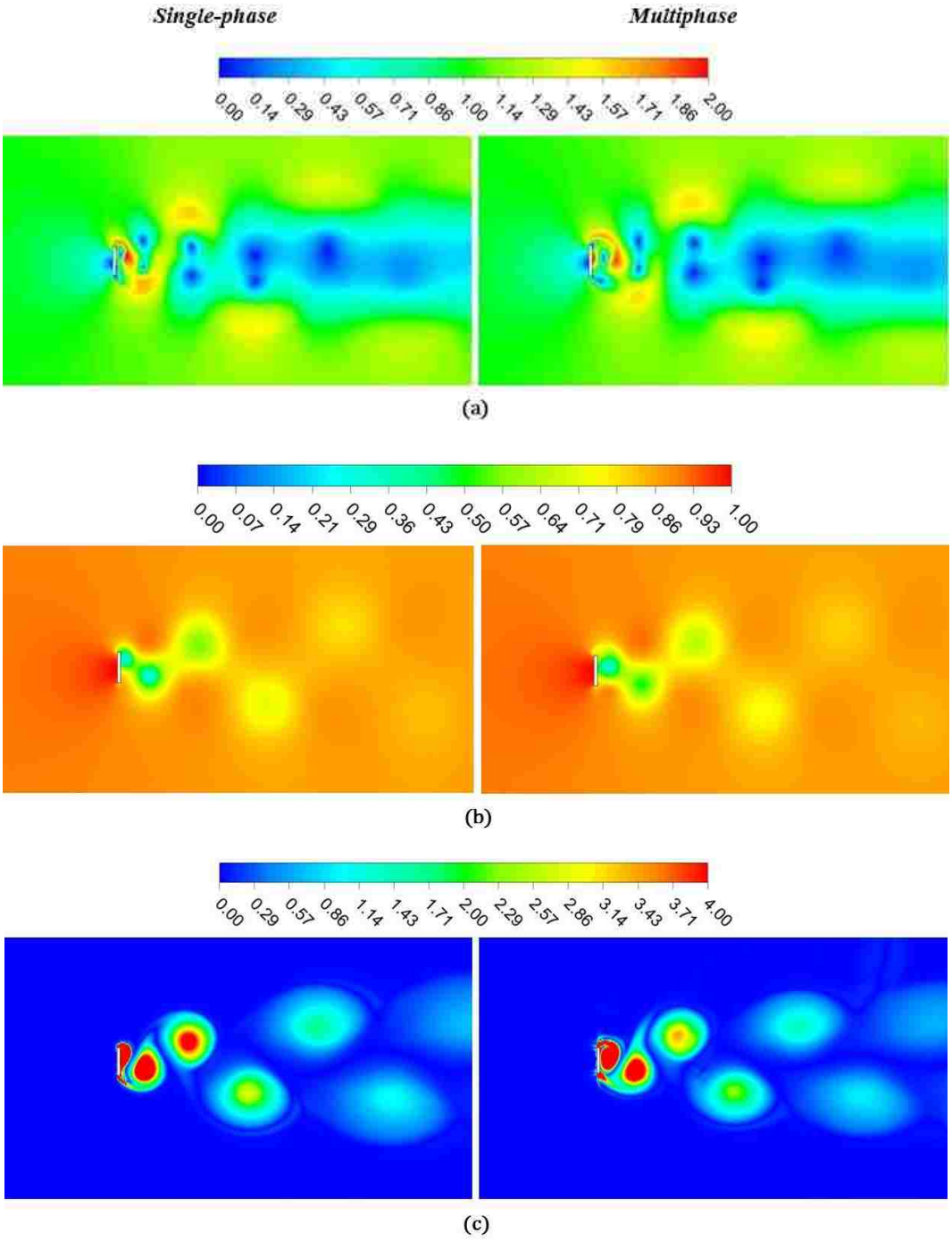

Figure 4. Instantaneous contours of (a) the normalized velocity, (b) the normalized pressure, and (c) the normalized vorticity. Single-phase flow results are depicted in the left column and multiphase results of liquid phase are depicted in the right column.

Figure 5 and Figure 6 depict instantaneous contours of the volume fraction of the gas phase and the concentration of the dissolved oxygen in the liquid phase predicted by the Eulerian multiphase model and the mixture multiphase model, respectively. The flow and the concentration field predicted by the Eulerian model are a more accurate representation as discussed earlier. Figure 5 and Figure 6 show results obtained using the variable bubble size including the breakage and the coalescence. Contours of the volume fraction of the gas phase and the concentration of the dissolved oxygen predicted by these models are very different due to the rise of the gas phase driven by the buoyancy effect. Eulerian method can capture forces of each phase more accurately than the mixture model. The gas phase rises and sticks to the no-slip wall and accumulates over the surface. As a result, the characteristics of the dissolved oxygen in the field predicted by these models are strikingly different. With the rise of the gas phase and its accumulation over the surface, more oxygen dissolves in that region, as shown in Figure 5(b). The influence of the buoyancy effect on the distribution of the gas phase predicted by the mixture model is very slim. Hence the concentration of the dissolved oxygen is nearly symmetric about the centerline, as shown in Figure 6(b).

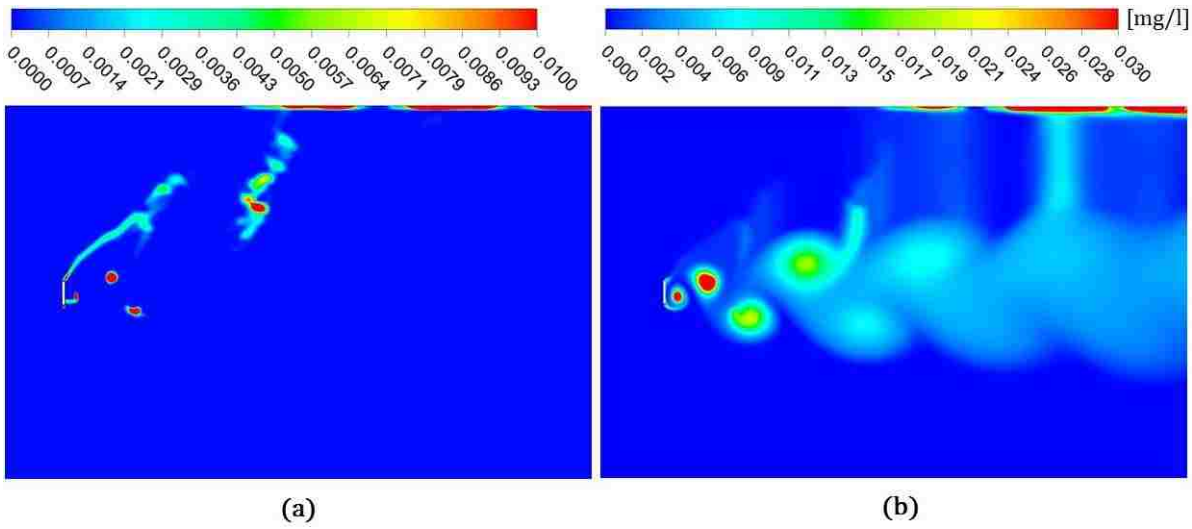

Figure 5. Instantaneous contours of (a) volume fraction of the gas phase and (b) concentration of the dissolved oxygen in the liquid phase predicted by the Eulerian multiphase model in the two-dimensional geometry at $\lambda = 300$.

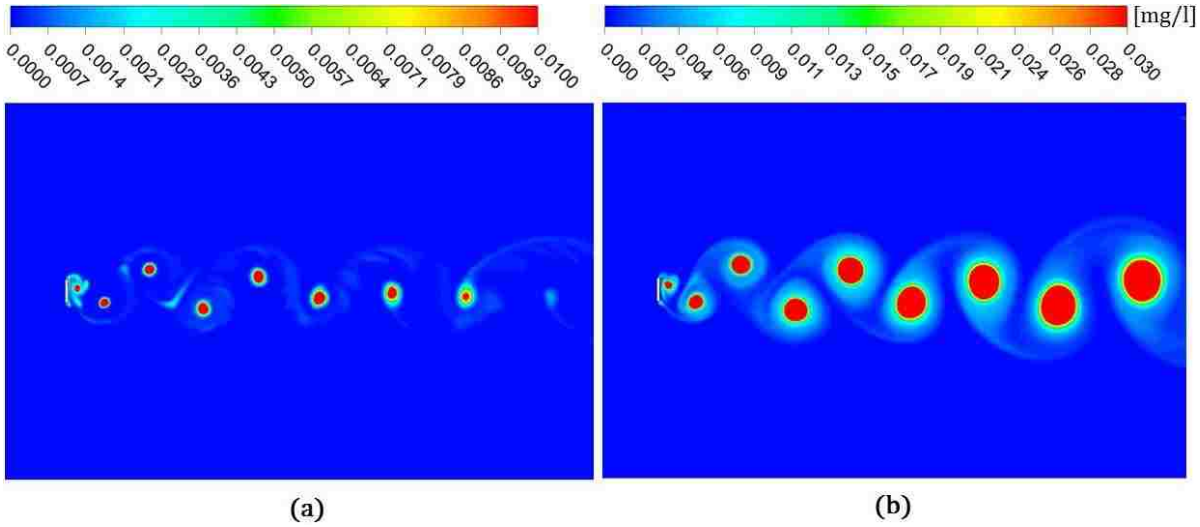

Figure 6. Instantaneous contours of (a) the volume fraction of the gas phase and (b) concentration of the dissolved oxygen in the liquid phase predicted by the mixture multiphase model in the two-dimensional geometry at $\lambda = 222$.

3.2.4 Three-dimensional analyses

LES simulations in three-dimensional geometries are conducted for flows past plates. Multiphase flows past a single finite plate placed normal to the stream-wise

direction and multiple yawed finite plates are simulated. The effect of the aeration on the flow field and the drag coefficient is studied. Multiphase flow results are compared to the single-phase flow results documented in [62].

The mesh study of LES simulations is carried out for the single plate placed in a three-dimensional geometry. Two mesh grids with a number of cells N_1=1.2×10^6 and N_2=2.4×10^6 are used in mesh study. The mesh refinement is mainly applied around the plate. The averaged value of y^+ is reduced from 12.1 to 7.5 from N_1 to N_2. The time-averaged drag coefficient is calculated to be 1.39 and 1.43, respectively for N_1 and N_2. The non-dimensional time step is selected to be 0.004.

The variable bubble size with the breakage and the coalescence and the interfacial drag force are considered for multiphase flows in three-dimensional geometries. The time signature of the drag coefficient predicted by the multiphase flow model is compared to that predicted by the single-phase flow model [62] in Figure 7. The time-averaged drag coefficient is calculated to be 1.43 in the present aeration study for flows past a finite plate, and it is reported to be 1.5 for the single-phase flows [62]. These results show that the aeration can be utilized in river current energy harvesting devices without experiencing significant penalty in power generations. In addition to the nominal value of the drag coefficient, the fluctuations are reduced after the aeration.

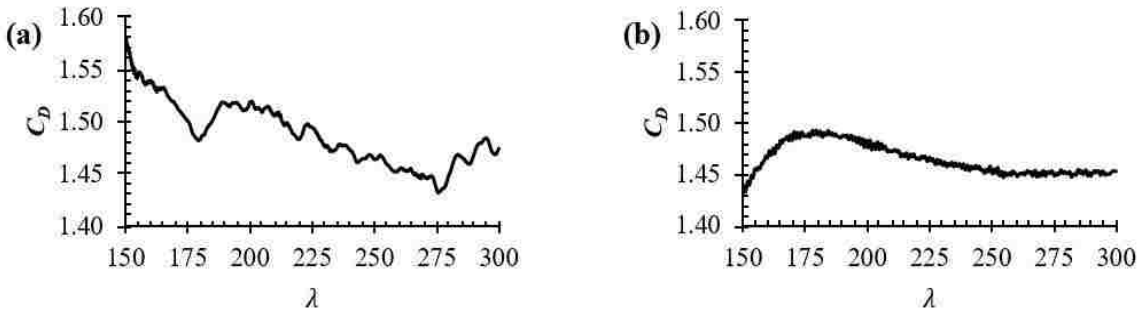

Figure 7. Drag coefficient as a function of non-dimensional time for (a) single-phase flow [62] and (b) multiphase flow with aeration.

Figure 8(a) and Figure 8(b) presents contours of the magnitude of the liquid phase vorticity at $\lambda = 280.5$. Images are acquired at x-y and x-z planes, respectively. Three-dimensional flow fields are influenced strongly by the aeration as compared against single-phase predictions in Ref. [62]. The intensity of vortex shedding is suppressed significantly, as it is shown in the vorticity field. That could have a profound influence on structures since the vibration induced by the vortex shedding would be diminished as air is injected from the plate to aerate the water. Several studies have documented that the injection/suction from the near wake of bluff bodies is able to suppress vortex shedding and delay flow separations [63, 64].

Contours of the dissolved oxygen concentration in the liquid phase are depicted in Figure 8(c) and Figure 8(d). It is observed from Figure 8(a)-(b) and Figure 8(c)-(d) that maximum level of oxygen dissolution is observed in regions where high vorticity magnitude appears. This observation indicates that induced momentum mixing in the wake region plays an important role in the mass transfer from the gas phase to the liquid phase. This study also shows that the aeration in these systems can be enhanced by promoting momentum mixing.

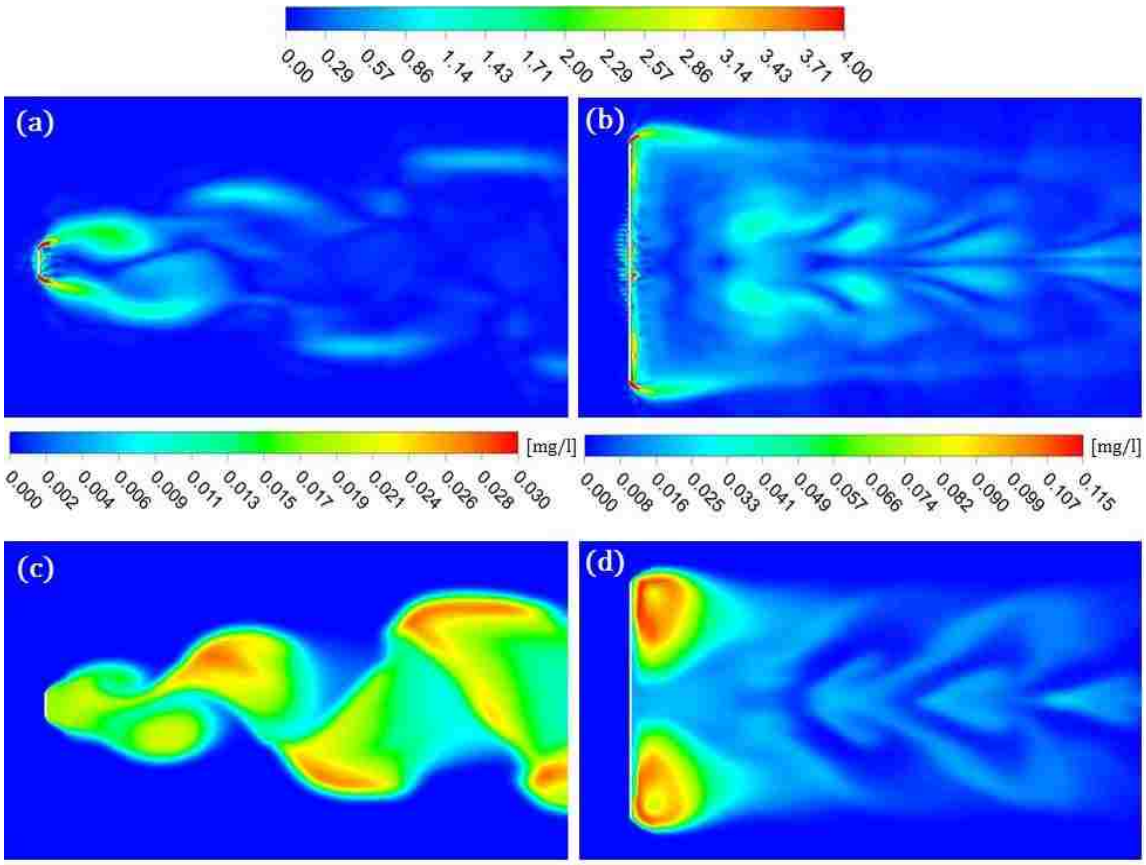

Figure 8. Instantaneous contours of (a, b) the normalized liquid phase vorticity (top row) and (c, d) the dissolved oxygen concentration in the liquid phase (bottom row). Images are acquired at the x-y plane (left column) and the x-z plane (right column) at λ =280.5.

In order to characterize the vortex structures in the flow field, the Q-criterion is applied [65]. Q-criterion is defined as $Q = \frac{1}{2}(\|S\|^2 - \|\Omega\|^2)$, where S is the strain tensor and Ω is the rotation tensor. Figure 9(a) shows the instantaneous iso-surface of Q-criterion at a constant level of Q = 0.003 colored by the normalized vorticity magnitude. Figure 9(b) illustrates the iso-surface of the dissolved oxygen in the liquid phase at a constant value of 0.01 mg/l. Figure 9(c) depicts the iso-surface of the volume fraction of the gas phase at a constant value of 2×10^{-4} at $\lambda = 280.5$. It is clear from Figure 9(a) and 9(b) that patterns

of the dissolved oxygen concentration are very similar to patterns of the vorticity field. The gas phase is moving with the continuous liquid phase, as depicted in Figure 9(c).

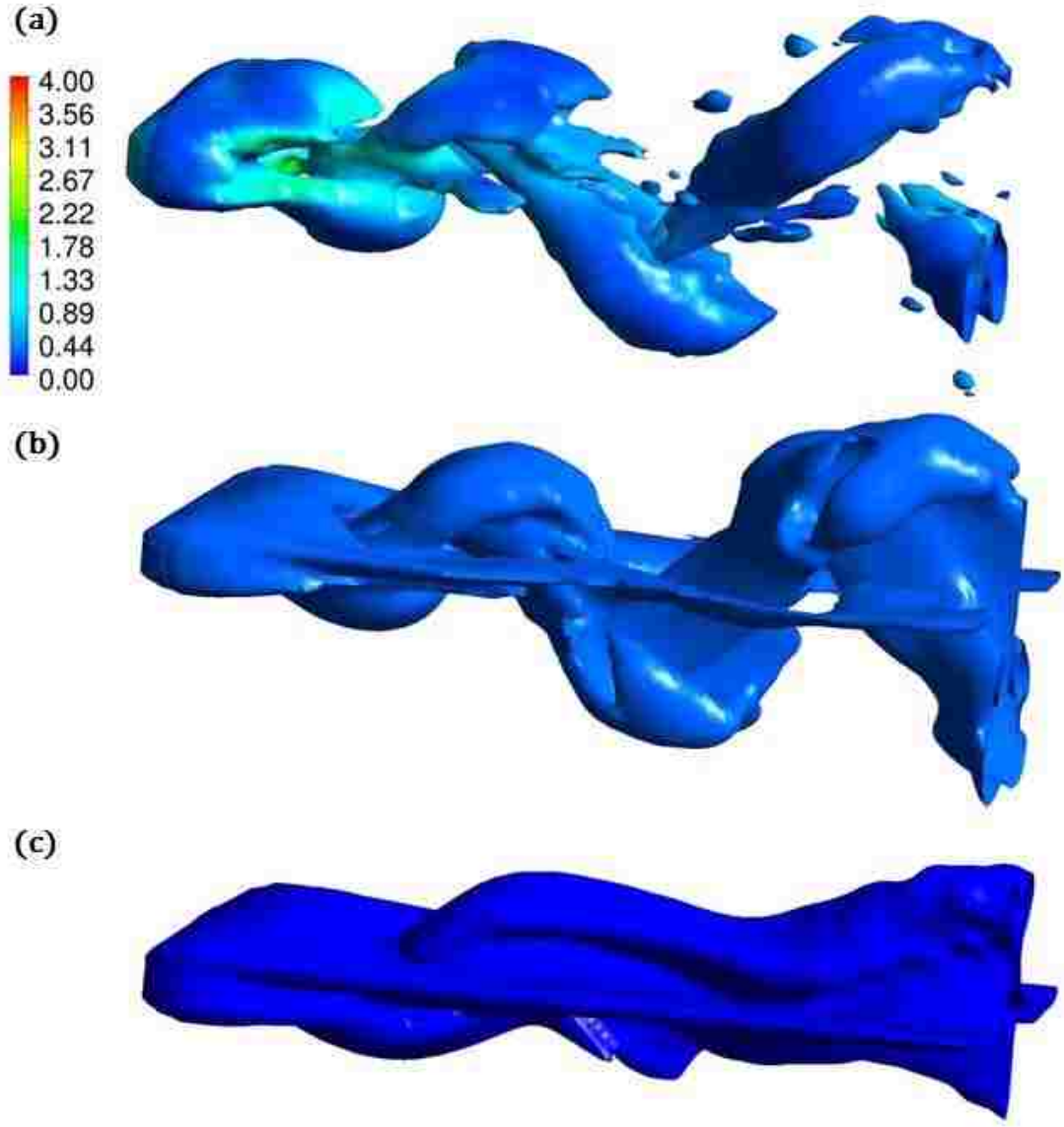

Figure 9. (a) The instantaneous iso-surface of Q = 0.003 colored by the normalized vorticity magnitude, (b) the iso-surface of the dissolved oxygen in the liquid phase at a constant value of 0.01 mg/l and (c) the iso-surface of the volume fraction of the gas phase at a constant value of 2×10^{-4} at $\lambda = 280.5$.

Aeration through four yawed plates is simulated with a longitudinal spacing of 5*H* between the plates in the same row. The number of elements in the discretized, three-dimensional computational domain of multiple yawed plates is 2.6×10^6, and the non-dimensional time step is selected to be 0.004. The time-averaged drag coefficient of each plate predicted by multiphase flow simulation is compared to that reported by the the single-phase flow study of the same configuration in Ref. [62], see Table 2 for comparison. The drag coefficient of downstream plates is lower than that of upstream plates for both single-phase and multiphase flow simulations. The observed reduction in the drag coefficient of downstream plates is due to the wake interaction induced by the upstream plate. The drag coefficient of upstream plates is not influenced by air injection adversely. However, the drag coefficient of downstream plates is reduced by about 67% when the aeration is applied. The interaction between the downstream plate and the air injected from the upstream plate may cause the reduction in the drag coefficient. Air phase profoundly affects the force exerted on the downstream plate. In order to increase the drag coefficient of the downstream plate, an optimization study must be conducted for the longitudinal spacing between plates.

Table 2. Time averaged drag coefficient of upstream and downstream plates in the staggered configuration obtained from prior single-phase flow simulation and present multiphase flow simulation. Plates are labelled as P_1, P_2, P_3 and P_4 as shown in Fig 1.

Plate	**Single-phase**	**Multiphase**
$\overline{C}_{D,P1}$	1.04	1.10
$\overline{C}_{D,P2}$	1.08	1.13
$\overline{C}_{D,P3}$	0.66	0.22
$\overline{C}_{D,P4}$	0.66	0.21

Figure 10(a) illustrates the instantaneous iso-surface of Q-criterion at a constant value of Q = 0.003. Q-criterion is colored by the normalized vorticity magnitude. Figure 10(b) depicts the iso-surfaces of the dissolved oxygen in the liquid phase at a constant value of 0.02 mg/l at $\lambda = 198$. The maximum vorticity level is observed at the leading edge of each plate. Vortices generated from plates migrate toward the center plane, as shown in Figure 10(a). Such behavior is also observed through the iso-surfaces of dissolved oxygen in Figure 10(b). It is also noticed that the high level of turbulence observed in the wake region of the single-phase flow [62] is not seen in the multiphase flow due to the air injection.

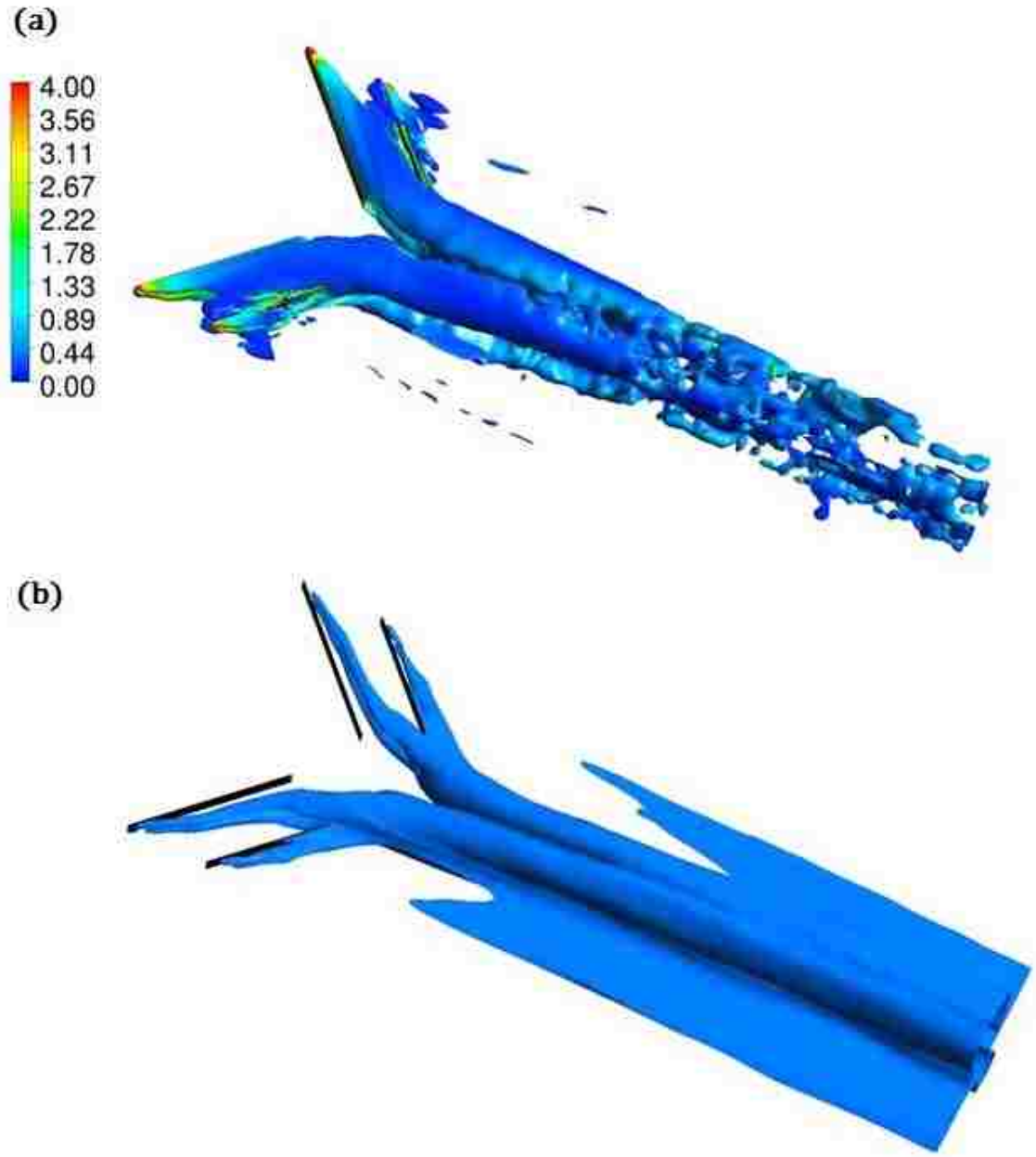

Figure 10. The instantaneous iso-surface of Q = 0.003 colored by the normalized vorticity magnitude and (b) iso-surface of the dissolved oxygen in the liquid phase at a constant value of 0.02 mg/l at $\lambda = 198$.

Conclusion

Computational fluid dynamics simulations are conducted to examine transient flows past plates in two- and three-dimensional geometries. The effect of aeration on flow structures and hydrodynamic forces acting on structures are investigated. Aeration is achieved by injecting air at the top and the bottom surfaces of plates. The oxygen dissolution model is validated by comparing predicted dissolved oxygen level in a bubble column to prior experimental findings. Predicted results agree reasonably well with measured results.

The parametric study is carried out to study the influence of various phenomena on the drag coefficient of the plate and the aeration characteristics. The dissolved oxygen concentration is hardly influenced by interfacial forces such as the lift force, the wall-lubrication force, and the turbulent dispersion force. The drag force has been taken into consideration as an interfacial force between the gas and liquid phase. The oxygen dissolution is influenced by the combined effects of the flow field and the mass transfer. The effect of the breakage and the coalescence on the oxygen dissolution is not strong.

Transient LES simulations in three-dimensional geometries of a single plate and multiple yawed finite plates have been carried out. The mixture multiphase model along with interfacial drag force and sink and source terms in IAC transport equation are employed. It is noted that the dissolved oxygen level is higher in regions with intense vortical activities. This observation suggests that momentum mixing enhances the aeration in these systems.

The time-averaged drag coefficient of plates predicted here by the multiphase flow model is compared to that of single-phase flow simulations reported in Ref. [62]. For a single plate, the difference in the drag coefficient between single-phase and multiphase flow simulations is less than 5%. For multiple plates, the drag coefficient of the upstream plate is not influenced by the air injection. However, the drag coefficient of downstream plates is reduced significantly when plates are tightly spaced as aeration is introduced. Careful optimization study for the longitudinal distance between the plates is essential in the design of energy harvesting systems consisting of translating blades. This study demonstrates that river current energy harvesting devices can be utilized for aeration to improve water quality for better aquatic life.

CHAPTER 4 LARGE EDDY SIMULATIONS OF VENTILATED HYDROKINETIC TURBINE AT DESIGN AND OFF-DESIGN OPERATING CONDITIONS

Large eddy simulations of pre-designed and optimized ventilated micro-hydrokinetic turbine are conducted at the design and off-design operational conditions. The simulations are performed for the pre-designed micro hydrokinetic turbine with and without aeration at off-design tip-speed ratios of 1.2 and 2.7 and at the design tip-speed ratio of 1.86. Air is introduced to the turbine downstream from the turbine hub. The multiphase simulations are performed using mixture multiphase model and LES turbulence model. The spatial and temporal characteristics of oxygen dissolution into the water are examined. Moreover, the influence of aeration on turbine performance and turbine vibration is also revealed. To the best knowledge of the author, computational study of aeration has not been considered for hydrokinetic turbines previously.

Numerical Method and Computational Domain

The pressure based segregated algorithm, Semi-Implicit Method for Pressure-Linked Equations (SIMPLE), was used to solve continuity and momentum equations. The Pressure Staggering Option (PRESTO) scheme was used in the pressure interpolation. The equation of volume fraction was discretized using first-order upwind scheme to prevent the divergence that observed in Quadratic Upstream Interpolation for Convective Kinematics (QUICK) scheme. Second order upwind discretization scheme was used for the interfacial area concentration and the mass transport equations.

The design and optimization of the turbine used in this study were completed by Schleicher et al. [66, 67]. The turbine geometry has two blades with the wrap angle of 142.9° and the tip diameter of 0.5334 m. As shown in Figure 11, the turbine geometry used in this study lacks the tower and nacelle. The effect of both tower and nacelle on both near and far turbine wake dynamics were studied by several researchers. Kang et al. [68] conducted simulations with and without the presence of the tower and nacelle. Results indicate that including the tower and the nacelle will result in wake meandering and the vortices created from both of them interact with the turbine tip vortices. Recently, Santoni et al. [69] conducted LES simulation of flow past a wind turbine to highlight the influence of both tower and nacelle on the turbine wake region. They observed that turbulent eddies induced by the tower interact with the vortex rope generated from the turbine blades and promotes the breakage of the blade tip vortices. They also documented that, although including the tower and nacelle has an influence in the near wake dynamics of the turbine, its presence does not have a strong influence on the power generation. Here, the tower and the nacelle are not included due to the complexity of generating body-fitted grids for the computational domain. The schematics of the turbine design are shown in Figure 11, and the geometric design parameters are tabulated in Table 3.

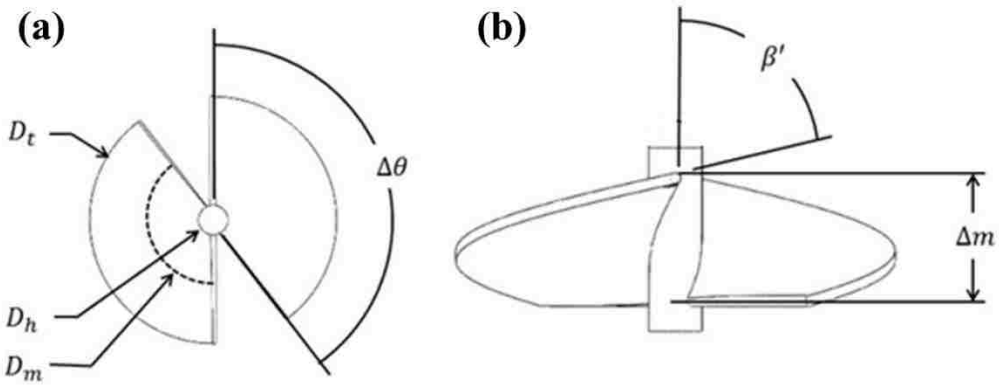

Figure 11. Turbine geometry, (a) front and (b) side view [70].

Table 3. Turbine design variables.

Variable	Value	Variable	Value
D_t (tip diameter)	0.5334 m	β (relative flow angle)	52.58°
D_h (hub diameter)	0.0635 m	β' (blade angle)	72.26°
D_m (mean diameter)	0.3745 m	Δm (meridional length)	0.1488 m
$\Delta\theta$ (wrap angle)	142.29°	σ (solidity)	0.83

The computational domain, boundary conditions, and geometric details are shown in Figure 12. The air is injected from the turbine hub to the downstream in the axial water flow direction. The computational domain contains two subdomains; stationary and rotatory, which are then connected to each other through the meshing interface. The turbine rotation is performed within the cylindrical, rotational subdomain which has a diameter of $2D_t$ and extending $2.9D_t$ upstream and $6D_t$ downstream of the blade leading edge. In order to transfer all flow variables between these domains; the non-conformal mesh interfaces technique is implemented. The distance from the water inlet to the turbine is $5.72D_t$ and the distance from the turbine to the outlet of the flow domain is $8.86D_t$.

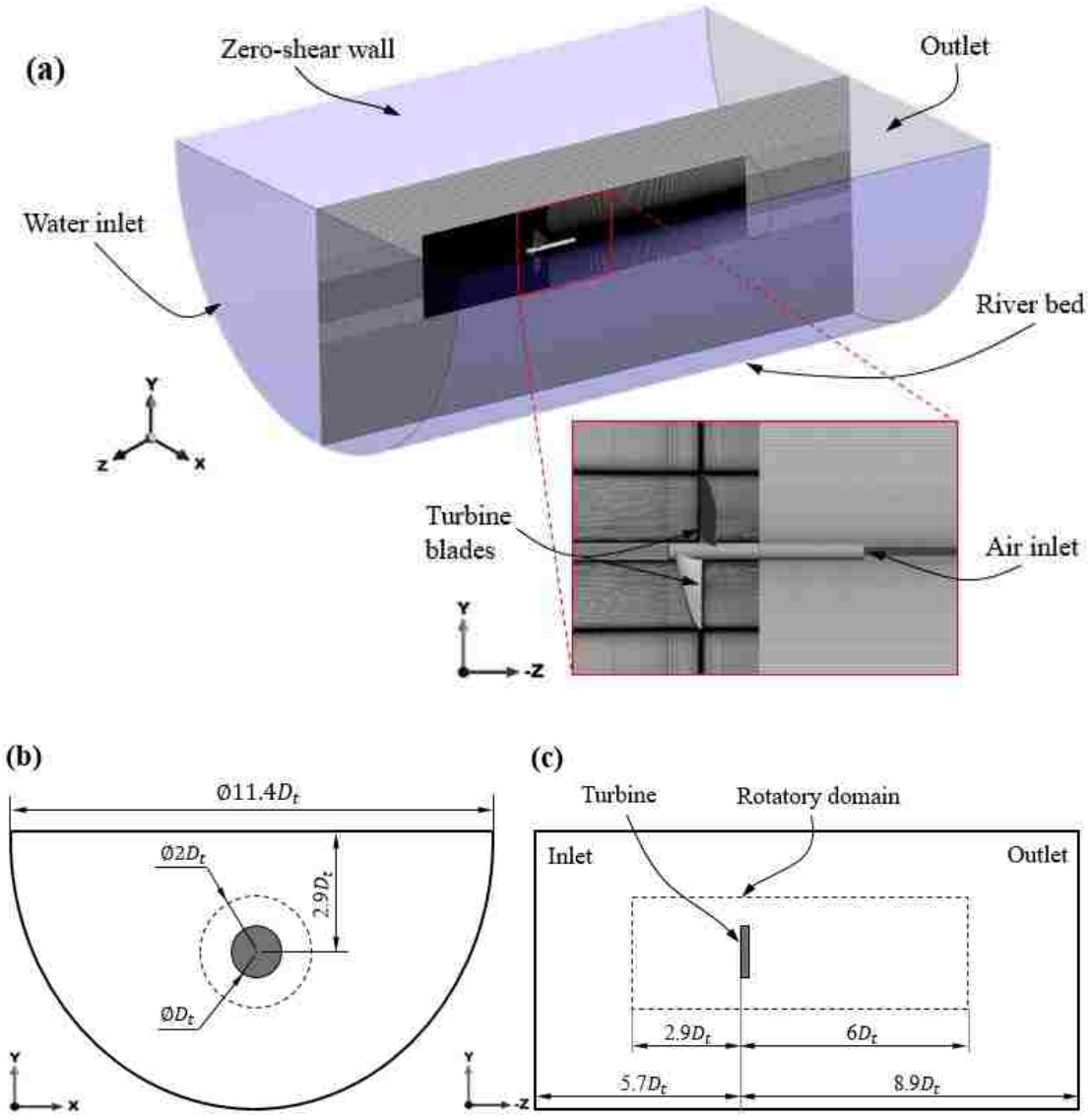

Figure 12. Computational domain with boundary conditions and geometric details: (a) Three-dimensional view of the computational domain and the mesh along the central, vertical plane across the domain, (b) front view of the domain, and (c) side view of the domain.

Schleicher et al. [67] characterized the current turbine performance by conducting steady-state single-phase simulations. At turbine's best efficiency point, they reported free-stream velocity of 2.25 m/s and turbine rotational velocity of 15.708 rad/s which result in the tip-speed ratio of 1.86. In this study, transient single-phase and multiphase simulations

are conducted at three different tip-speed ratios: λ = 1.2, λ = 1.86 and λ = 2.7. The tip-speed ratio is adjusted using a uniform free-stream velocity of U_∞ =2.25 m/s and varied turbine rotation speed. The turbine rotation speeds at each operating point are tabulated in Table 1. The air injection velocity from the turbine hub surface is assumed to be U_g =0.316 m/s that provides air flow rate as 0.2% of water flow rate at turbine swept area. The oxygen mass fraction in the water, $x_{O_2,l}$, is assumed to be zero at water inlet and the oxygen mass fraction in the gas phase, $x_{O_2,g}$ is set to a value of 0.233 at the air inlet. The injected air bubble size is assumed to be 0.1 mm at the air inlet, the bubble size varies inside the flow domain within the range of 0.02 mm to 0.5 mm as a direct result of the changes in the flow field variables, the mass transfer, the breakage and the coalescence effects. Initially, the computational domain is filled with water with zero dissolved oxygen content. For the outlet boundary of the flow domain, the outflow boundary condition is used. This type of boundary condition imposes zero gradient normal to the boundary face for all flow variables except for pressure. The no-slip wall boundary condition is applied for the turbine surface and the top surface of the computational domain is set to be zero-shear wall to resemble the free surface. The river bed boundary is treated as no-slip smooth wall, hence, the effects of natural river bed topography on the flow is not considered in this study. Natural waterways such as rivers often have complex bed topography with sequences of riffle and pool, sediment bar, and deep scour patterns. These geometrical irregularities can induce strong secondary flows that can influence the turbine performance and the structural integrity of turbine unit [71]. Several researchers investigated the interactions between the secondary flows induced by complex river bed topology and the hydrokinetic turbine.

Chamorro et al. [72] reported that the turbine performance is influenced by the approaching turbulent eddies inside the flow. In addition to the influence on the power output, Chamorro et al. [73] also showed that the turbine wake stability and velocity field recovery depend on the turbulent eddies generated by the upstream objects. However, to simplify the numerical approach; simulations in the present study are conducted for a straight uniform channel without geometric irregularities and by implementing a uniform inflow velocity profile at the water inlet with U_∞=2.25 m/s. Table 4 provides the values and units of the parameters used in the present study. ω represents the angular speed of the turbine at distinct tip-speed ratios, U_∞ is the free-stream water velocity and U_g is the air velocity.

Table 4. Parameters used in the current study.

Parameter	Value	Unit	Parameter	Value	Unit
$\omega_{\lambda=1.2}$	10.124	[rad/s]	U_∞	2.25	[m/s]
$\omega_{\lambda=1.86}$	15.708	[rad/s]	U_g	0.316	[m/s]
$\omega_{\lambda=2.7}$	22.778	[rad/s]			

Figure 12(a) illustrates the mesh along the y-z plane in addition to the computational domain and the boundary conditions. Figure 13 provides additional details about the mesh along (a) the blade surface, (b) the blade trailing edge and (c) the blade root. As shown in the figures, particularly the cell size which is normal to the surface of the turbine blade is refined to capture small eddies that are expected to be generated near the blade surface. Moreover, a finer mesh is also crucial to capture the wake dynamic behind the turbine. This statement was clear from the results obtained by Kang et al. [68]. They conducted LES simulations to investigate the three-dimensional wake dynamics behind the axial hydrokinetic turbine. It was clear that using coarser mesh caused underestimations of

both the intensity and extent of the wake structures compared to the results from a finer mesh. However, in the current study, the mesh refinement is not applied for each desired region inside the computational domain due to the restriction that comes with the aforementioned Milelli condition [59]. We employed LES approach with mixture multiphase model. The mesh is coarsened downstream the turbine where bubbly flow presents in order to control the stability and to prevent the divergence in numerical solution due to the aforementioned restriction, see Figure 12. To avert the above restriction; the minimum cell size used in the mesh study for each of the three meshes including N_1=12×10^6 cells, N_2=20×10^6 cells and N_3=34×10^6 cells is: 2 mm, 1.1 mm and 0.88 mm, respectively. This way the minimum cell size, 0.88, is more than 1.5 times higher than the maximum limiting bubble diameter inside the flow domain, which is 0.5 mm. Thus, the stability and accuracy of the numerical results can be maintained.

Simulations are conducted using high-performance computers, named Bridges, at the Pittsburgh Supercomputing Center. Two parallel nodes are used, each including 28 cores and 128 GB RAM. The computing time of one turbine revolution is roughly three days and 3 hours for multiphase simulation including 34 million cells and two days and 6 hours for multiphase simulation including 20 million cells. Results are presented for five-turbine revolutions except for the mesh study.

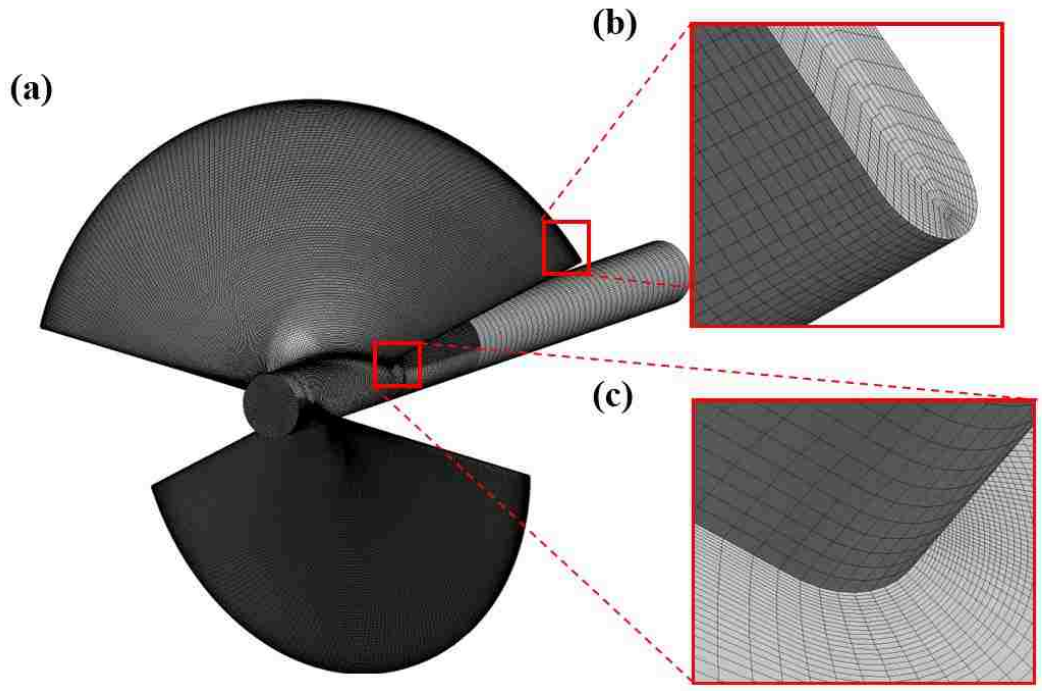

Figure 13. The mesh along (a) the blade surface, (b) the blade trailing edge and (c) the blade root.

Results and Discussion

4.2.1 Spatial and Temporal Convergence Study

The mesh study is conducted for multiphase simulations with mixture multiphase model and LES turbulence model. The mesh study is performed for the tip-speed ratio of 1.2. The mesh density of N_1, N_2 and N_3 are used to calculate the power and the thrust coefficient. The mesh resolution used in the wake region inside the rotating domain is: 164, 164 and 230 for N_1; 175, 175 and 226 for N_2; and 210, 210, and 274 for N_3 in the x, y and z direction, respectively. Milelli condition limits further refinement of the mesh in this region. The time signature of the power and thrust coefficient is depicted in Figure 14. The relative differences between N_1 and N_2 for power and thrust coefficients are 5.0% and

0.8%, respectively. The relative differences reduced to around 2.6% and 0.1% between the meshes N_2 and N_3. The mean y^+ value along the blade surface is predicted to be 7.7, 5.5 and 3.9 for the cases including 12×10^6, 20×10^6 and 34×10^6 cells, respectively. In order to minimize the computational cost; the numerical predictions obtained by the medium mesh N_2 will be presented in this study for both single-phase and multiphase simulations. However, for the critical tip-speed ratio of 1.2 associated with flow separation, the multiphase results will be presented using the finer mesh, N_3. This is because the finer mesh is required to resolve the flow field near the blades and in the wake region at this operating condition. The mean y^+ value for N_2 mesh along the blade surface is predicted to be roughly 6.5 and 7.7 at the tip-speed ratio of 1.86 and 2.7, respectively.

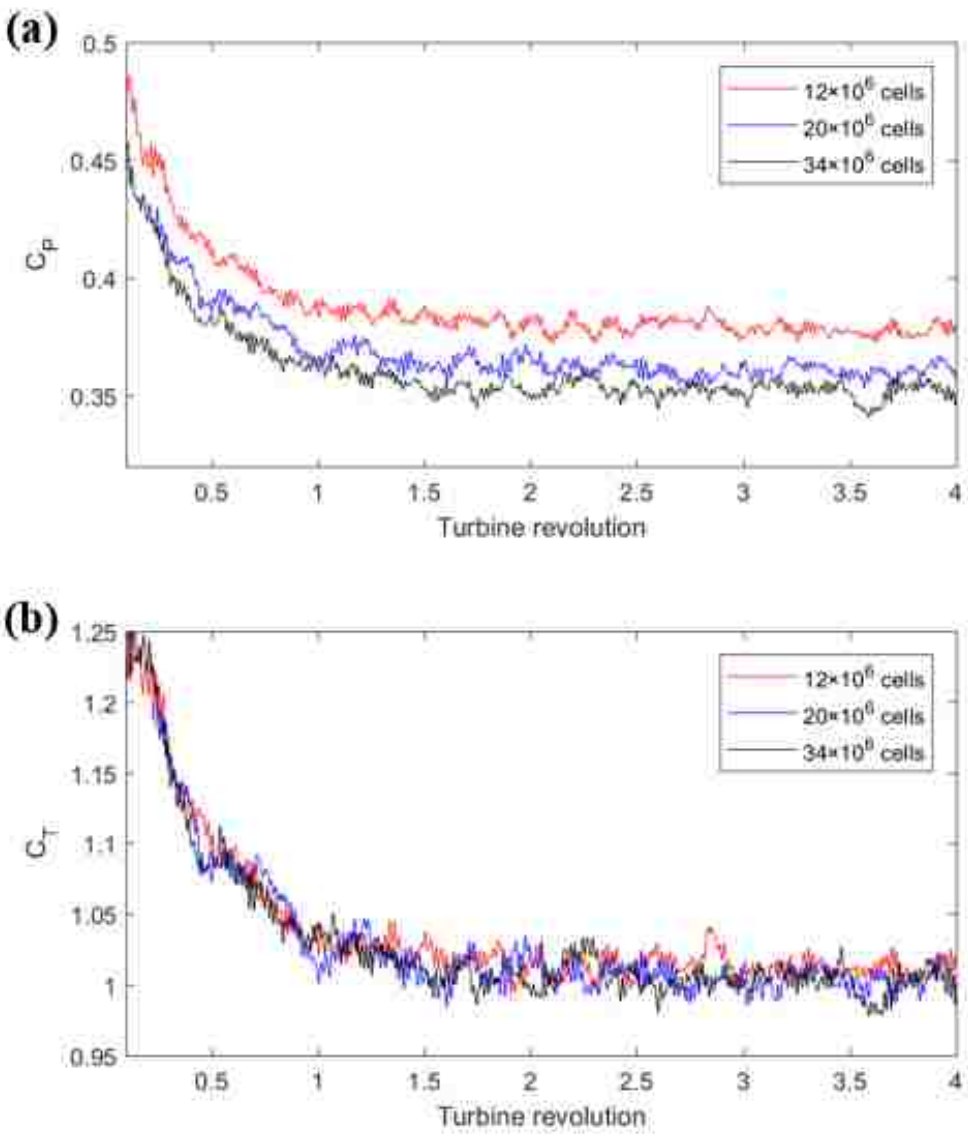

Figure 14. Turbine performance parameters obtained by various mesh densities: (a) power coefficient as a function of turbine revolution, (b) thrust coefficient as a function of turbine revolution.

Figure 15 depicts profiles of the stream wise component of normalized velocity at three locations for meshes N_1, N_2 and N_3. The time-averaged velocity profiles are acquired at various distances from the blade leading edge: $1D_t$, $2D_t$ and $3D_t$ (see Figure 15(a)). The line at $1D_t$ passes through the turbine hub and this causes discontinuity in the velocity

profiles, see Figure 15(b). The time averaging started after the 2nd revolution and continued until the end of 4th revolution. The results show a reasonable agreement in the stream wise velocity component even with the time averaging of two revolutions. The profiles reveal relatively higher fluctuation near the central, hub region of the turbine, this indicates the highly turbulent region in the flow domain. The time averaging should be conducted using longer flow time, however, due to limited computational resources we use only two turbine revolutions for time averaging. Span-wise and cross flow component of the velocity are not presented for comparison since they require time averaging at much longer flow time. Moreover, due to the Milelli condition as mentioned earlier, the mesh in this region could not be refined further. Even if the accuracy of the flow field is suffered from the limited resolution in the wake region, the wake flow structure is presented to explain the dissolution characteristic of the system.

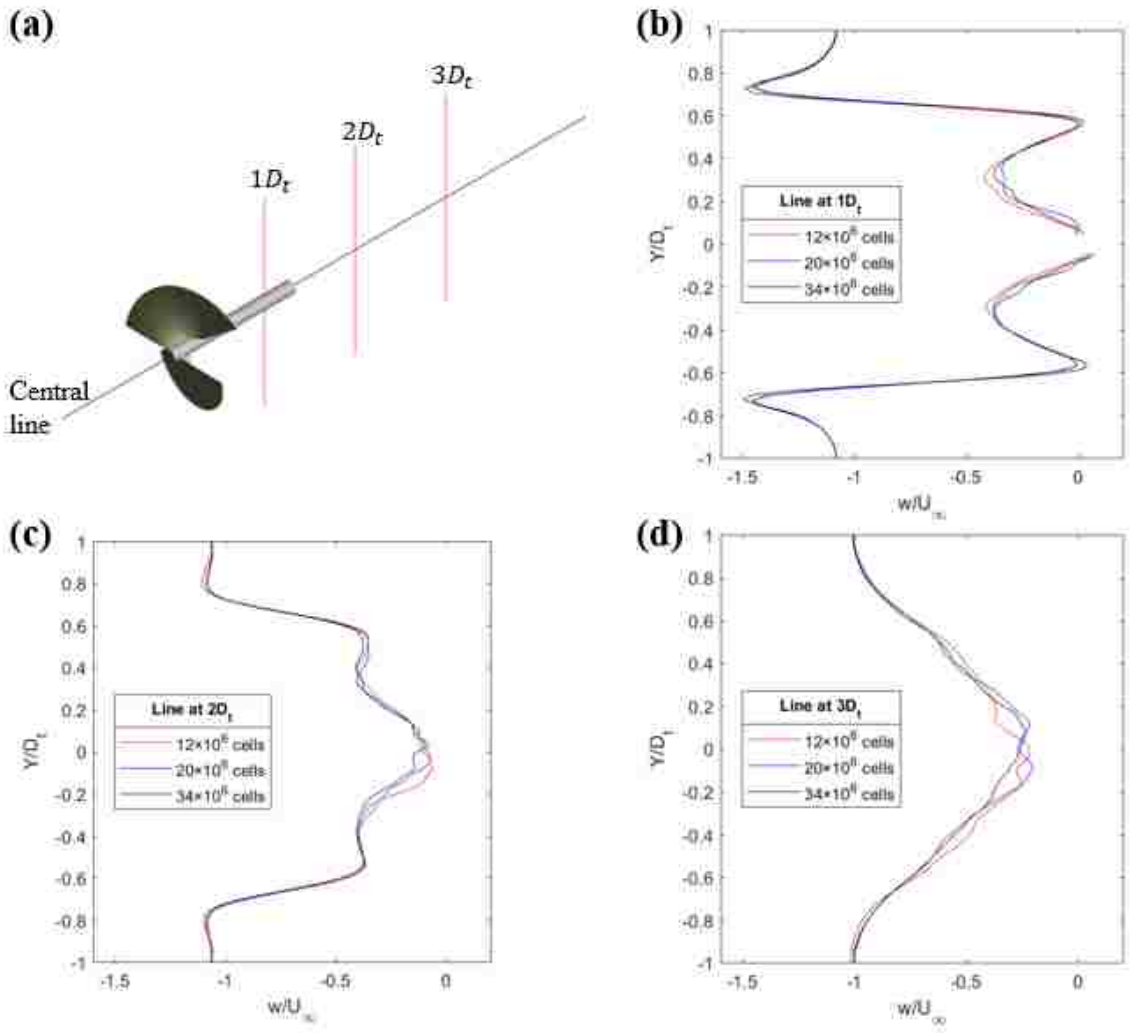

Figure 15. The profiles of stream wise component of normalized velocity obtained by various mesh densities: (a) the positions of the probe lines and the profiles of streamwise component of the normalized velocity at (b) $1D_t$, (c) $2D_t$ and (d) $3D_t$.

The determination of time step size is another important step in transient numerical simulations. Present researchers conducted the temporal convergence study of present turbine previously at its design point using sequentially decreasing time step values of 0.005 s, 0.0025 s and 0.001 s with single-phase RANS simulations [72]. They compared the power coefficient predicted by each time step and concluded that the relative difference between the results is less than 1%. In their study, the smallest time step size of 0.001s

yields 0.9° turbine rotation for each time step. In the present study, the time step size of each case (λ = 1.2, λ = 1.86 and λ = 2.7) are adjusted based on the turbine rotation rate and yields 0.9° angular motion within each time step. The time step sizes are determined to be 1.55×10^{-3} s, 1.0×10^{-3} s and 6.89×10^{-4} s for λ = 1.2, λ = 1.86 and λ = 2.7, respectively.

4.2.2 Turbine Performance

The turbine operating conditions are characterized based on the tip-speed ratio that is defined as the ratio between the tangential velocity of the blade tip and the free-stream water velocity, see Eq. (32). Turbine performance parameters, the power coefficient and the thrust coefficient, are normalized in Eqs. (33)-(34) as follows:

$$\lambda = \frac{\omega D_t}{2U_\infty} \tag{32}$$

$$C_P = \frac{P}{\frac{\pi}{8}\rho D_t^2 U_\infty^3} \tag{33}$$

$$C_T = \frac{T}{\frac{\pi}{8}\rho D_t^2 U_\infty^2} \tag{34}$$

Here, λ represents the tip-speed ratio, ω is the turbine rotation rate, U_∞ is the free-stream water velocity, C_P is the power coefficient, P is the power, C_T is the thrust coefficient, T is the thrust force and D_t is the turbine tip diameter. The signature of power and thrust coefficient are illustrated in Figure 16 and Figure 17 for λ = 1.2, λ = 1.86 and 2.7. The time averaging of power and thrust coefficient are done between the turbine revolutions of 2.0 - 5.0 and tabulated in Table 5 with corresponding standard deviation. In the lower tip-speed ratio case at λ = 1.2, aeration lowered the nominal value of power coefficient by only 1.9%.

However, it highly influenced the standard deviation of power coefficient by increasing it 56%. However, at turbine's design point, $\lambda = 1.86$, air introduction provides a slight improvement in the power generation by 1.6% and roughly 9% reduction in the deviation of this power output. March [14] also reported a slight efficiency increase for the centrally aerated turbine at Norris Dam. At $\lambda = 2.7$, the power generation increases slightly by 3.1% with air injection and the standard deviation of power coefficient is reduced approximately 19%. Due to the reduced deviation in power output, the turbine will experience valuable improvement in stability. It must be noted here that even the standard deviation at lower tip-speed ratio operation increases significantly after the aeration, it yields standard deviation lower than that observed at $\lambda = 1.86$ and $\lambda = 2.7$, see Table 5. There is also a minor influence of air injection on the nominal values of thrust coefficient at all three tip-speed ratios. Similar trend is also observed for the standard deviation of the thrust coefficient. At lower tip-speed ratio, the thrust coefficient standard deviation is increased 47%. In contrast, it decreased roughly 18% at tip-speed ratio of 1.86 and 2.7. Our results clearly demonstrate that the influence of aeration on the turbine performance is strongly dependent on the turbine operating conditions.

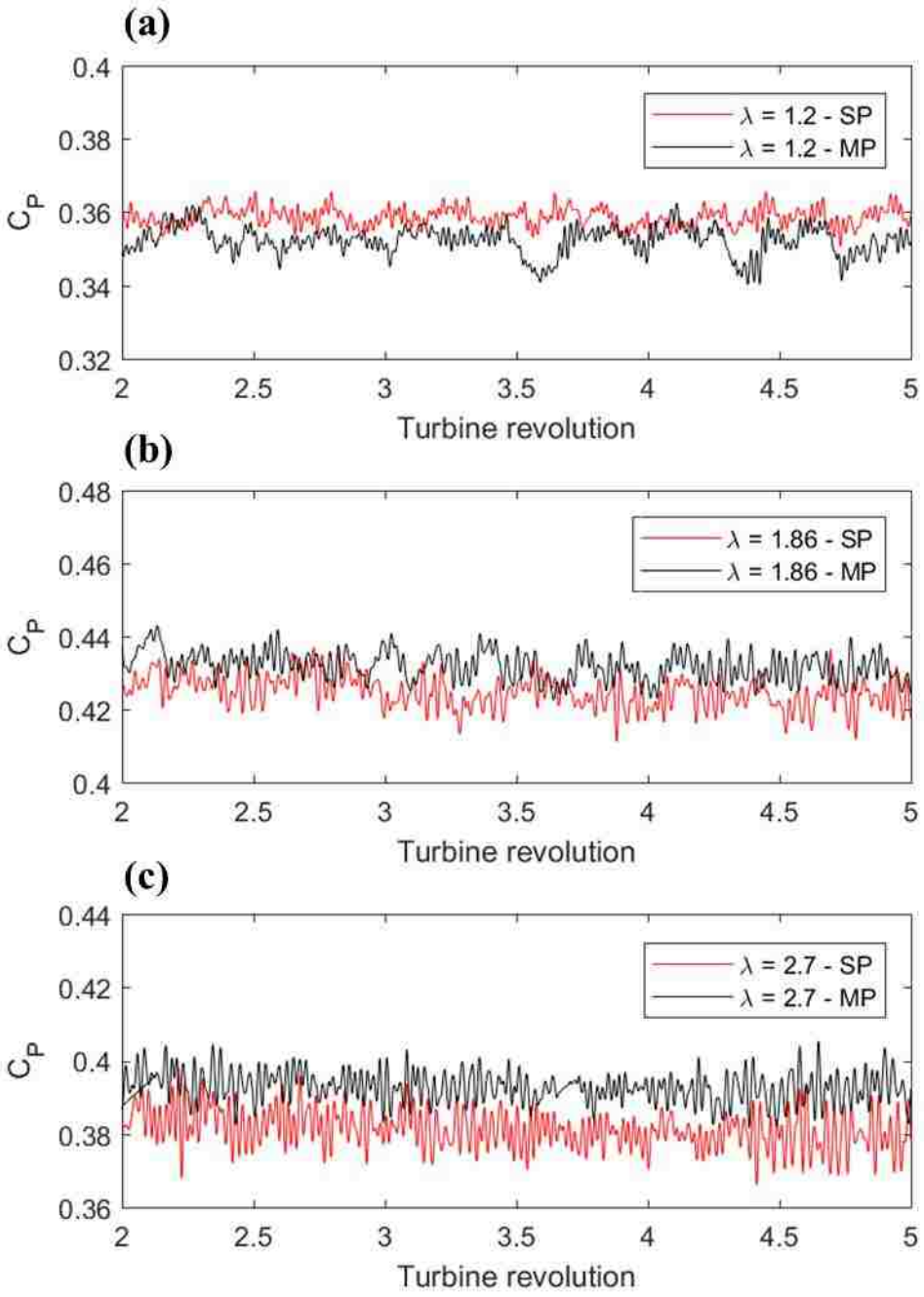

Figure 16. Power coefficient as a function of turbine revolution for the single-phase (SP) and the multiphase (MP) simulations at (a) λ = 1.2, (b) λ = 1.86 and (c) λ = 2.7.

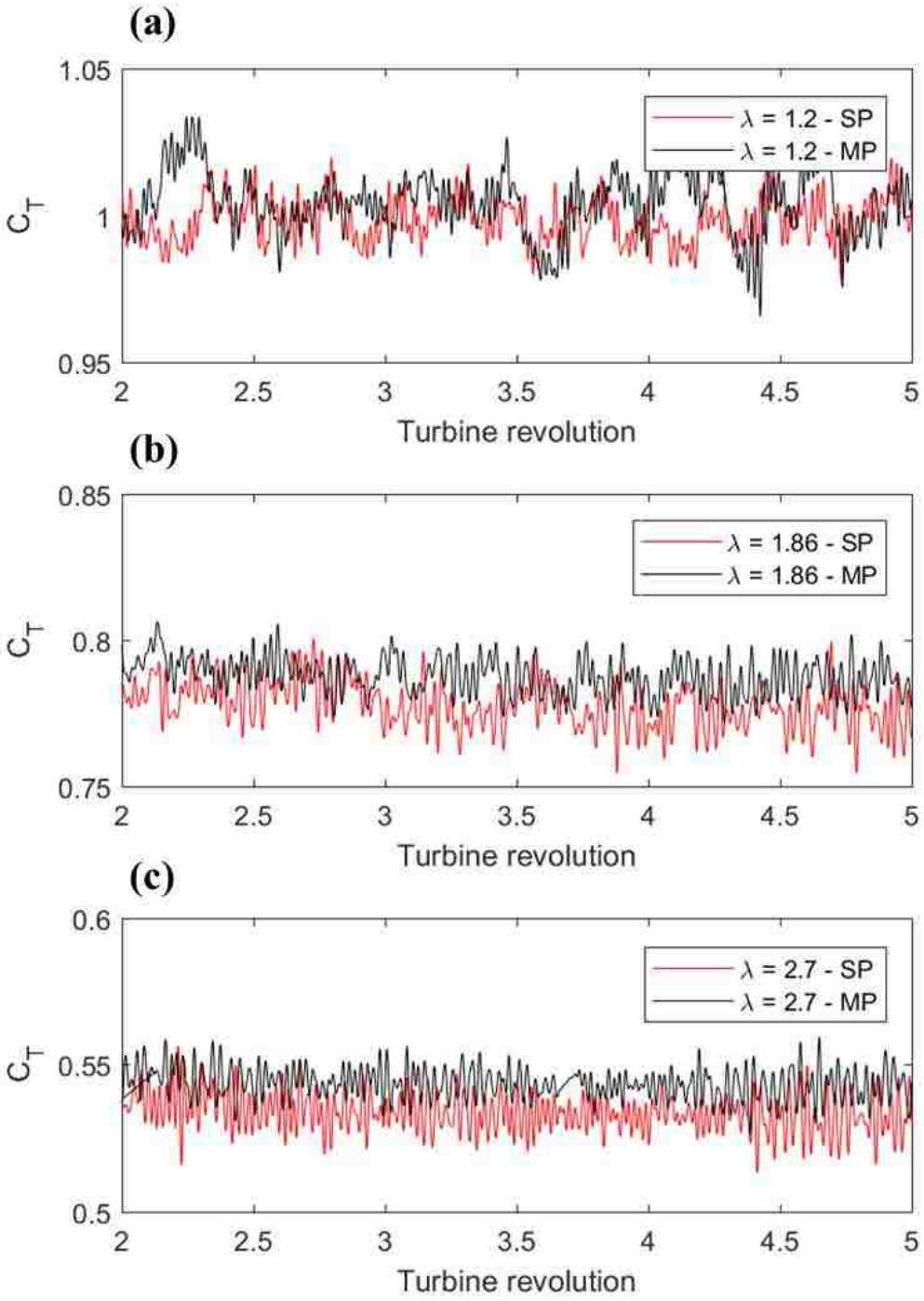

Figure 17. Thrust coefficient as a function of turbine revolution for the single-phase (SP) and the multiphase (MP) simulations at (a) λ = 1.2, (b) λ = 1.86 and (c) λ = 2.7.

Table 5. Predicted power and thrust coefficient with standard deviation.

Tip-speed ratio	Phase	Power coeff. ($C_P \pm \sigma$)	Thrust coeff. ($C_T \pm \sigma$)
λ=1.2	Single-phase	0.359±0.0025	0.998±0.0074
	Multiphase	0.352±0.0039	1.004±0.0109
λ=1.86	Single-phase	0.425±0.0043	0.778±0.0078
	Multiphase	0.432±0.0039	0.788±0.0064
λ=2.7	Single-phase	0.381±0.0052	0.534±0.0065
	Multiphase	0.393±0.0042	0.544±0.0053

4.2.3 Flow Field Structures – Aeration

Daskiran et al. [74] documented the occurrence of flow separation when the tip-speed ratio is lower than the design tip-speed ratio using RANS approach. Similar behavior was observed for both single-phase and multiphase simulations carried out at λ = 1.2 in the present study employing LES approach. Figure 18 depicts the streamlines along the cylindrical surface at a diameter of $0.66D_t$ for single-phase simulations at (a) λ = 1.2, (b) λ = 1.86 and (c) λ = 2.7. The cylindrical surface is colored by normalized static pressure. The normalization of the pressure is presented in Eq. (35), where $\tilde{p}$ represents normalized pressure, p_{min} and p_{max} are the minimum and maximum pressure in each flow field, respectively. The higher and the lower pressure was observed on the pressure and suction side of the blade, respectively for all three cases. The flow separation occurred from the blade leading edge for the lower tip-speed ratio, as shown in Figure 18(a). The pressure is the lowest in the center region of vortices generated from the blade leading edge.

$$\tilde{p} = \frac{p - p_{min}}{p_{max} - p_{min}} \tag{35}$$

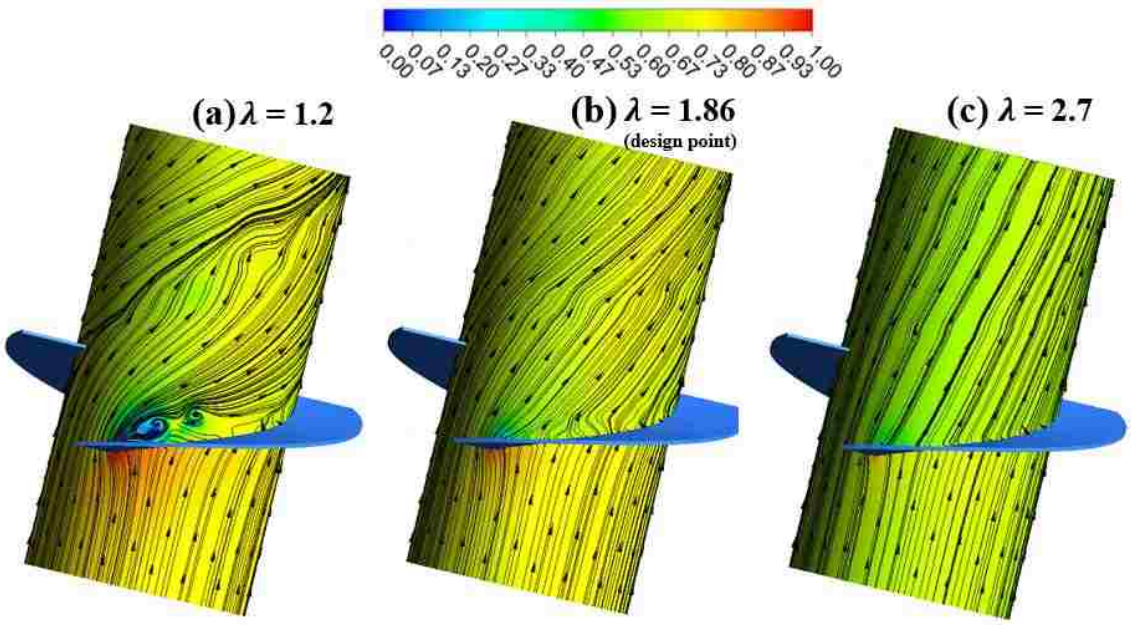

Figure 18. Instantaneous streamlines after 5 revolutions on a circular surface at a diameter of $0.66D_t$ for the single-phase simulations conducted at (a) λ = 1.2, (b) λ = 1.86 and (b) λ = 2.7. The cylindrical surfaces are colored by normalized pressure.

Flow field variables, velocity and vorticity magnitude, are normalized based on free-stream water velocity and turbine rotation rate. Normalization of velocity and vorticity are shown in (29) and (36), respectively.

$$\tilde{\omega} = \frac{\left|\varepsilon_{ijk}\frac{\partial U_k}{\partial \times_j}\right|}{\omega} \tag{36}$$

Here, $\tilde{\omega}$ is normalized vorticity and $\left|\varepsilon_{ijk}\frac{\partial U_k}{\partial \times_j}\right|$ is the magnitude of local vorticity. The free-stream velocity are considered to be constant as 2.25 m/s for the three tip-speed ratios. The turbine rotation rate, ω, is adjusted based on the tip-speed ratio. Reynolds number is defined based on turbine tip diameter as follows:

$$Re = \frac{\rho_l U_\infty D_t}{\mu_l} \tag{37}$$

where ρ_l is the density of the liquid phase and μ_l is the dynamic viscosity of the liquid phase. Reynolds number is calculated to be 1.2×10^6 and is kept constant for simulations at each tip-speed ratio.

Instantaneous contours of normalized velocity and vorticity are illustrated in Figure 19 and Figure 20, respectively with and without aeration. The highest velocity and vorticity magnitude are observed at the center region of vortex ropes that are created from each blade tip. The vortex ropes are tightly spaced at λ = 2.7 due to higher turbine rotation speed. The strength of the vorticity ropes and the intensity of smaller flow structures are greater at λ = 1.2 with and without air injection. Intermidate behaviour is observed at the design point tip-speed ratio at λ = 1.86. Figure 21 depicts the iso-surfaces of vorticity for the three cases with and without air introduction. The air phase slightly suppressed the smaller flow structures at turbine downstream for both λ = 1.86 and λ = 2.7, reduced the strength of the vortex ropes, and caused faster dissipation of vortex ropes for both tip-speed ratio. This might be the cause for the slight deviation reduction in power generation, as shown inTable 5. However, for the lower tip-speed ratio, λ = 1.2, the vortices in the central region expanded in the radial direction and more smaller structures are observed in this region after aeration. This behaviour result in the significant increase in the deviation of power generation which is not desirable. As observed in Figure 21(b), the interaction between the main tip vortices and the vortices at the central region causes distortion on the main tip vortex ropes and disorder the regular helix-shaped pattern of these ropes. The influence of the flow separation on the wake flow structures is obvious in Figure 19 through Figure 21

with and without aeration. The separation leads to more chaotic or less coherent flow structures in the wake of the turbine, indicating improved mixing in the near wake region.

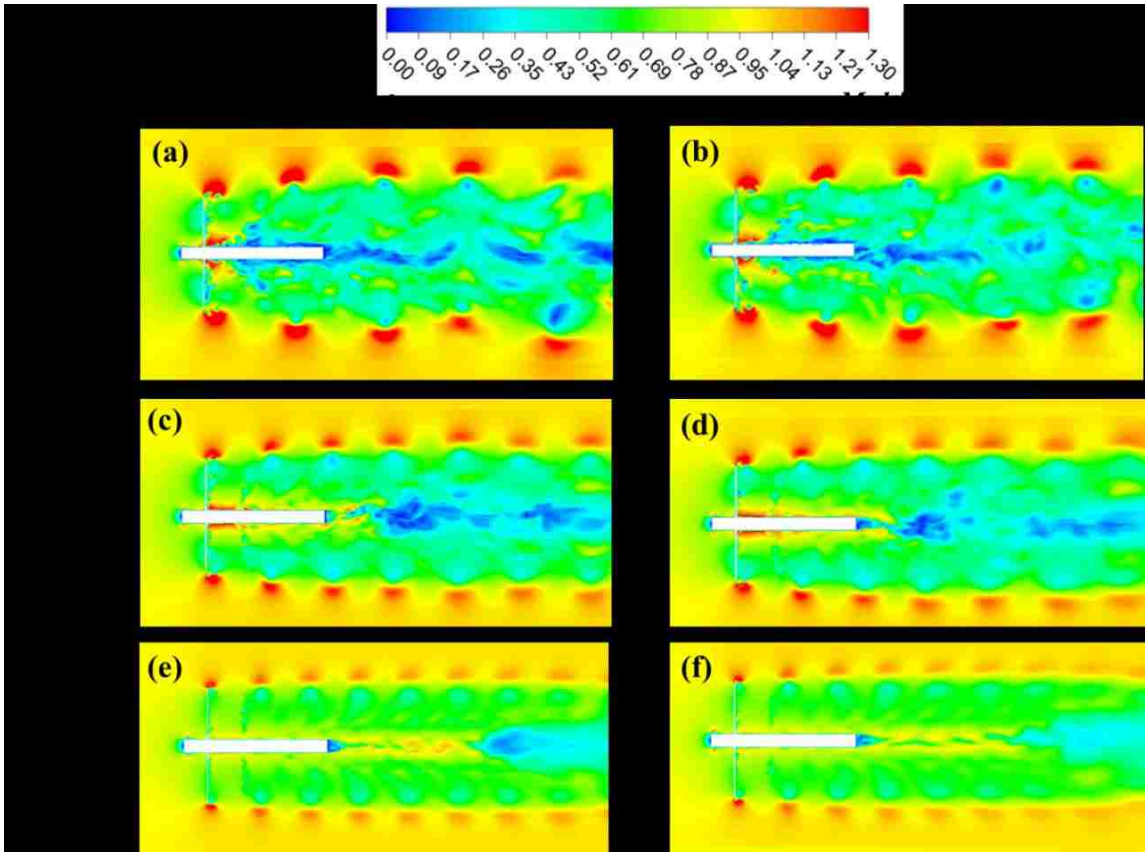

Figure 19. Instantaneous normalized velocity contours after 5 revolutions for the single-phase (SP) and the multiphase (MP) simulations at distinct tip-speed ratios: (a) SP – λ = 1.2, (b) MP – λ = 1.2, (c) SP – λ = 1.86 , (d) MP – λ = 1.86, (e) SP – λ = 2.7 and (f) MP – λ = 2.7.

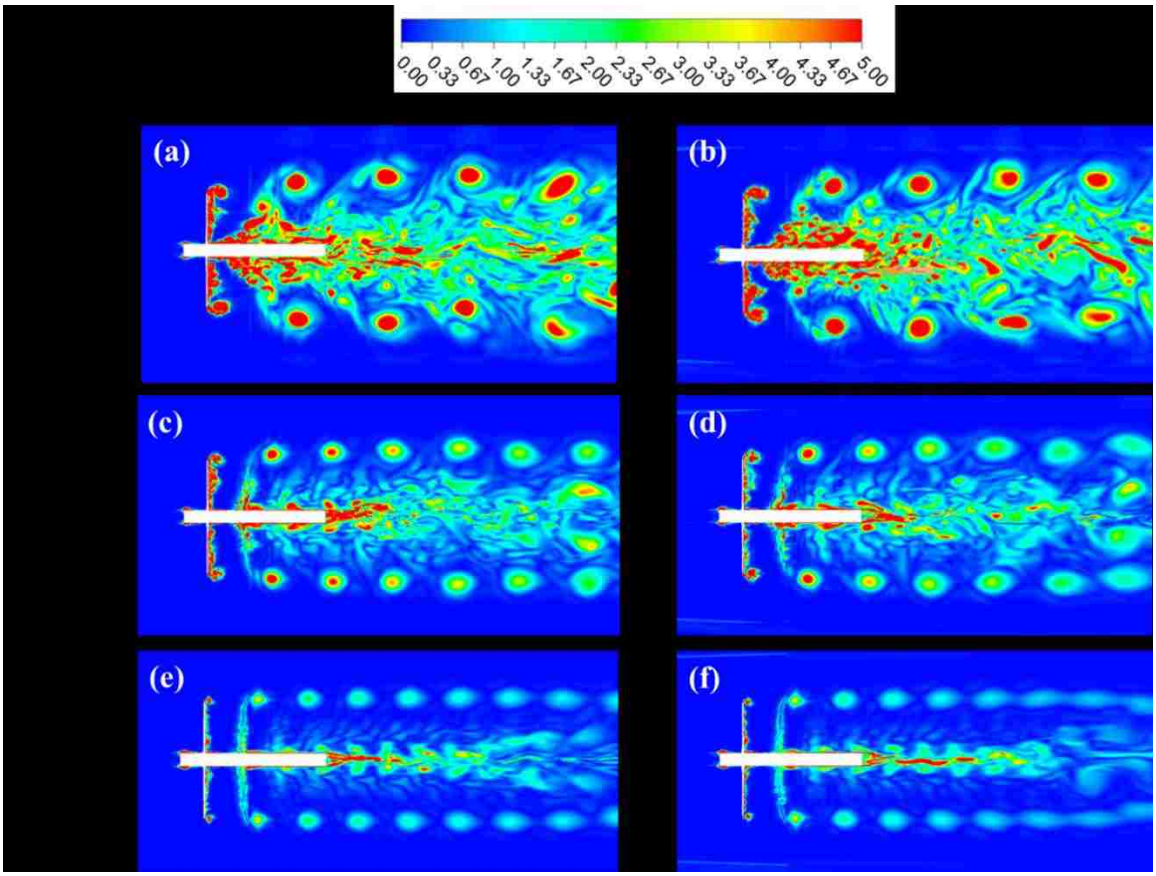

Figure 20. Instantaneous normalized vorticity contours after 5 revolutions for the single-phase (SP) and the multiphase (MP) simulations at distinct tip-speed ratios: (a) SP – λ = 1.2, (b) MP – λ = 1.2, (c) SP – λ = 1.86 , (d) MP – λ = 1.86, (e) SP – λ = 2.7 and (f) MP – λ = 2.7.

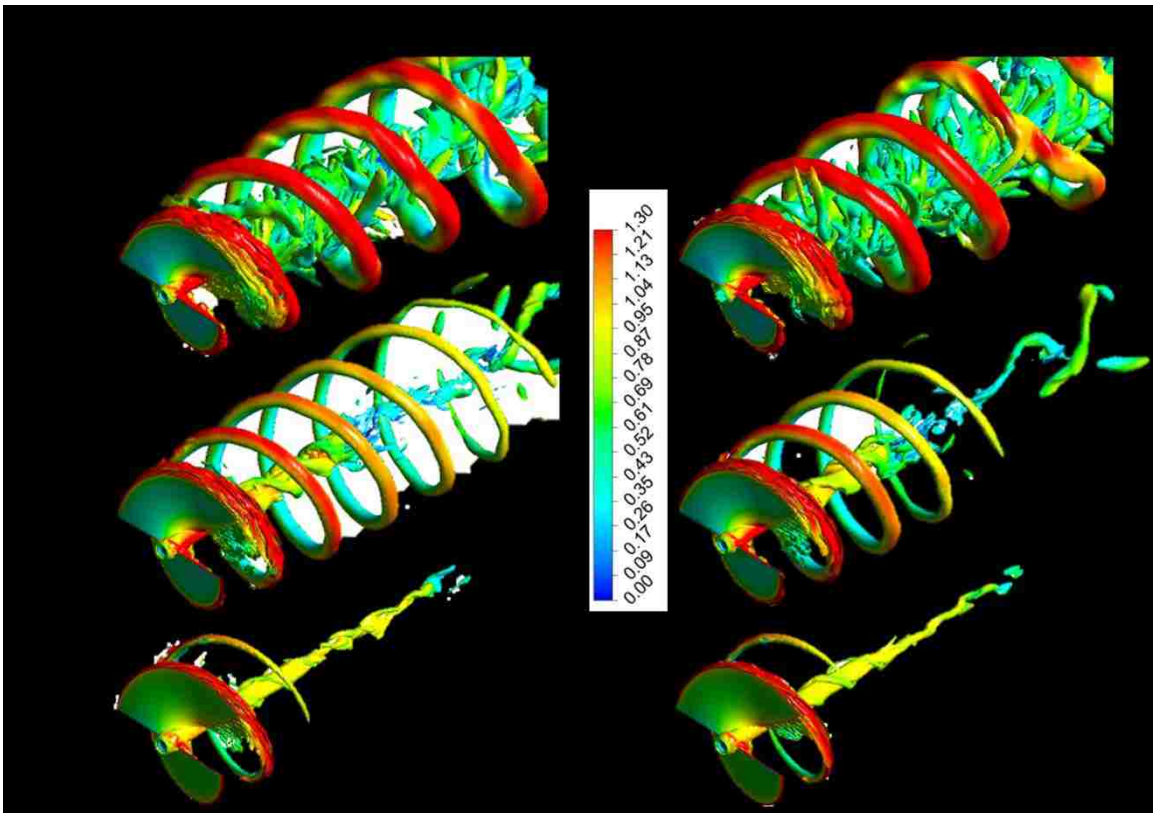

Figure 21. Instantaneous iso-surfaces of normalized vorticity at $\widetilde{\omega}$=2.0 after 5 revolutions for the single-phase (SP) and the multiphase (MP) simulations at distinct tip-speed ratios: (a) SP – λ = 1.2, (b) MP – λ = 1.2, (c) SP – λ = 1.86 , (d) MP – λ = 1.86, (e) SP – λ = 2.7 and (f) MP – λ = 2.7.

Figure 22 illustrates the time-averaged contours of air volume fraction at λ = 1.2, λ = 1.86 and λ = 2.7, respectively. Images are rendered on a vertical plane along the centerline. Because of the vortices created from the hub and enhanced mixing induced by the flow separation at λ = 1.2, the air injected from hub surface is transported both axially and radially. In the case of the design point at λ = 1.86, although the flow separation is not observed clearly, the hub vortices in the central region transported the injected air in both radial and axial directions, see Figure 21(d) and Figure 22(b). For λ = 2.7, the air is mainly transported in the axial direction along the centerline with a minimal dissipation in the radial direction. The air volume fraction is unity at air inlet due to the boundary condition

applied, and it dilutes in the turbine downstream while it is diffusing in radial and axial directions. Due to the lower density of air, it is expected to move upward, however, the introduced air moves centrally at each case. This observation indicates that the swirling effects dominate the buoyancy effects.

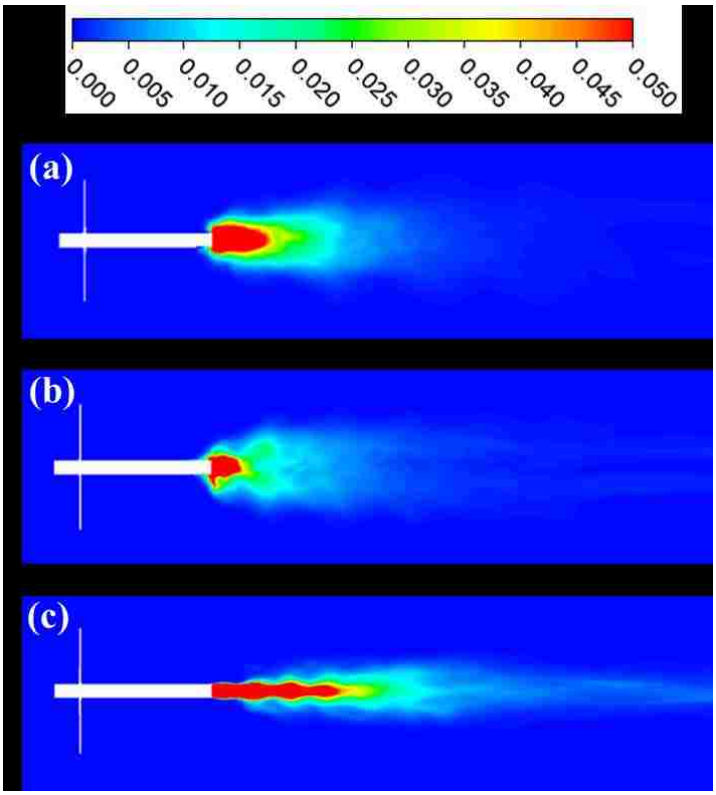

Figure 22. Time-averaged contours of air volume fraction at (a) λ = 1.2, λ = 1.86 and (c) λ = 2.7 after 5 revolutions.

The contours of dissolved oxygen concentration are depicted in Figure 23 for the three values of tip-speed ratio. Three-dimensional view of dissolved oxygen level is illustrated with the iso-surfaces of DO at a constant value of 0.5 mg/l in Figure 24. As the vorticity iso-surface in Figure 21 is compared against the iso-surface of DO concentration in Figure 24, one might obtain that higher dissolution occurs in regions having higher vortical activities. Through the intensive, central hub vortices observed at λ = 1.2 and λ =

1.86 and the flow separation at λ = 1.2, oxygen dissolution occurs in a wider flow field locally and provides better mixing of the dissolved oxygen into the stream near wake region, see Figure 23. Dissolved oxygen levels of approximately 3.5 mg/l and 2.5 mg/l are observed within the near wake for tip-speed ratio of 1.2 and 1.86, respectively. For λ = 2.7, nearly saturated and highly concentrated DO throughout the near wake within the central portion of the wake is observed. Contours of oxygen mass fraction in air are also illustrated in Figure 25. Similar to the contours of DO concentration in Figure 23, the oxygen in air is observed in a wider radial space at λ = 1.2 and λ = 1.86. It must be also noted that the mass fraction of oxygen that is 0.233 at the air inlet reduces as air moves downstream due to the oxygen transfer occurred from air to water.

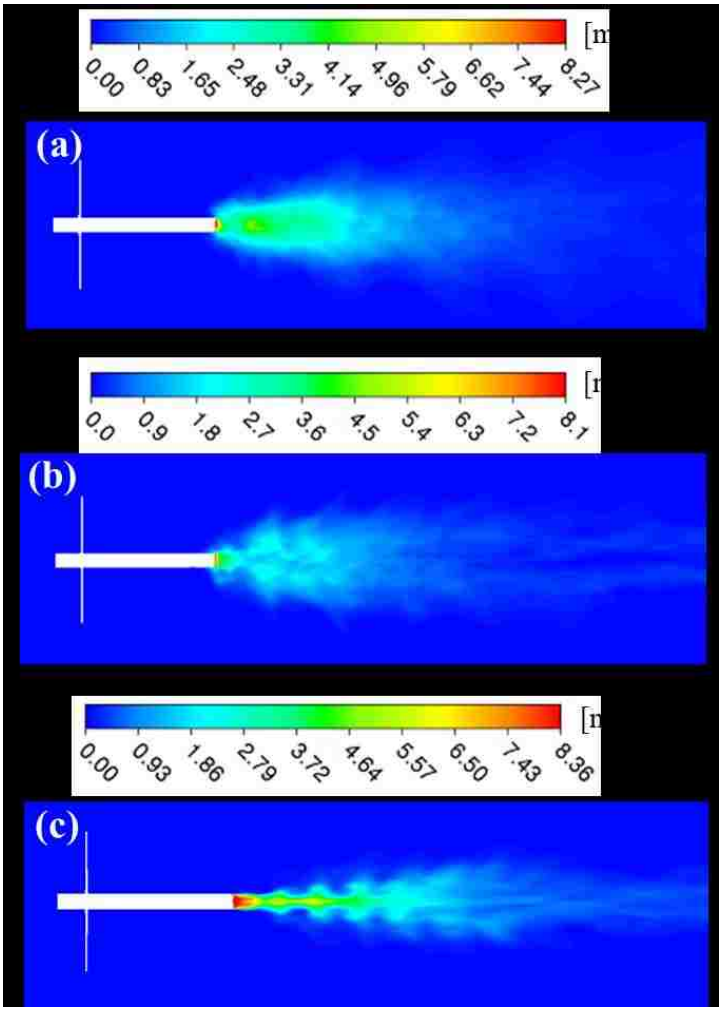

Figure 23. Time-averaged contours of dissolved oxygen concentration at (a) $\lambda = 1.2$, $\lambda = 1.86$ and (c) $\lambda = 2.7$ after 5 revolutions.

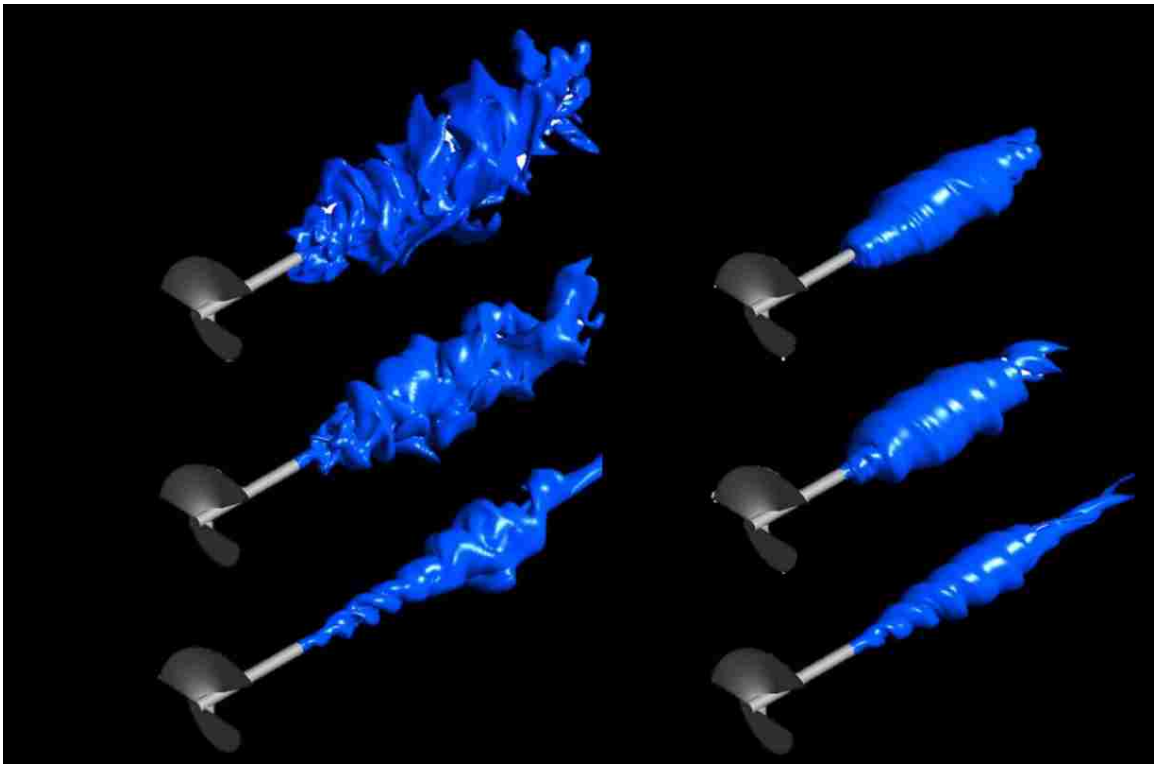

Figure 24. Instantaneous and time-averaged iso-surfaces of dissolved oxygen concentration at 0.5 mg/l at (a)-(b) λ = 1.2, (c)-(d) λ = 1.86 and (e)-(f) at λ = 2.7 after 5 revolutions.

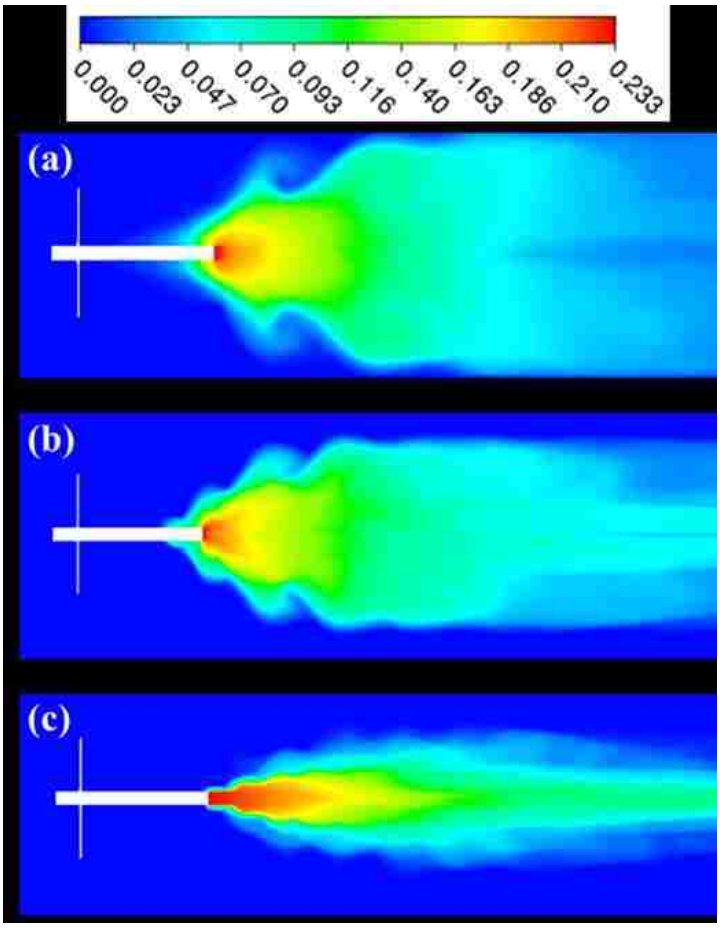

Figure 25. Time-averaged contours of oxygen mass fraction in air (undissolved oxygen) at (a) $\lambda = 1.2$, $\lambda = 1.86$ and (c) $\lambda = 2.7$ after 5 revolutions.

The amount of dissolved and undissolved oxygen inside the flow domain is calculated to determine the oxygen dissolution efficiency for each tip-speed ratio. Dissolution efficiency is defined as the ratio of the amount of dissolved oxygen to the amount of total oxygen. Figure 26 illustrates the dissolution efficiency as a function of (a) turbine revolution and (b) flow time for all three tip-speed ratios. As aforementioned, the tip-speed ratio is adjusted by varying the turbine rotation speed. Therefore, the turbine operating at $\lambda = 2.7$ rotates faster and completes five revolutions in a shorter time as observed in Figure 26(b).

The dissolution efficiency begins leveling off asymptotically within 5 turbine revolutions for the lower tip-speed ratio at λ = 1.2. It must also be noted that the reason of sudden leveling off in λ = 1.2 case is related to having the highest flow time after 5 revolutions in this case. Due to higher flow time, the injected air and the water including dissolved oxygen start to leave from the outlet. The simulations must be conducted further to allow both air phase and dissolved oxygen fields to settle. In case of the design tip-speed ratio, λ = 1.86 and higher tip-speed ratio, λ = 2.7, the dissolution efficiency just starts leveling and needs additional turbine revolutions to determine the exact values of dissolution efficiency. Unfortunately, due to the limited computational resources available and the high cost of such simulation, the simulations are not performed further revolutions. However, it is clear that the asymptotic value of dissolution efficiency at tip-speed ratio of 1.2 and 1.86 is expected to be higher than that at λ = 2.7. As mentioned earlier, the higher vortical activities and the dispersion of air in the radial direction due to the vortices created from the hub and the blade root at tip-speed ratio of 1.2 and 1.86, and the flow separation that observed at λ = 1.2 improved the mixing and the dissolution.

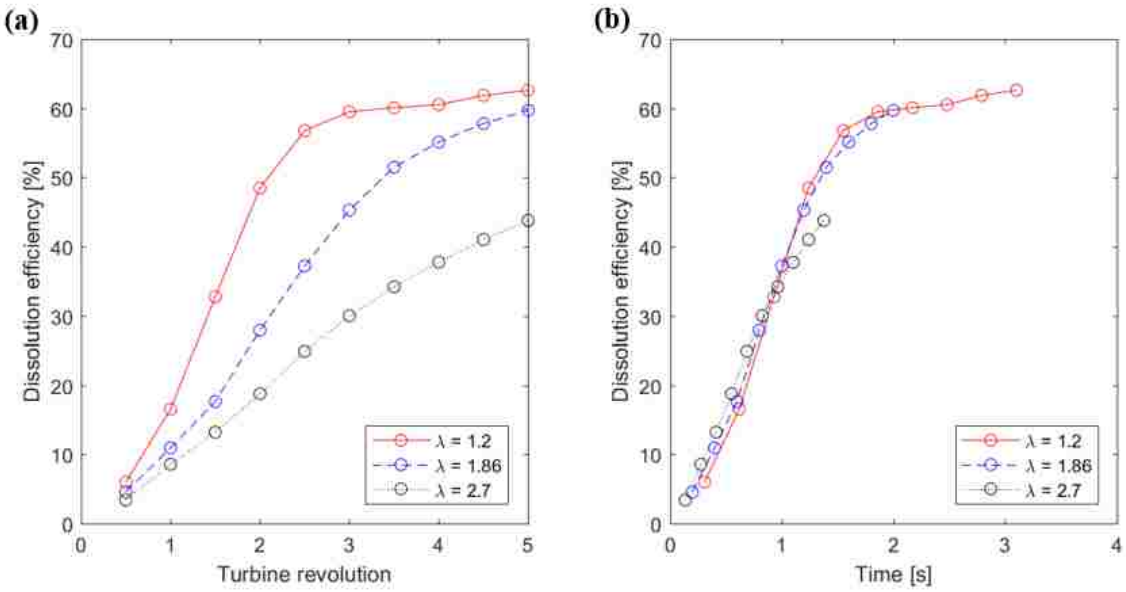

Figure 26. Oxygen dissolution efficiency for different tip-speed ratios as a function of (a) turbine revolution and (b) time.

Conclusions

During wet or dry seasons, the likelihood is high that hydrokinetic turbines will operate at a wide range of operational conditions. Computational fluid dynamics simulations of a pre-designed micro hydrokinetic turbine were performed at the design and off-design operating conditions with and without aeration. Single-phase and multiphase simulations were conducted at three different tip-speed ratios as λ = 1.2, λ = 1.86 and λ = 2.7 by employing LES approach. In this study, air was injected from the hub surface to the turbine downstream and the oxygen mass transfer from air to water was investigated for design and off-design operating conditions. This study shows that hydrokinetic turbine systems can be used effectively for aeration purposes.

Flow separation from the blade edges occurred at the tip-speed ratio lower than that at the turbine's design point (λ = 1.2). With a momentum mixing induced by the flow

separation at λ = 1.2 and intensive hub and blade root vortices at λ = 1.2 and λ = 1.86, the air injected from hub surface spread more in the radial direction as compared to that at λ = 2.7. Presence of air in a wider region at tip-speed ratio of 1.2 and 1.86 provided expanded living space with desired level of dissolved oxygen near wake region for the aquatic life. Moreover, the oxygen dissolution efficiency was higher at λ = 1.2 and λ = 1.86 as compared against that at λ = 2.7.

The effect of aeration on the turbine performance and the flow field was determined by comparing single-phase and multiphase results. The air introduction yielded 1.9% decrease in the nominal value of power output at λ = 1.2 and yielded 1.6% and 3.1% increase for λ = 1.86 and λ = 2.7 cases, respectively. The influence of aeration on the nominal value of thrust force was negligible for all three cases. At λ = 1.2, the deviation of power coefficient increased 56% with aeration, and the thrust deviation was also increased by 47%. Further, the deviation for the power and thrust coefficient at the design tip-speed ratio, λ = 1.86, were decreased by approximately 9% and 18% with aeration, respectively. Moreover, at higher tip-speed ratio, λ = 2.7, the deviation of both power and thrust coefficient were decreased more than 18% with aeration. Air injection resulted in early dissipation of vortex ropes created from each blade tip for tip-speed ratios of 1.86 and 2.7. The attenuation in the standard deviation of turbine performance parameters and the vortex suppression at the design and the higher tip-speed ratio after aeration increased the stability and minimized the vibration of the turbine after aeration. In contrast, the increase in the standard deviation at tip-speed ratio of 1.2 causes higher turbine vibration after the aeration. The level of power coefficient standard deviation at tip-speed ratio of 1.2 is still lower than

that observed at tip-speed ratios of 1.86 and 2.7 after the aeration. In contrast, the standard deviation of thrust coefficient at λ = 1.2 becomes higher than other cases after the aeration. Therefore, operating this hydrokinetic turbine at the lower tip-speed ratio is not desirable, especially with the application of aeration.

CHAPTER 5 COMPUTATIONAL STUDY OF AERATION FOR WASTEWATER TREATMENT VIA CENTRALLY VENTILATED PUMP-TURBINE

Large eddy simulations are performed on a modular pump-turbine to study the oxygen dissolution inside the draft tube. Central aeration is applied over the runner cone surface during turbine regime. Data regarding bubble size, void fraction and interfacial area concentration are presented to understand their influence on oxygen dissolution. Transient single phase and multiphase flow simulations are carried out to investigate the influence of air injection and oxygen dissolution on the flow field and the turbine performance. The multiphase simulation is conducted by using the mixture multiphase model. The averaged dissolved oxygen concentration inside the draft tube is evaluated to determine whether or not it is sufficient for an active aerobic microorganism activity for the wastewater treatment process. The influence of inlet bubble size on pump-turbine performance and dissolution characteristics is also investigated. The results presented in this chapter are published in Ref. [75].

Numerical Method and Computational Domain

The continuity and momentum equations are coupled by using a pressure based coupled algorithm. The pressure staggering option (PRESTO!) scheme is used for pressure interpolation and a bounded central differencing scheme is used for momentum equation discretization. A second order upwind scheme is used to discretize the equations of the interfacial area concentration and the species transport. The volume fraction equation

discretization is accomplished using the Quadratic Upstream Interpolation for Convective Kinematics (QUICK) scheme.

The computational domain of the predesigned and optimized pump-turbine [76] is comprised of stationary and rotational domains. The volute and the draft tube sub-domains are stationary and the runner sub-domain is rotational with a rotation rate of 1200 rpm. The pump-turbine is modeled considering the full six-blade runner. The geometry of the pump-turbine runner is depicted in Figure 27 and the plane and the meridional view of the runner is illustrated in Figure 28. The runner design variables are listed in Table 6.

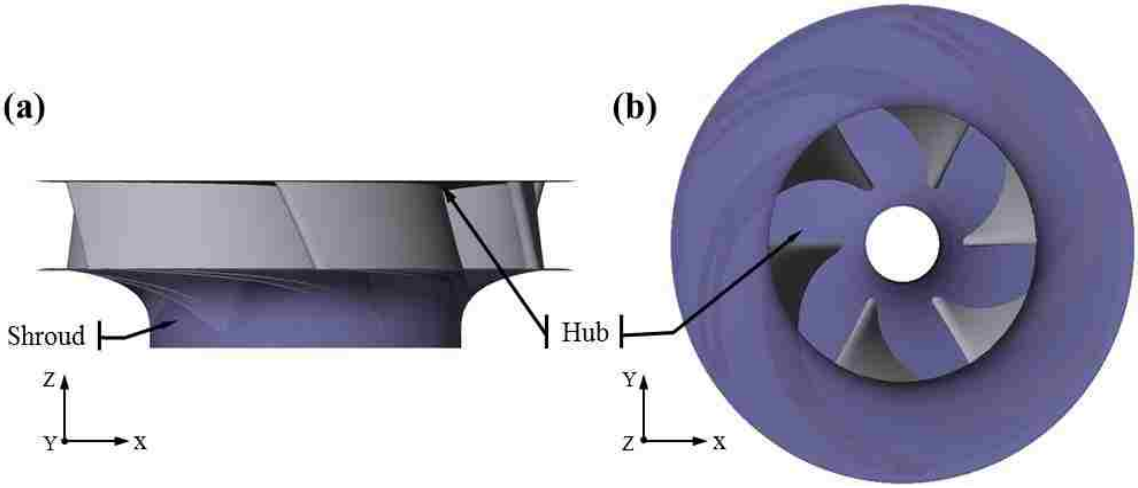

Figure 27. The geometry of predesigned pump-turbine runner.

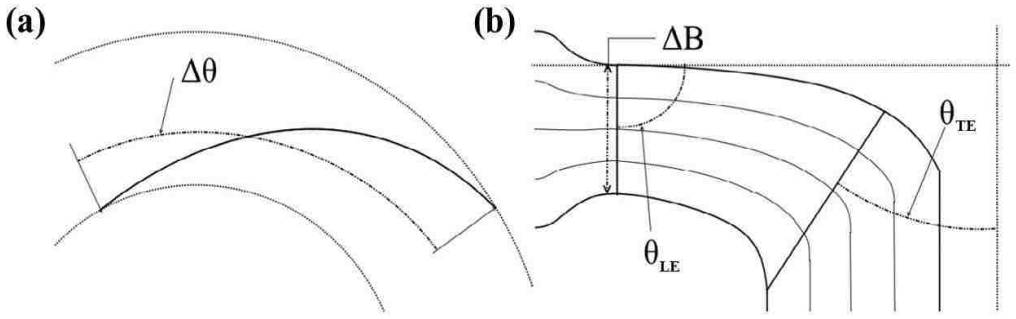

Figure 28. (a) Plane and (b) meridional view of the runner [76].

Table 6. Runner design variables.

Variable	***Description***	***Value***
ΔB	Gate height	67.133
$\Delta\theta_{hub}$	Blade wrap angle at the hub	74.729º
$\Delta\theta_{shroud}$	Blade wrap angle at the shroud	34.304º
θ_{LE}	Leading edge lean angle	88.697º
θ_{TE}	Trailing edge lean angle	37.669º

The entire computational domain with geometric details is depicted in Figure 29 . At the water inlet, a volumetric flow rate of $\dot{Q}_l$ =0.2 m^3/s is applied with a relative flow angle of 6º to the circumferential direction. Air is injected from the hub center in the axial direction with a volumetric flow rate of $\dot{Q}_g$ =2×10^{-3} m^3/s which is 1% of water flow rate. The air flow rate is suggested to be in the range of 1-3% of the water flow rate in Ref. [77]. A zero gradient condition normal to the boundary for all flow variables except for the pressure is applied at the outlet. A no-slip boundary condition is imposed on hub, shroud, blade and draft tube surfaces. The runner rotates with a rotation speed of 1200 rpm. Here, the pump-turbine operates at its design point.

The inlet bubble size is an important parameter that has profound influence on the dissolution characteristics, as documented by Gong et al. [78]. In the present study, two values of the inlet bubble size are considered: as 0.1 mm that is the lower bound studied by Gong et al. [78] and 0.05 mm. The majority of results are presented for the inlet bubble size of 0.1 mm. The bubble size in the flow domain is predicted at each iteration based on the IAC equation. In order to prevent unrealistic bubble size predictions inside the flow domain, lower and upper bounds are assumed for each inlet bubble sizes. Based on this assumption, the inlet bubble size of 0.1 mm varies in the range of 0.03 mm to 0.3 mm and

the inlet bubble size of 0.05 mm varies in the range of 0.015 mm to 0.15 mm in the flow field.

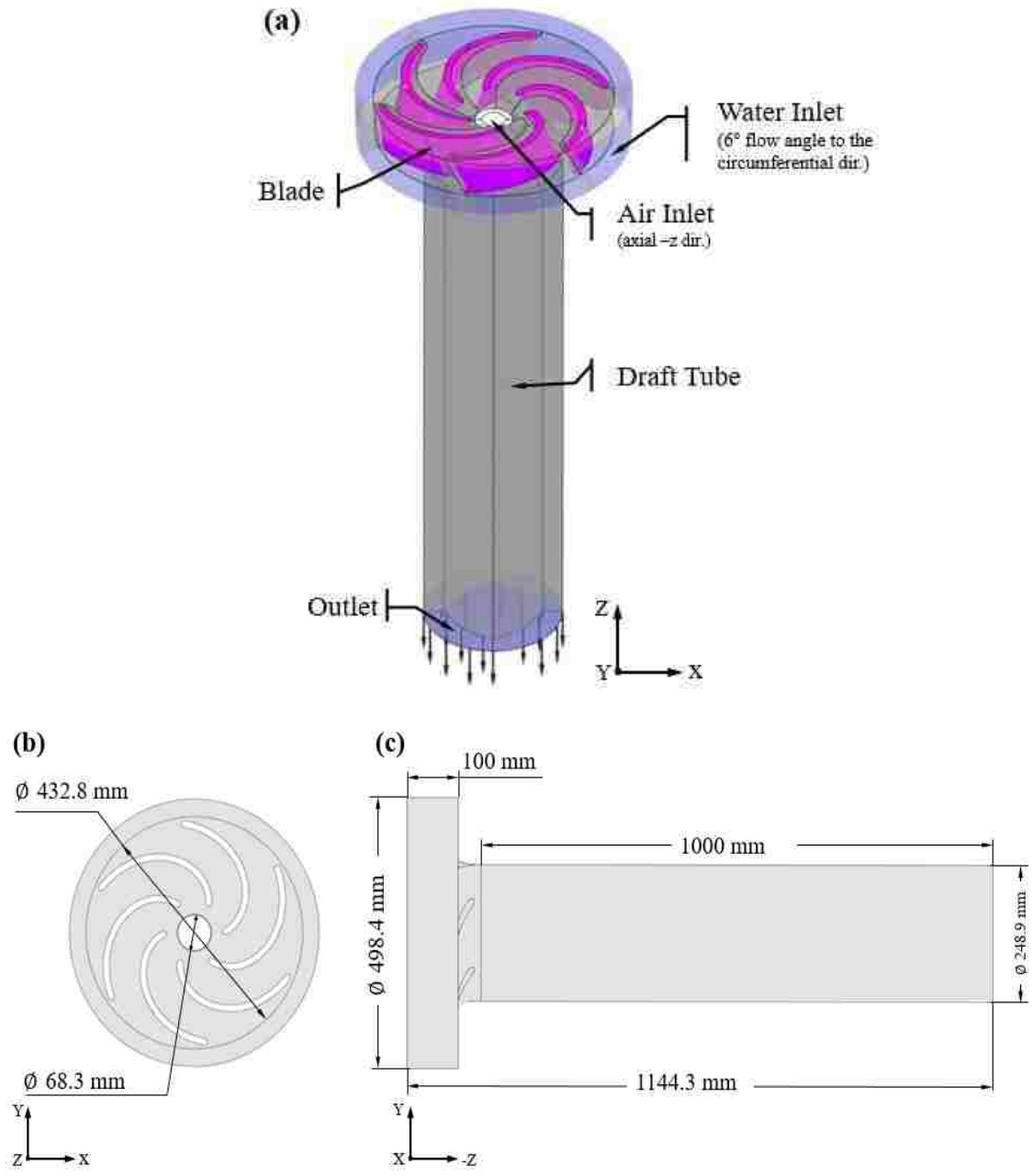

Figure 29. (a) The three-dimensional, (b) the top and (c) the side view of the computational domain with all components.

The numerical analysis is conducted at Reynold number of 1.06×10^7. The characteristic Reynolds number is defined by following equation based on the IEC 60193 Standard [79].

$$Re = \frac{\pi n {D_{ref}}^2}{60\nu_l} \tag{38}$$

where $n = 1200$ rpm is the runner rotation speed, $D_{ref} = 411.2$ mm is runner's reference diameter, and ν_l is the kinematic viscosity of the liquid phase. The reference diameter is defined as the blade tip diameter at the hub.

Results and Discussion

5.2.1 Spatial and Temporal Discretization

A spatial convergence study of single phase simulations was carried out by Schleicher and Oztekin [76] for the same blade design and computational domain dimensions. In their RANS simulations, a runner with six blades was modeled as a single blade passage with rotational periodicity at side boundaries and the draft tube was modeled as a full geometry. The number of cells for five different grid sizes were selected to be in the range of 10^5 to 9×10^6 for a single blade passage and the full draft tube. The mechanical power generation is presented as a function of a mesh size. The deviation in power generation obtained using 2.9×10^6 and 6.1×10^6 cells was 1.53% and the difference in power generation obtained using 6.1×10^6 and 9×10^6 elements was 0.51%.

Figure 30 depicts the mesh on the hub, near the blade trailing edge and on the blade surface. The mesh refinement is applied in regions closer to the blade surface, as depicted

in Figure 30(b), to resolve the boundary layer on the blade surface. In dispersed bubbly flows with LES modeling, the Milelli condition regarding the limitation on the cell size should also be considered. The cell size must be sufficiently small to capture turbulent flow structures in the flow field, on the other hand the cell size must be large enough to prevent divergence due to cell size-bubble size restriction. Both requirements are addressed within the meshing of the draft tube. The discretization of the full pump-turbine domain is achieved using structured-hexahedral mesh including 16.7×10^6 cells by considering the mesh independence study conducted by Schleicher and Oztekin [76] and the bubble size-cell size restriction.

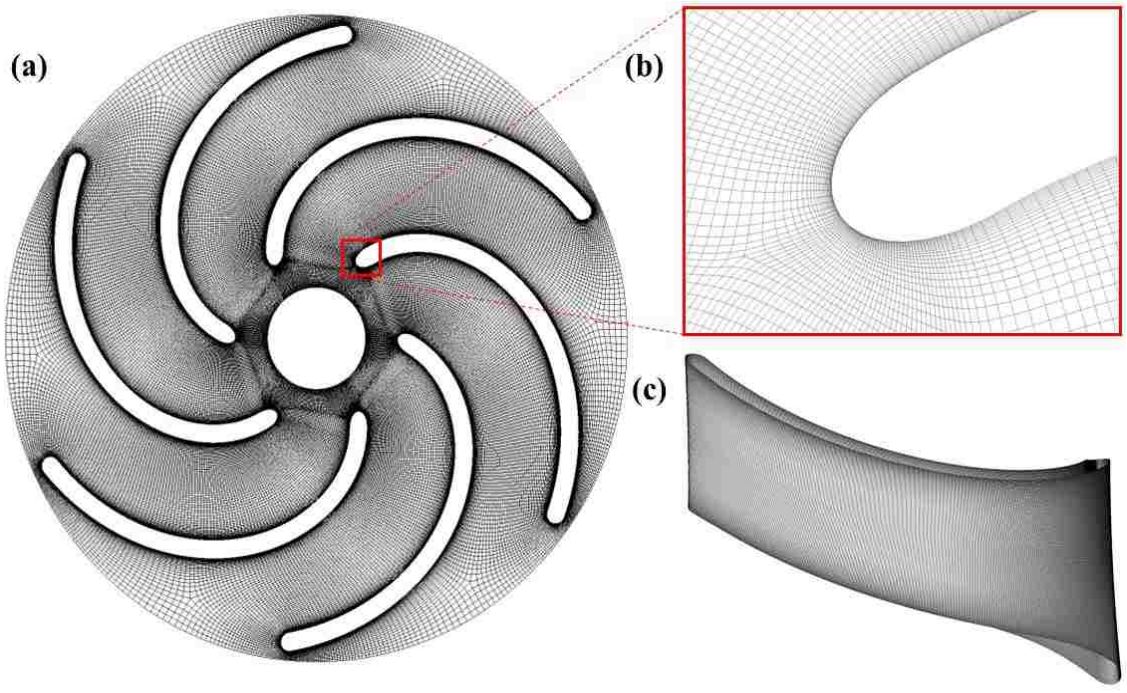

Figure 30. The mesh (a) on the hub, (b) near the blade trailing edge and (c) on the blade surface.

A dimensionless wall distance in a wall-restricted flow is described as $y^+ = u_* y/\nu$. Here, u_* is the velocity at the nearest wall and y is the distance to the first grid point from

the wall. The instantaneous contour of y^+ after 14 revolutions is illustrated in Figure 31(a). The maximum y^+ value is calculated to be 58.72 which occurs at small number of cells on the blade surface. The time and area-averaged y^+ value is predicted to be nearly 12 on the blade surface in the single-phase simulation. The low value of y^+ indicates that the quality of mesh is good. In addition to cell size, the time step size is determined to ensure that the runner rotates roughly 0.8° per time step which leads to average Courant–Friedrichs–Lewy condition (CFL) number of roughly 0.5 on the blade surface. The CFL number defines the behavior of the fluid particles moving through the cells. When the CFL number is equal to or less than unity, the fluid particles move from cell to cell properly. Otherwise, the fluid particles skip some cells in the domain which can lead to a numerical instability and inaccurate results. The limitation on the CFL number arises in the explicit numerical analysis, higher CFL number is tolerable in the implicit solutions. Here, the partial differential equations are solved with an implicit solver for which the CFL number less than 5 provides sufficient accuracy [80, 81]. The contour of CFL number on the blade surface is depicted in Figure 31(b) and only a few cells near the blade trailing and leading edges have the CFL number higher than 5.

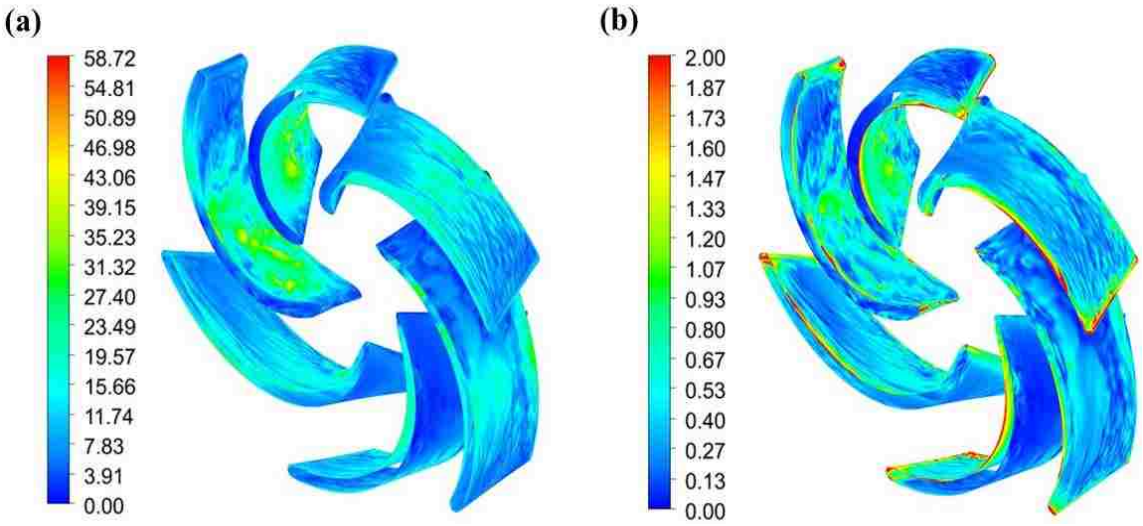

Figure 31. The instantaneous contour of (a) y^+ value and (b) CFL number after 14 revolutions in single phase simulation.

5.2.2 Single Phase and Multiphase Simulations

Here, the effectiveness of the aeration process in the pump storage systems is investigated. The evolution of dissolved oxygen in the draft tube and the influence of aeration on the turbulent flow structure are characterized. The single phase flow simulation is conducted to evaluate the influence of air injection on the runner performance and the flow field.

Instantaneous velocity and vorticity contours are illustrated on a central plane passing through the draft tube in Figure 32 after 14 revolutions. The images in the left column of each subplot shows the results of the single-phase simulation and the images in the right column of each subplot depicts the results obtained by the multiphase simulation. There is a noticeable difference in the flow field due to the existence of air phase. The low speed is observed along the centerline of the draft tube in both single phase and multiphase flows, see Figure 32(a). The air injection expands low velocity region around the centerline.

The magnitude of vorticity is greater, and the size of eddies is smaller in single phase flows, see Figure 32(b). The suppression of vorticity by air injection could be vital in these systems due to the correlation between vortical activities and flow induced vibration.

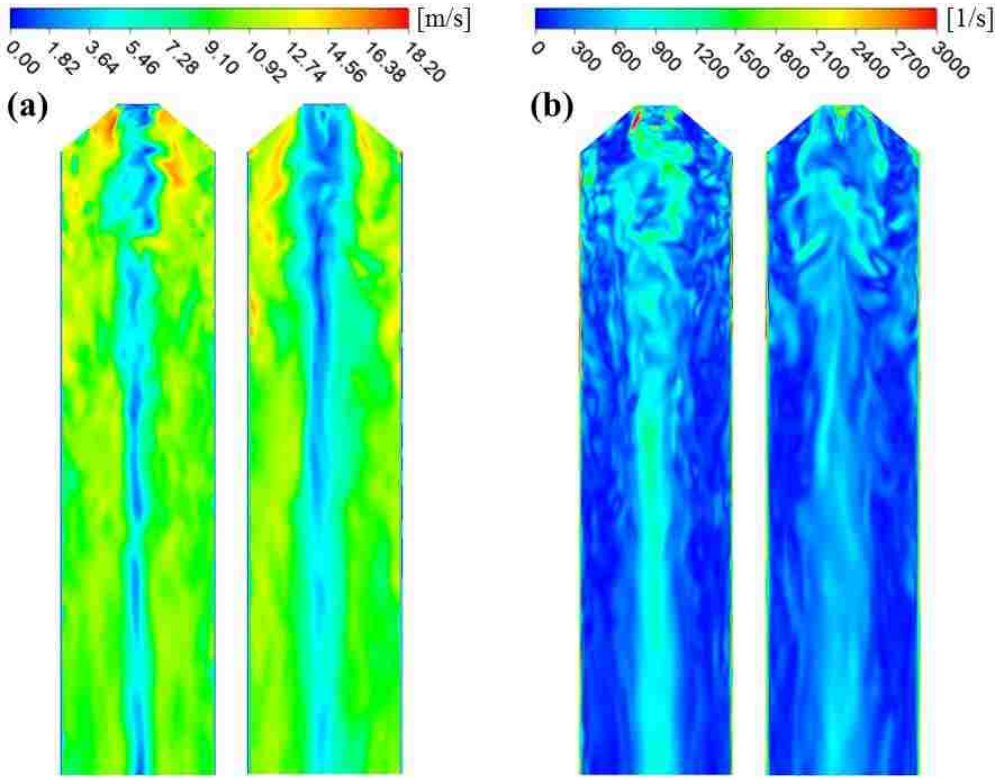

Figure 32. The instantaneous (a) velocity and (b) vorticity contours on a central, vertical plane passing through the draft tube after 14 revolutions. The left column and the right column of each subplot depicts the single phase and the multiphase results with inlet bubble size of 0.1 mm, respectively.

Figure 33(a)-(b) depicts the instantaneous bubble size and the air volume fraction inside the draft tube, respectively. The interfacial area concentration based on both bubble size and air volume fraction is depicted in Figure 33(c), see Eq. (15). The bubble size is larger in the region near the tube center and decreases an order of magnitude approaching to the tube surface. The inlet bubble size in this figure is 0.1 mm. The presented bubble size contour reveals that the bubble size in the flow domain is generally larger than the

inlet bubble size which is an indication of dominant coalescence effects in the flow field. The air volume fraction at the air inlet is unity and it is much greater in the region near the center of the draft tube. The air volume fraction reduces in axial flow direction due to blending with the free water stream coming from the runner region and the mass transfer from air to water. Moreover, the cross-section area at the air inlet is smaller than that at the draft tube. Since the air diffuses in the radial direction, air volume fraction is diluted naturally.

The instantaneous contour of dissolved oxygen level is illustrated in Figure 33(d). The DO concentration is nearly saturated near downstream of the runner and it decreases in the stream-wise direction. The higher dissolution in the near wake region is attributed to the higher air volume fraction in the region. As described in Eq. (15) and Eq. (23), the oxygen mass transfer is proportional to the air volume fraction. The other contributing factor is the high intensity swirling in the region induced by the blade rotation which promotes momentum mixing and enhance dissolution. This hypothesis is verified by the fact that higher dissolution is observed in regions with higher vortical activities, see Figure 34 and Figure 35. Figure 33(e) illustrates the mass fraction of oxygen in air which decreases in the flow direction due to the oxygen transfer from air to water.

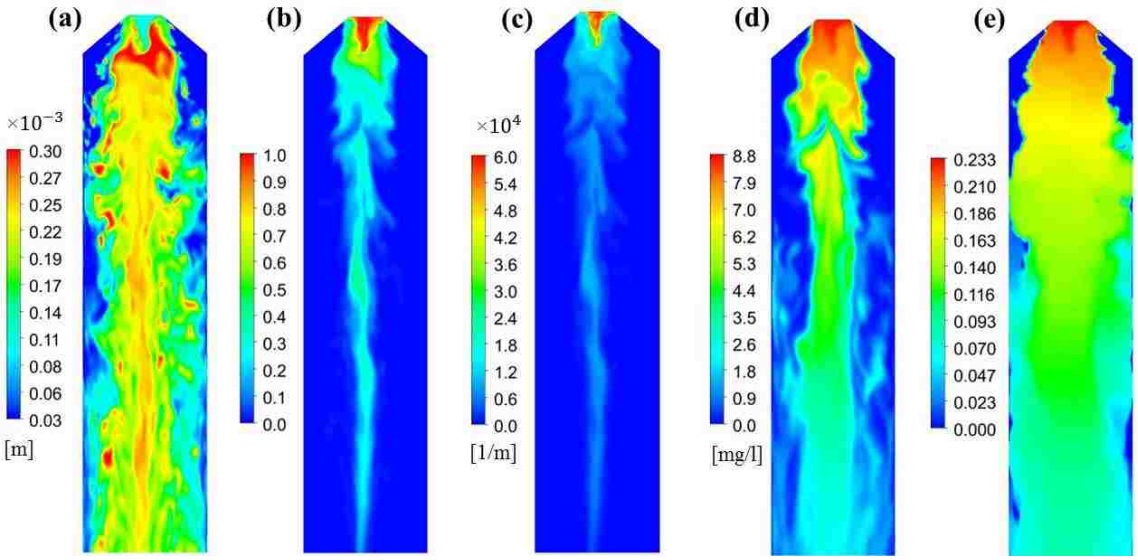

Figure 33. The instantaneous contours of (a) bubble size, (b) air volume fraction, (c) interfacial area concentration, (d) dissolved oxygen concentration and (e) oxygen mass faction in air on a central, vertical plane passing through the draft tube after 14 revolutions for inlet bubble size of 0.1 mm.

Figure 34 and Figure 35 illustrate the contours of instantaneous vorticity and dissolved oxygen concentration at a central plane of the draft tube for various runner revolutions, respectively. The multiphase simulation is initialized by assuming water without dissolved oxygen in the flow domain. The DO reaches the outlet after roughly 4 runner revolutions. The maximum, nearly saturated DO concentration is observed near the air inlet and the high DO region expands in the axial direction with increasing runner revolution. Quasi-periodic state in the draft tube is reached after about 11 revolutions as evidence from the evolution of vorticity field and dissolved oxygen concentration depicted in Figure 34 and Figure 35. It is also clear that the higher oxygen dissolution occurs in the regions having higher vorticity magnitude. The spatial distribution of dissolved oxygen and its evolution are correlated to the vorticity field and its evolution. This conclusion

reveals that the turbulent momentum mixing downstream the runner dominates the dissolution and the mass transport process.

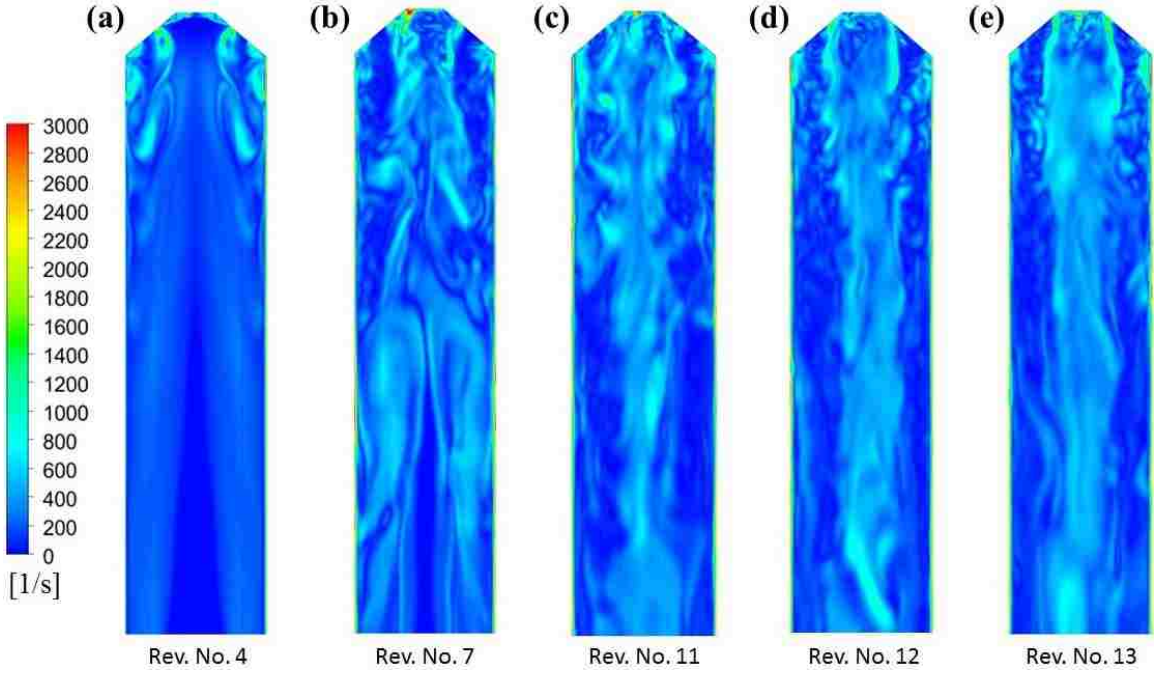

Figure 34. The instantaneous vorticity contours on a central, vertical plane passing through the draft tube at different runner revolutions in multiphase simulation with inlet bubble size of 0.1 mm.

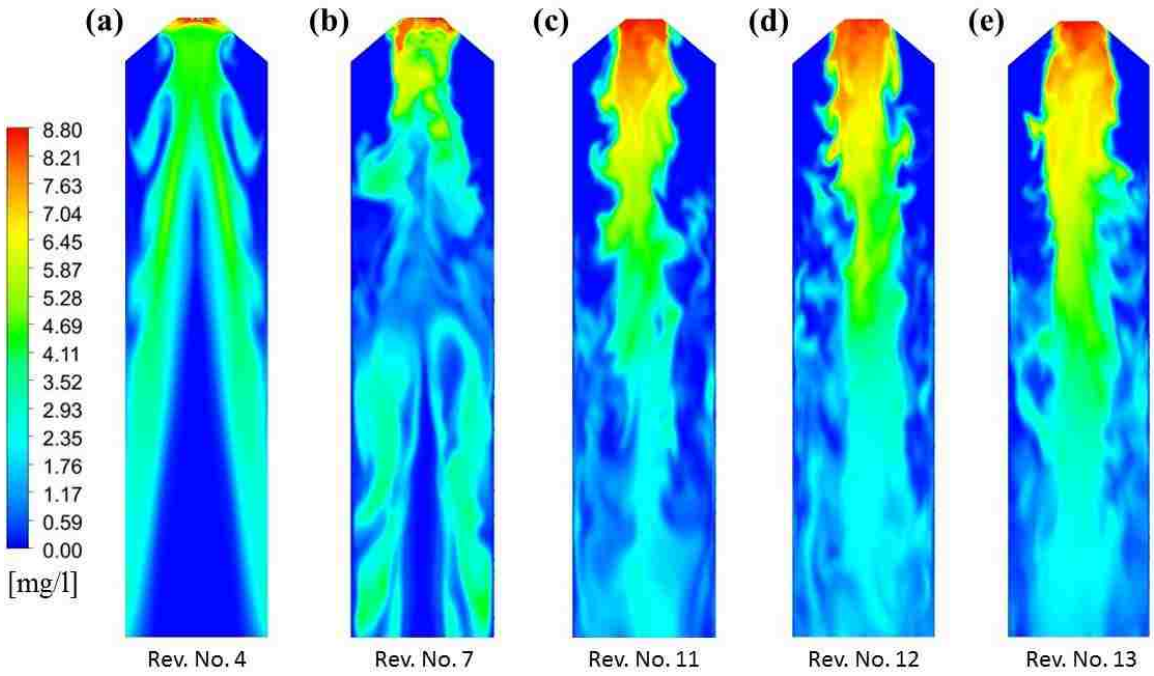

Figure 35. The instantaneous contours of dissolved oxygen concentration on a central, vertical plane passing through the draft tube at different runner revolutions for inlet bubble size of 0.1 mm.

The dissolution efficiency (%) and the volume-averaged dissolved oxygen (mg/l) inside the draft tube is listed in Table 7 at various runner revolutions. Dissolution efficiency is defined as the ratio of total amount of dissolved oxygen to total amount of dissolved and undissolved oxygen inside the draft tube. The dissolution efficiency reduces as air moves towards the outlet and asymptotes to 25% as the number of revolution increases. The oxygen dissolution is greater near the air inlet region due to the higher momentum mixing induced by blade motion. Another reason for lower level of dissolution away from the air inlet is the increase in bubble size due to the coalescence effects inside the draft tube and the decrease in air volume fraction. It is well-known that the rate of dissolution reduces with increasing bubble size and decreasing air volume fraction. The volume-averaged DO concentration is obtained to be in the range of 1.2-1.4 mg/l inside the draft tube. A value

of 1 to 2 mg/l is reported to be sufficient for active aerobic microorganism activity for wastewater treatment processes [82]. The pump-turbine system could aerate the wastewater effectively for specified operating conditions.

Table 7. The dissolution efficiency and the amount of volume-averaged DO at various values of runner revolution for inlet bubble size of 0.1 mm.

Runner Rev.	***8.0***	***8.8***	***11.0***	***12.0***	***13.0***	***14.0***	***15.0***
Dissolution efficiency (%)	32.3	30.5	27.0	26.3	25.4	25.0	24.8
Volume-averaged DO (mg/l)	1.23	1.20	1.28	1.32	1.37	1.42	1.42

Figure 36(a)-(b) show the instantaneous iso-surface of Q-criterion at a constant value of Q=29×10^3 1/s^2 for single phase and multiphase simulations, respectively. Figure 36(c) illustrates the iso-surface of air volume fraction at a constant value of 0.01. Figure 36(d) depicts the iso-surface of dissolved oxygen concentration in liquid phase at a constant value of 2 mg/l after 14 revolutions. It is clear from Figure 36(a)-(b) that the smaller vortical structures downstream the runner and single central vortex rope are observed in both single phase and multiphase simulations. The vortical structures in single phase simulation is smaller as compared against multiphase case since the air injection assists with the vortex suppression as explained before within Figure 32(b). The air is injected from the upstream draft tube at center and moves at the centerline towards the outlet, see Figure 36(c). It is known that the oxygen mass transfer occurs from air to water and therefore the greater DO concentration is observed within the same region of greater air concentration, as depicted in Figure 36(c)-(d).

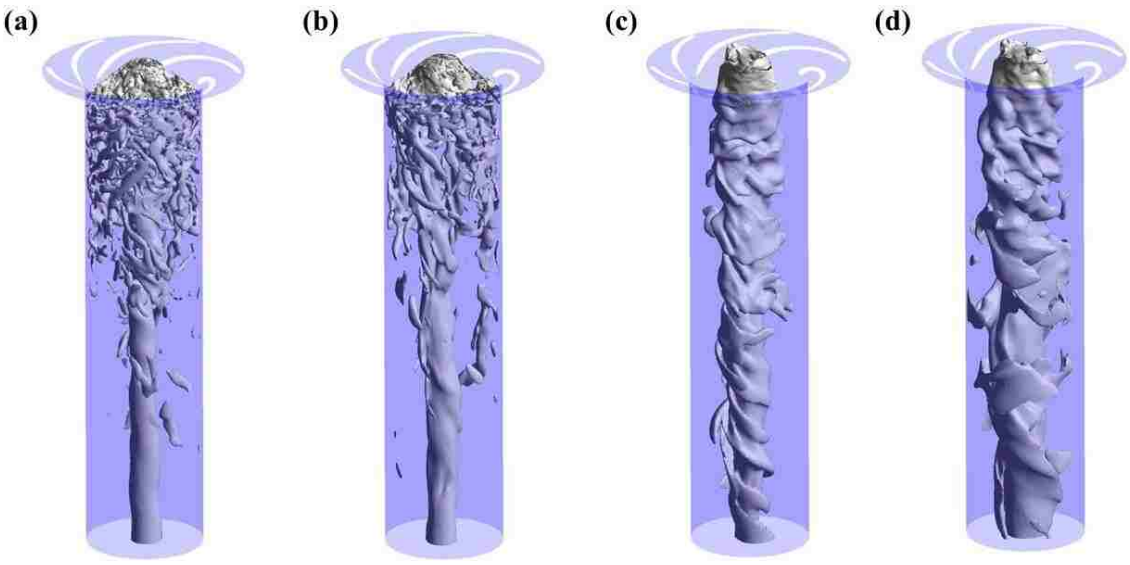

Figure 36. The instantaneous (a) iso-surface of Q-criterion at a constant value of 29×10^3 $1/s^2$in single phase simulation, (b) iso-surface of Q-criterion at a constant value of 29×10^3 $1/s^2$ in multiphase simulation, (c) the iso-surface of the air volume fraction at a constant value of 0.01 and (d) the DO concentration at a constant value of 2 mg/l after 14 revolutions for inlet bubble size of 0.1 mm.

Figure 37 shows power generation as a function of the runner revolution for both (a) single phase and (b) multiphase simulations. The time signature demonstrates that the amplitude of power generation obtained by single phase flow simulations is larger than that of multiphase flow simulations. This observation suggests that the air admission provides more stable runner operation. Both simulations are carried out for several number of runner revolutions by ensuring that the turbine operation reaches quasi-periodic state. Single phase simulation is carried out for 25 revolutions of flow time while the multiphase simulation is carried out for 15 revolutions of flow time.

The power generation of single phase flows is calculated to be 56.7±1.0 kW with the full runner geometry while Schleicher and Oztekin [76] reported the runner power generation to be roughly 57.5 kW for a single blade passage approximation. Here, ±1.0 kW represents the standard deviation ($\pm\sigma$) of the generated power. The power generation

reported in Schleicher and Oztekin [76] differs only 1.4% compared to the power generation predicted here by more robust numerical simulations. This confirms the results of Schleicher and Oztekin [76] obtained by single blade passage approximation. Multiphase simulations including aeration process predict the turbine power output as 54.7±0.6 kW. The nominal value of power generation is reduced only by 3.5%. It is demonstrated here that aeration can be applied in the pump-turbine without posing any major penalty in the power generation. In addition to the comparison of nominal value of power output, the standard deviation of transient power generation is decreased roughly 40% with aeration. The deviation reduction with aeration is consistent with the suppression of vorticity that is observed in multiphase simulation in Figure 32. The decrease in the fluctuations reveals less vibrational and more stable operation of pump-turbine with aeration.

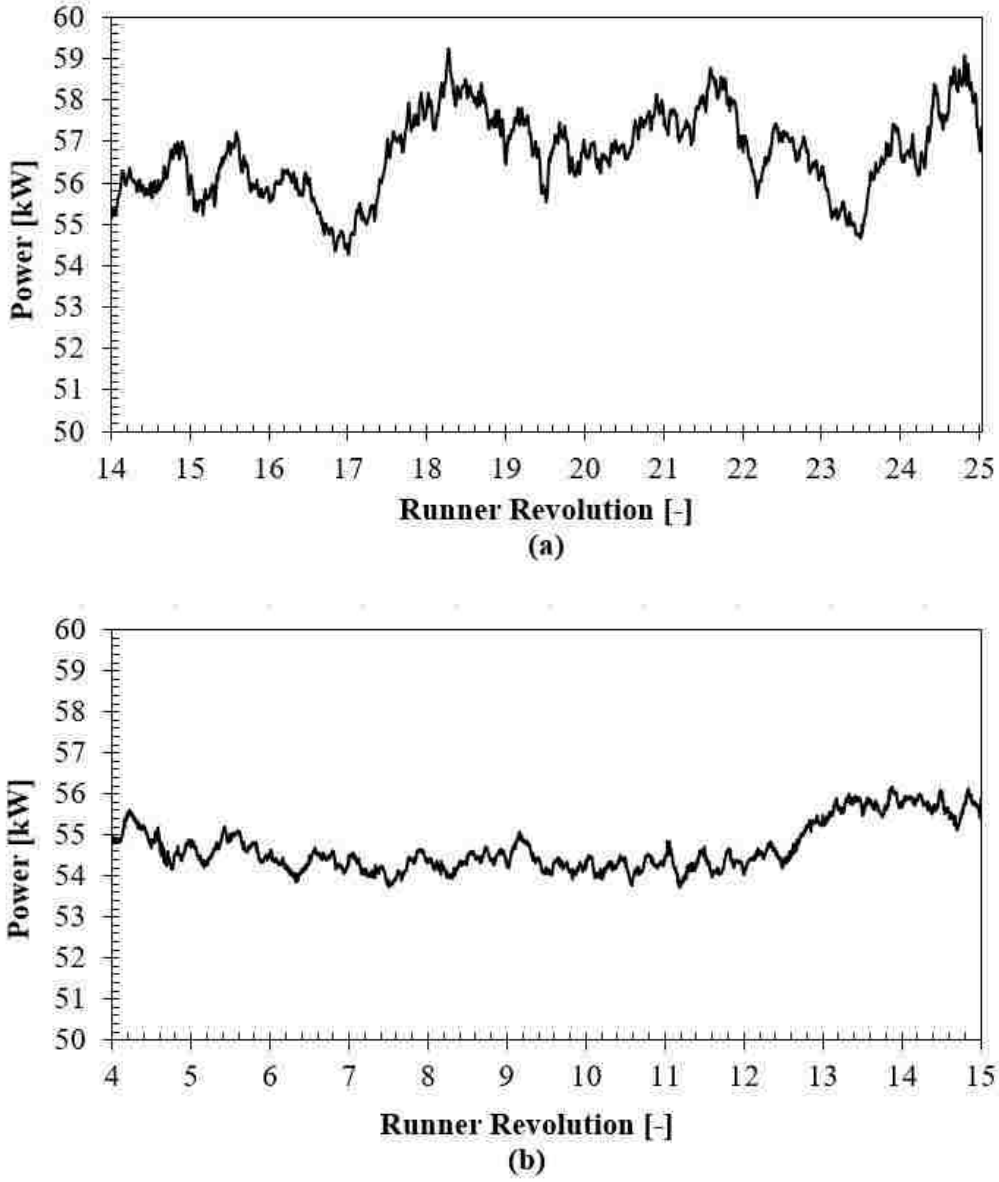

Figure 37. Power generation as a function of the runner revolution for (a) single phase and (b) multiphase simulation with inlet bubble size of 0.1 mm.

5.2.3 The Effect of the Inlet Bubble Size

In order to determine the influence of inlet bubble size on oxygen dissolution, one additional simulation is conducted with inlet bubble size (d_i) of 0.05 mm by keeping air mass flow rate constant. Eqs. (15) and (26) reveal that the decrease in the bubble size

increases the interfacial area concentration (α_i) and the mass transfer coefficient (k_l). The amount of mass transferred from air to water is predicted as a function of α_i and k_l as shown in Eq. (23). Figure 38 depicts the contours of air volume fraction and DO concentration for different inlet bubble sizes. In both cases, air is concentrated in the central region, however when the inlet bubble size is smaller, air disperses further in radial direction near the air inlet region. As a result, the higher dissolved oxygen is observed in a wider region for d_i=0.05 mm. Overall spatial and temporal characteristics of the dissolved oxygen in the draft tube is similar in both cases. Dissolution rate is greater near the injection site and reduces gradually in the stream-wise direction, as depicted by images shown in Figure 38.

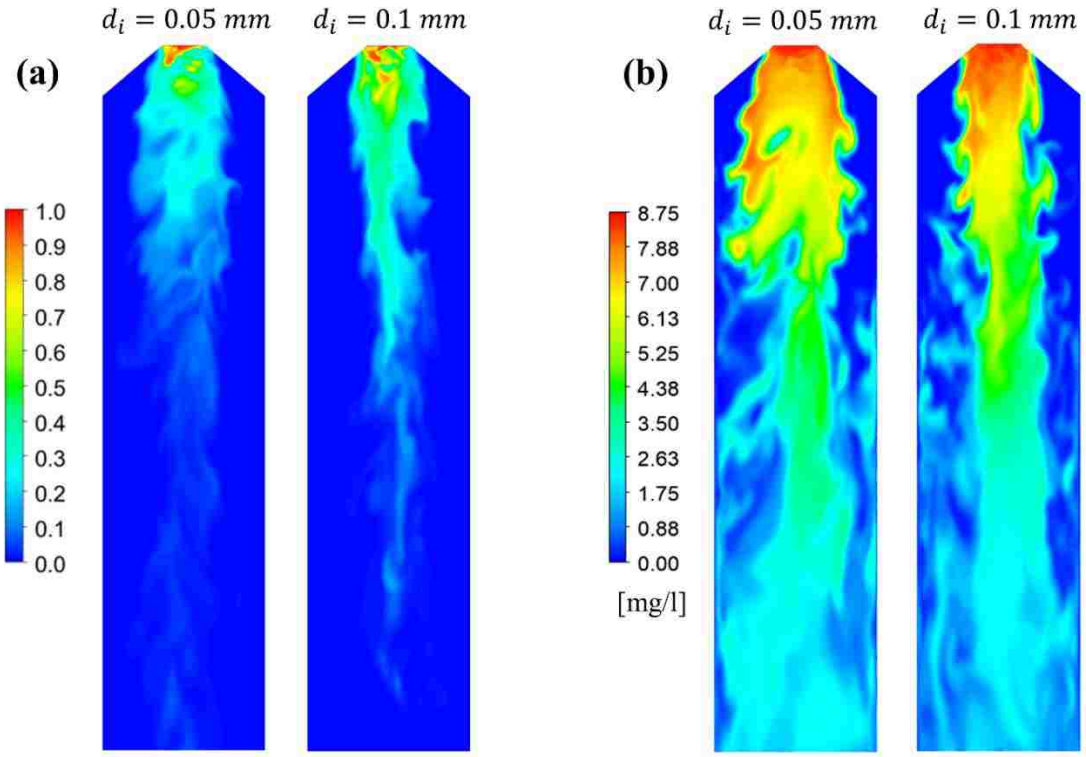

Figure 38. The instantaneous contours of (a) air volume fraction and (b) dissolved oxygen concentration for different inlet bubble sizes on a central, vertical plane passing through the draft tube after 12 revolutions.

The dissolution efficiency and the amount of volume-averaged DO is calculated for d_i=0.05 mm and is compared against results obtained for d_i=0.1 mm at various runner revolutions in Table 4. As expected, higher dissolution efficiency and greater amount of DO concentration inside the draft tube is predicted for d_i=0.05 mm. Reducing the bubble size from d_i=0.1 mm to d_i=0.05 mm enhanced the dissolution efficiency roughly 30% and increased the amount of volume-averaged DO approximately 27%. In addition to the mass transfer performance comparison, the influence of inlet bubble size on turbine performance is also investigated. Less than 0.3% improvement is observed on turbine performance as the inlet bubble size is decreased from 0.1 mm to 0.05 mm.

Table 8. The influence of bubble size on dissolution efficiency and the amount of volume-averaged DO.

Runner Revolution		***8.0***	***8.8***	***10.1***	***11.0***	***12.0***
Dissolution efficiency (%)	$d_i = 0.1\ mm$	32.3	30.5	28.1	27.0	26.3
	$d_i = 0.05\ mm$	36.0	35.3	34.7	34.7	34.3
Volume-averaged DO (mg/l)	$d_i = 0.1\ mm$	1.23	1.20	1.24	1.28	1.32
	$d_i = 0.05\ mm$	1.32	1.38	1.50	1.60	1.68

Conclusions

Transient single phase and multiphase CFD simulations of predesigned and optimized modular pump-turbine were performed. The multiphase simulation implemented the mixture model. Air was injected during turbine operation from the runner cone surface centrally. The purpose of present study was to determine the aeration capability of the pump turbine for wastewater treatment and to evaluate the influence of central aeration on pump-turbine performance.

The bubble size inside the draft tube was predicted to be larger than the inlet bubble size probably due to the dominant coalescence effects. The dissolution characteristics are strongly dependent on the inlet bubble size. Reducing the inlet bubble size from 0.1 mm to 0.05 mm provided roughly 30% improvement in the dissolution efficiency, roughly 27% increase in the amount of volume-averaged dissolved oxygen and less than 0.3% increase in the turbine power output.

The time evolution of the dissolved oxygen concentration distribution in the draft tube was characterized. Dissolution of oxygen was higher in regions with increased vortical activities; proving that enhanced momentum mixing promotes dissolution. The volume-averaged DO level in the draft tube was calculated to be 1.2 mg/l to 1.4 mg/l. For effective wastewater treatment, the dissolved oxygen was desired to be in the range of 1-2 mg/l. The pumped-storage scheme considered here can be used to treat the wastewater.

The time signature of power generation for both single phase and multiphase simulations were compared. The amplitude and the fluctuation of power generation in single phase simulation was more than that of multiphase case. This observation and the vortex suppression in the flow field suggested that the air admission might assist with the vibration reduction in pump-turbine systems. The mean power generation was reduced from 56.7±1.0 kW to 54.7±0.6 kW when aeration was applied during turbine operation. This study indicated that aeration for wastewater treatment can be achieved via a pump-turbine system effectively with a minor reduction in system performance.

CHAPTER 6 COMPUTATIONAL STUDY OF AERATION FOR WASTEWATER TREATMENT VIA PERIPHERALLY VENTILATED PUMP-TURBINE

In this Chapter, aeration was performed peripherally from the continuous and discrete surfaces near the inlet of the draft tube. The simulations were performed using mixture multiphase model and LES turbulence model. The influence of aeration on pump-turbine performance is assessed by comparing power generation predicted by the multiphase and single flow simulations. The mean DO concentration and dissolution efficiency inside the draft tube are predicted and compared against the results obtained with central aeration. Moreover, the influence of aeration on pressure pulsation near the draft tube wall is studied and presented for both central and draft tube aeration.

Configuration of Aeration Methods

The detailed description of the computational domain and the runner geometry is presented in the chapter 5. The set of boundaries, initial conditions and the operating conditions are also described in the chapter 5. The air is injected from three types of orifice: the central injection, a continuous peripheral ring and discrete orifices along the surface of the draft tube, see Figure 39. The air is injected peripherally with a 30° angle, as shown in Figure 39(b)-(c).

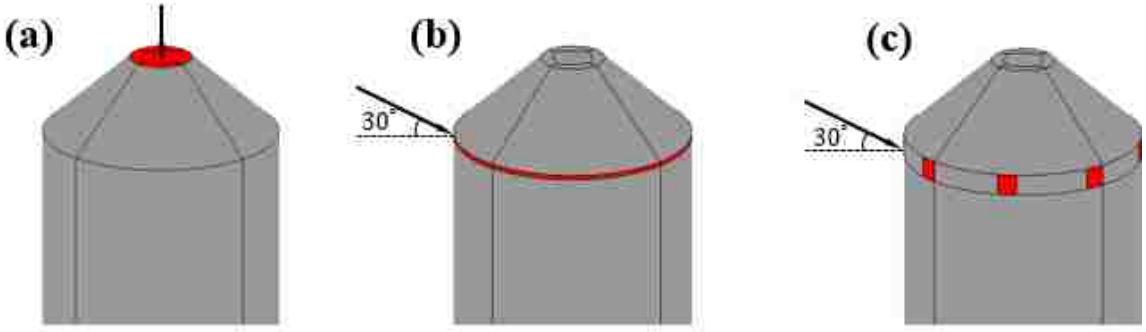

Figure 39. The location and direction of air injection for (a) central aeration, (b) continuous surface draft tube aeration, and (c) discrete surface draft tube aeration.

Results and Discussion

Results of continuous and discrete surface draft tube aeration are presented. The single phase and central aeration results are presented and discussed in the chapter 5. Figure 40 depicts instantaneous contours of velocity magnitude, pressure and vorticity magnitude along the central, vertical surface in the draft tube with discrete phase draft tube aeration after 10 revolutions. Similar contours are predicted for all three types of aeration. A central vortex rope with higher vorticity magnitude at the center of draft tube is observed. The lower velocity magnitude and pressure is observed inside the vortex rope. Velocity increases from the center to the surface of the vortex rope within the upper portion of the draft tube. The pressure increases in the radial direction from the center to the surface of the draft tube. Smaller flow structures induced by the runner motion are observed between the central vortex rope and the draft tube surface near the entrance of the draft tube, see Figure 40(c).

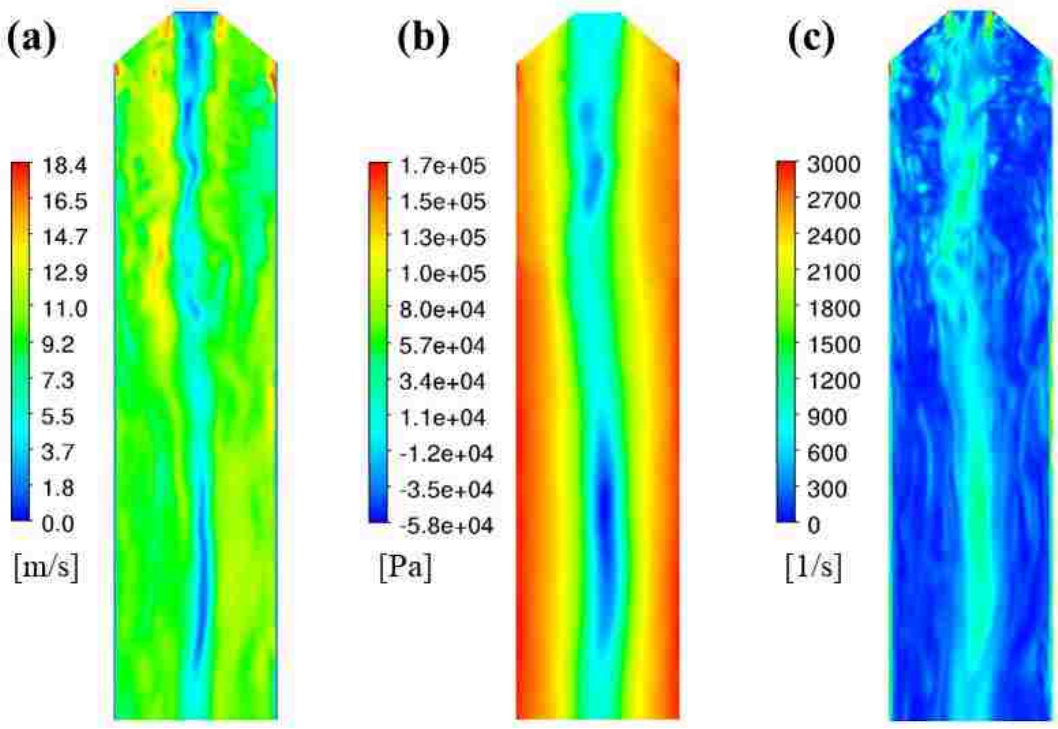

Figure 40. Instantaneous contour of (a) velocity, (b) pressure and (c) vorticity after 10 revolutions with discrete surface draft tube aeration.

The local bubble size, the air volume fraction, and the interfacial area concentration are illustrated in Figure 41 for both continuous and discrete surface draft tube aeration. The instantaneous contours are acquired after 10 revolutions. The inlet bubble size is set to be 0.1 mm. Almost uniform bubble size is predicted inside the draft tube except for a small number of cells near the air inlet with the continuous surface DT aeration. However, a wide range of bubble size is obtained within the discrete surface DT aeration. The bubble size reaches to 0.3 mm near the air inlet due to the intensive coalescence effects induced by bubble-bubble random collision and(or) wake entrainment. Since air is introduced from the draft tube surface where the centrifugal forces are greater, the air moves near the draft tube surface. Better mixing is obtained within the discrete surface aeration since a larger amount of air is convected and diffused in the radial direction towards the center, see Figure 41(b).

The maximum air volume fraction is revealed near the air inlet region and it dilutes in the axial direction towards the outlet due to the convection and diffusion in radial direction in both cases. The interfacial area concentration is a function of bubble size and the air volume fraction. The amount of mass transferred is directly proportional to the interfacial area concentration. Higher interfacial area concentration yields higher dissolution.

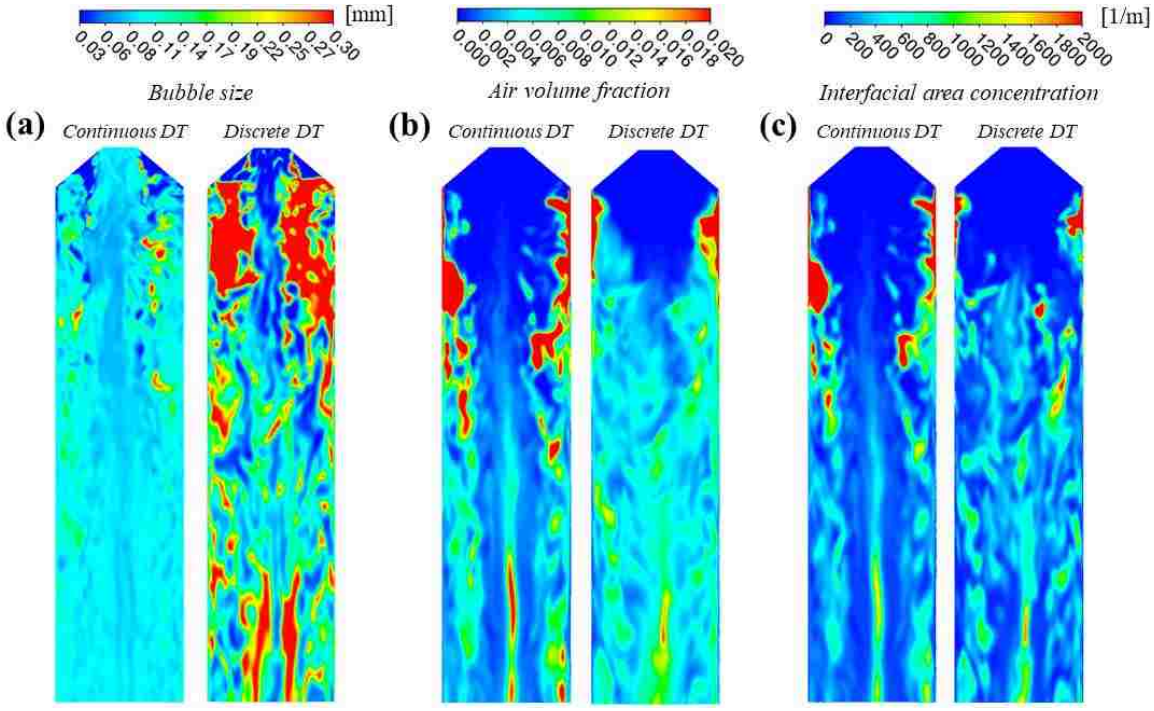

Figure 41. Instantaneous contours of (a) bubble size, (b) air volume fraction and (c) interfacial area concentration after 10 revolutions. For each part, left and right images represents the results of continuous and discrete surface draft tube aeration, respectively.

The instantaneous concentration of dissolved oxygen and the mass fraction of undissolved oxygen is illustrated in Figure 42 after 10 revolutions. The highest dissolution is obtained near the air inlet, due to higher air volume fraction and intensive vortical activity in this region, see Figure 40. Although the bubble size and air volume fraction distribution are predicted to be different for both continuous and discrete draft tube aeration cases in Figure 41, their cumulative contribution yields similar dissolved oxygen concentration

field. Moreover, the undissolved oxygen mass fraction (mass fraction of oxygen in air) field is predicted to be similar for both cases as well, see Figure 42(b). The mass fraction of oxygen inside the air reduces towards the outlet due to the oxygen mass transfer from air to water.

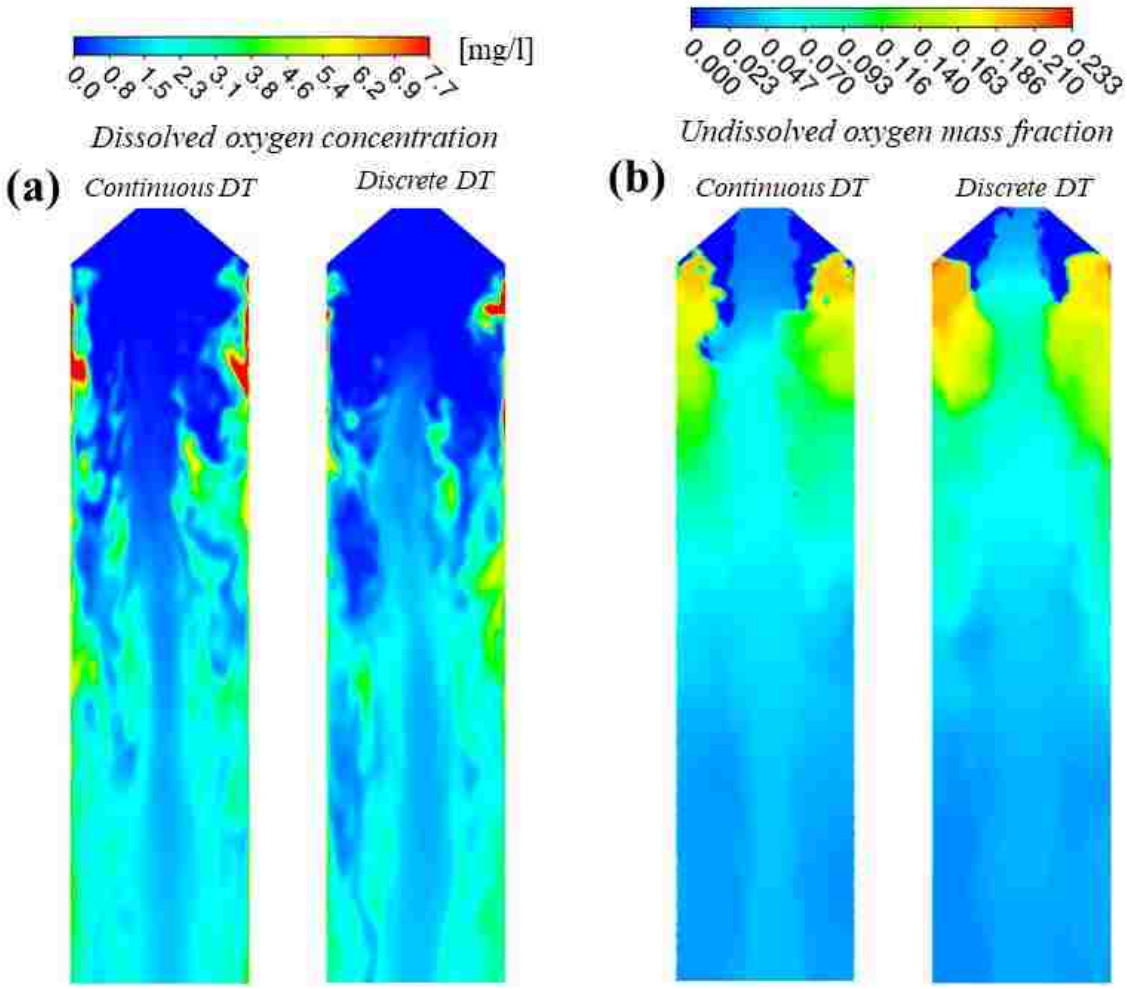

Figure 42. Instantaneous contours of (a) dissolved oxygen concentration and (b) undissolved oxygen mass fraction after 10 revolutions. For each part, left and right images represents the results of continuous and discrete surface draft tube aeration, respectively.

The time averaged contours of air volume fraction, dissolved oxygen concentration, and undissolved oxygen mass fraction are illustrated in Figure 43 for the discrete surface

DT aeration. Time averaging is carried out from 3.6^{th} revolution to 10^{th} revolution. Distribution of air volume fraction and dissolved/undissolved oxygen mass fraction is nearly axisymmetric, as shown in Figure 43. Near the inlet of the draft tube there is a thin layer of air volume fraction and dissolved oxygen concentration near the wall of the draft tube. Air is concentrated along the draft tube surface near the inlet region due to higher swirling effect induced by the runner. Boundary layer thickens away from the inlet region with air dispersing radially as the swirling effects fades. The dissolved oxygen concentration distribution becomes nearly uniform in the region toward the outlet. The dissolved oxygen concentration reaches 1.5-2.0 mg/l level near the outlet. In the region close to the inlet of the draft tube, the undissolved oxygen mass fraction is predicted to be the highest as expected, and it suddenly drops below 0.1 level after the middle section of the draft tube.

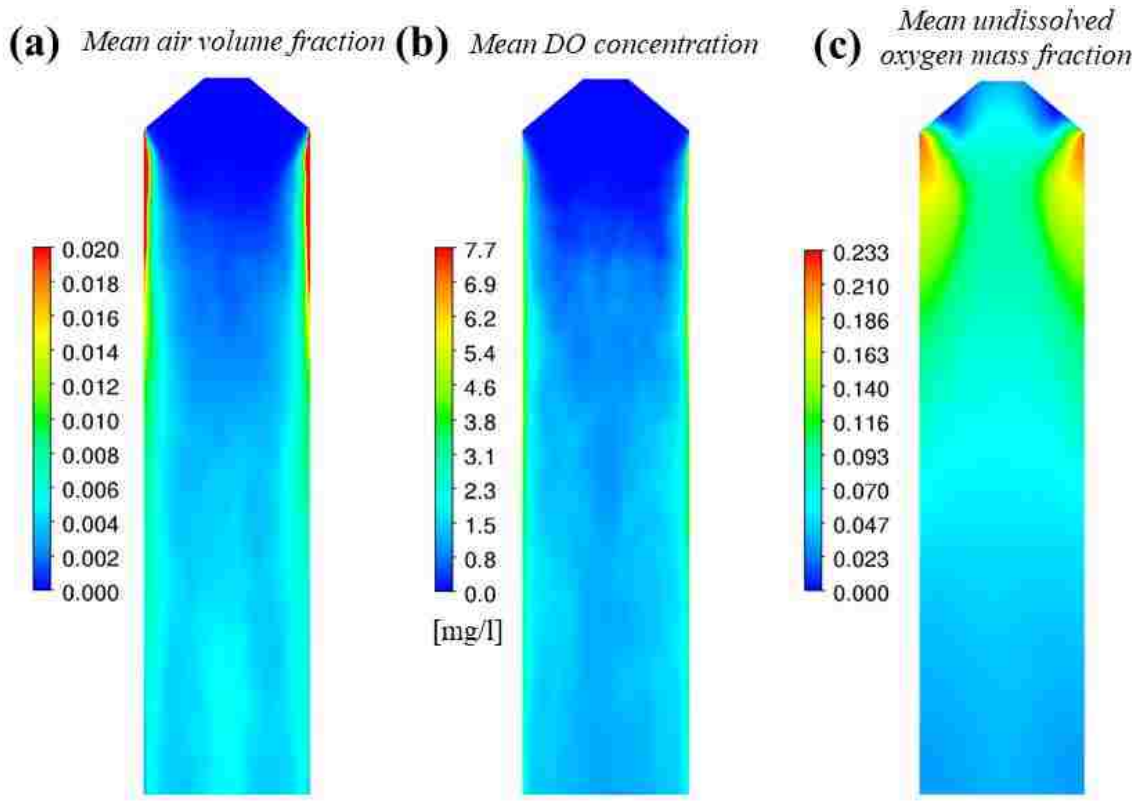

Figure 43. Time-averaged contours of (a) air volume fraction, (b) dissolved oxygen concentration, and (c) undissolved oxygen mass fraction from discrete surface draft tube aeration case.

The oxygen dissolution efficiency and volume-averaged dissolved oxygen concentration inside the draft tube is illustrated in Figure 44 as a function of the runner revolution. The dissolution efficiency is determined as the ratio between the amount of the dissolved oxygen and the total oxygen inside the draft tube. The amount of total oxygen consists of the dissolved oxygen and undissolved oxygen which is in air. The simulations are conducted until nearly asymptotic value of the efficiency is reached. In order to reveal the exact plateau value of the mean dissolved oxygen concentration, the simulations should be performed for a longer flow time. However, due to the limitation of the computational resources, the simulations are conducted for ten revolutions. The similar dissolution

efficiency signature is predicted by both continuous and discrete aeration. The mean DO concentration signature of the discrete surface aeration follows nearly the same pattern with the continuous surface aeration with a slight deviation. The deviation reduces further 9 revolutions and after and the level of the mean DO concentration becomes almost identical after 10 revolutions. The dissolution efficiency and mean DO concentration level are 25% and 1.4 mg/l for the central aeration, as presented in the chapter 5. Here, both the continuous and discrete surface DT aeration resulted in 80% dissolution efficiency and 1.8 mg/l mean dissolved oxygen concentration inside the draft tube.

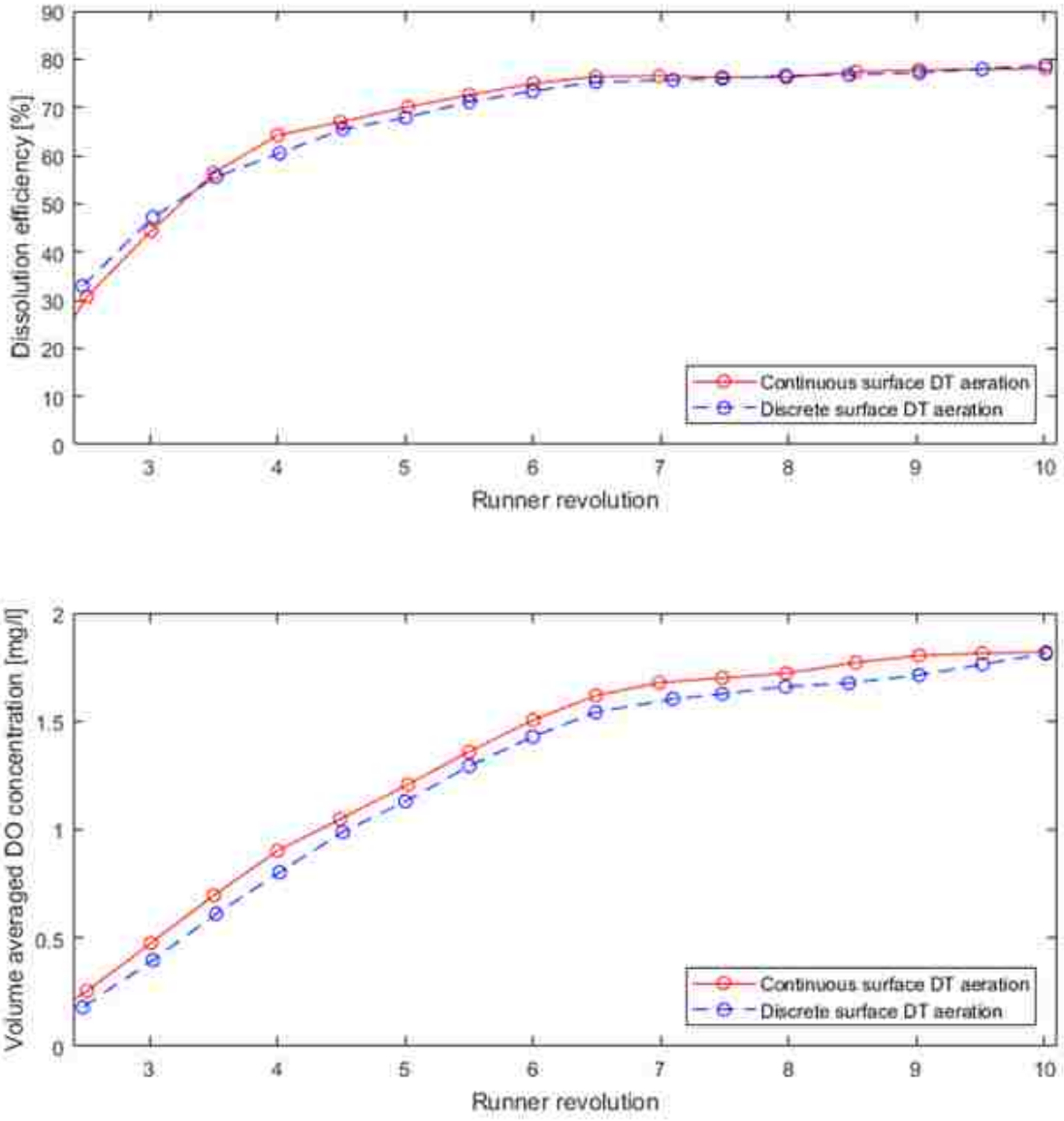

Figure 44. Dissolution efficiency (top) and volume-averaged dissolved oxygen concentration (bottom) inside the draft tube for both continuous and discrete draft tube aeration.

The mean DO concentration and the asymptotic value of the dissolution efficiency are calculated for the central and the peripheral aeration and are tabulated in Table 9. The dissolution efficiency improved 3.2 times with the peripheral aeration from the draft tube as compared to the central aeration. The mean DO concentration level is increased more

than 30% with the draft tube aeration. One of the reason of the increased dissolved oxygen level and the dissolution efficiency is the air is injected to the higher pressure region and stay in the higher pressure region after injection for the peripheral draft tube aeration. As illustrated in Figure 40(b), the lowest pressure is observed in the central region while the highest pressure is obtained near the draft tube surface. In central aeration, air is concentrated in the central region where the pressure level is low, see Figure 33(b). However, the air moves near the draft tube surface for the draft tube aeration, see Figure 41(b). The equilibrium level of oxygen concentration in the liquid phase increases as the pressure is increased (see Eqs. (23)-(25)). The higher level of equilibrium oxygen concentration yields the higher driving force for the mass transfer from air to water. Another reason might be the higher vortical activities inside the boundary layer attached to the draft tube surface and more intense swirling flows near the draft tube surface induce more mixing and in turn improves the mass transfer and dissolution of oxygen . Therefore, it is expected to observe larger amount of dissolved oxygen with draft tube aeration.

Table 9. Performance comparison for different cases.

Case	Power generated	Mean DO	Dissolution eff.
No aeration	57.04	-	-
Central aeration	55.11	1.4	25
Continuous DT aeration	54.86	1.8	80
Discrete DT aeration	55.20	1.8	80

The influence of the aeration on the power generation is also listed in Table 9. The power generation is predicted to be similar with different aeration cases. There is roughly

3.5% reduction in the turbine power performance when the aeration is applied. The signature of pump-turbine power generation for continuous and discrete draft tube aeration is illustrated as a function of the runner revolution in Figure 45. The similar trend is obtained for the power signature with both draft tube aeration methods. The results reveal that 10 revolutions are not sufficient to obtain an accurate nominal value for the power generation. However, there is only a slight increase in the power after 5 revolutions. As the simulations conducted further revolutions, the power would be closer to the power generation without the aeration, hence the penalty due to the aeration on the turbine power generation would be smaller than what is reported here.

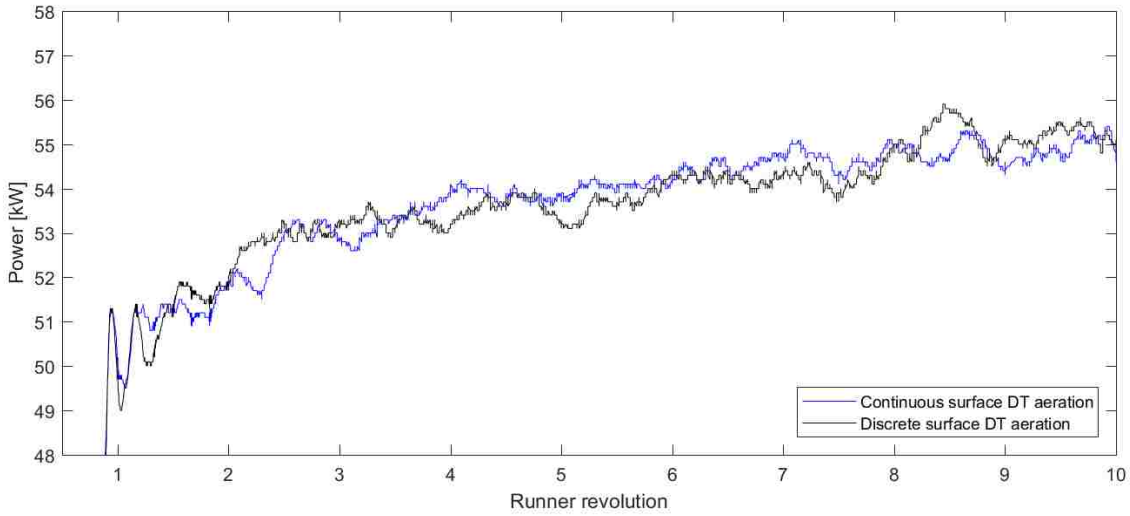

Figure 45. Power signature as a function of runner revolution for both continuous and discrete draft tube aeration.

In addition to the treating wastewater through the aeration, air injection can also lead to more stable operating condition for the pump-turbine system by reducing the flow induced vibration. The pressure signals are acquired at two locations on draft tube surface during the last 5 runner revolutions. The location of the pressure probes is illustrated in

Figure 46. Figure 47 and Figure 48 illustrates $(P - P_{mean})/\rho gH$ as a function of the turbine revolution at point 'a1' and 'a2', respectively for cases with and without aeration. The head of the pump-turbine system is represented by *H*. The pulsation level is significantly reduced by each aeration methods as compared to no aeration case. The time signature of $(P - P_{mean})/\rho gH$ shows more regular behavior with the central aeration compared to the other aeration configurations. The fluctuations vary around the same time averaged value consistently within the central aeration. The fluctuation acquired at the point 'a2' is smoother than that at the point 'a1'. The point 'a1' is closer to the runner and hence the higher vortical activities and the more intense swirling flows exist around this point induce the more irregular and higher-level flow induced fluctuation in this region. The standard deviation ($\pm\sigma$) of pressure data at points 'a1' and 'a2' are listed in Table 10 with and without aeration. At point 'a1', the standard deviation is reduced 69% with central aeration, 54% with continuous surface draft tube aeration and 44% with discrete surface draft tube aeration.

Table 10. The standard deviation of pressure data at points 'a1' and 'a2' for all cases.

Point	No aeration	Central Aeration	Continuous DT aeration	Discrete DT aeration
a1	0.062	0.019	0.029	0.035
a2	0.051	0.015	0.026	0.035

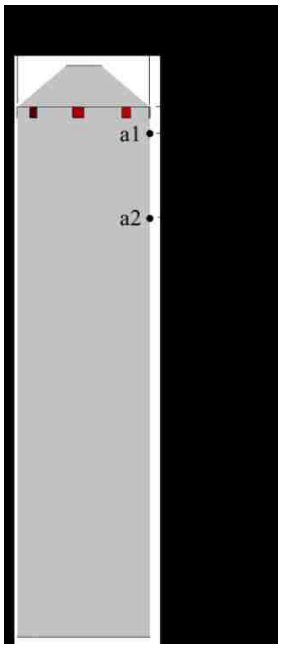

Figure 46. The location of points ‘a1’ and ‘a2’ where the pressure data is acquired.

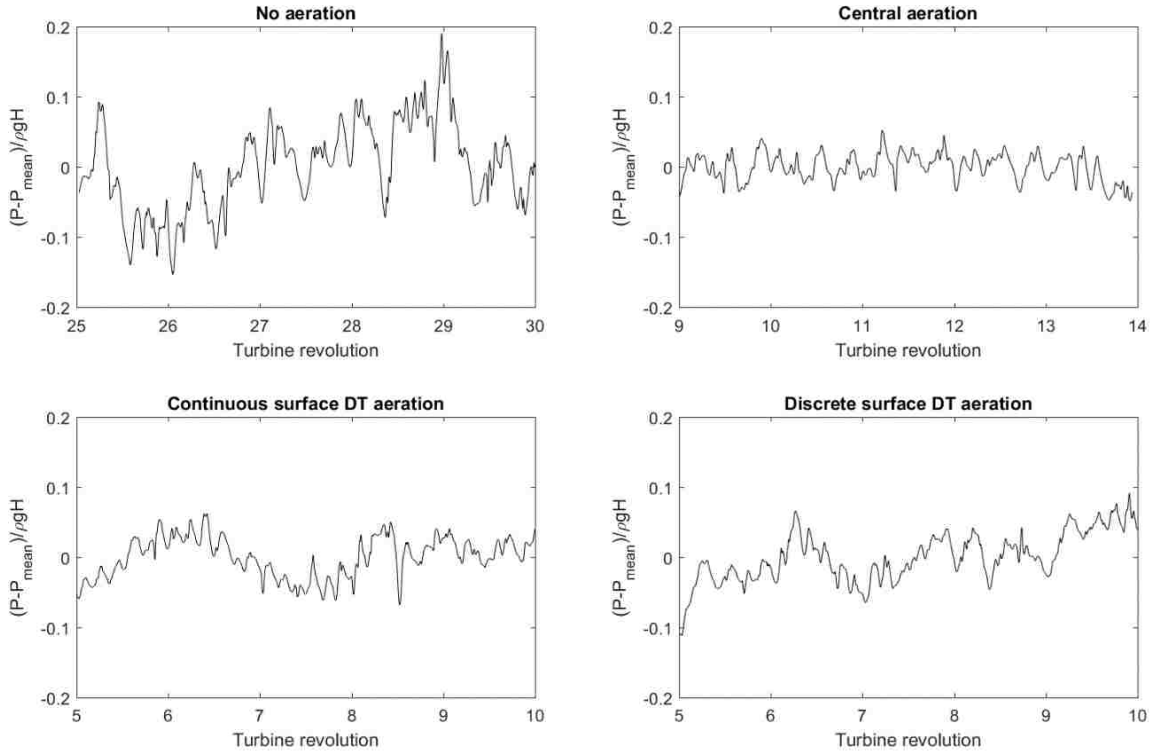

Figure 47. Pressure pulsation acquired at point ‘a1’ with (a) no aeration, (b) central aeration, (c) continuous surface draft tube aeration, and (d) discrete surface draft tube aeration.

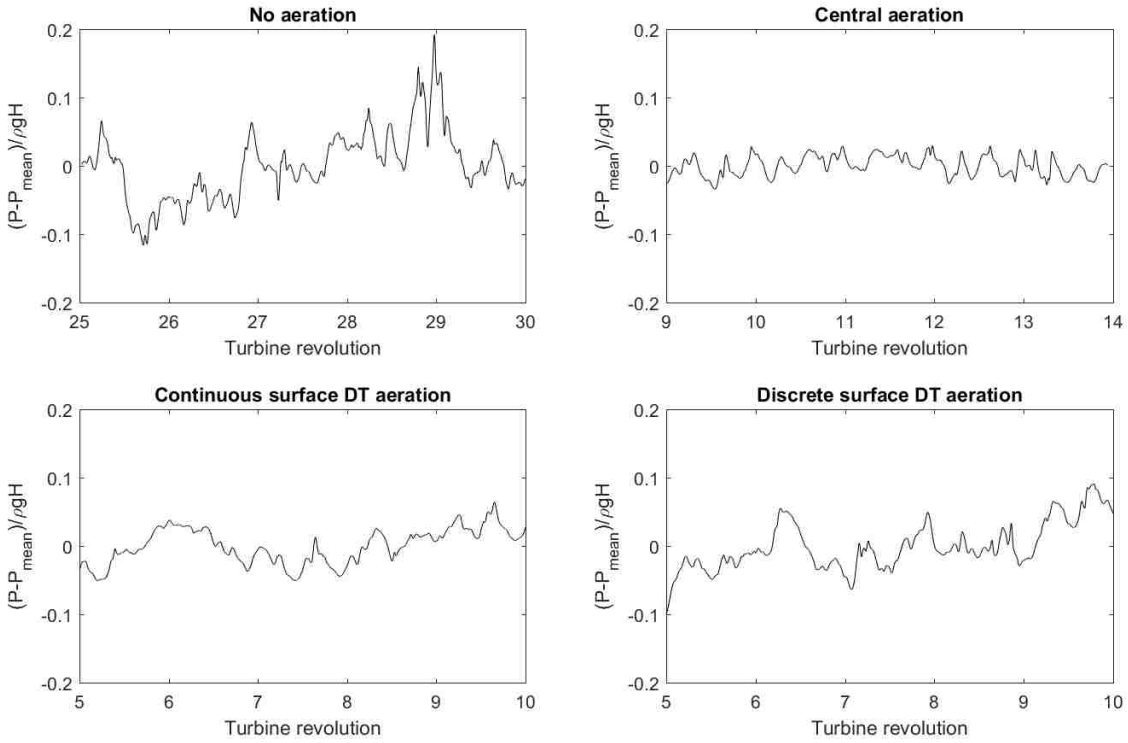

Figure 48. Pressure pulsation acquired at point ‘a2’ with (a) no aeration, (b) central aeration, (c) continuous surface draft tube aeration, and (d) discrete surface draft tube aeration.

Conclusion

Air was injected peripherally from the continuous ring and discrete surfaces near the draft tube inlet. Power generation, volume-averaged DO concentration and dissolution efficiency were predicted and compared against those predicted for the central aeration. Mixture multiphase model was employed to predict velocity field for each phase and the slip velocity between the phases. The plateau value of the dissolution efficiency and the mean DO concentration were predicted to be almost the same for both continuous and discrete surface draft tube aeration. The draft tube aeration resulted in 80% dissolution efficiency which is more than three times greater than that predicted with the central

aeration. The mean value of DO concentration inside the draft tube was computed to be 1.8 mg/l with the peripheral draft tube aeration which is 30% greater than that with the central aeration. The predicted amount of mean DO concentration with all three aeration configurations was sufficient for treating the wastewater. The influence of aeration on the power generation was almost the same with different aeration techniques. Aeration caused 3.5% penalty on the power generation of the unit. It was also demonstrated here that aeration reduces the flow induced fluctuations in the draft tube. The vibration of pump-turbine was reduced 69%, 54% and 44% with central, continuous surface draft tube, and discrete surface draft tube aeration, respectively.

CHAPTER 7 CONCLUSION

Large eddy simulations of ventilated micro-hydrokinetic turbine [67] and modular pump-turbine [76] were performed. Mixture multiphase model was employed to predict the velocity field of each phase. The oxygen dissolution model was validated by comparing numerical predictions in a bubble column against experimental measurements reported by Zhou et al. [5]. The parametric study was performed for flow past rectangular prism ventilated from top and bottom surfaces in a two-dimensional geometry to better understand the underlying physics of the dissolution process in these systems. The influence of aeration on power generation, flow induced vibration and oxygen dissolution was investigated. In bubbly flows, the Milelli condition should be considered carefully prior to the determination of the mesh size. For high fidelity LES simulations, small cell size is desired to capture the flow physics and the flow structures accurately, however, due to the cell size - bubble size restriction that comes from the Milelli condition, the mesh at each desired region cannot be refined.

The influence of interfacial forces, surface tension and bubble breakage and coalescence terms were investigated. The effects of non-drag interfacial forces including the lift force, the wall-lubrication force, and the turbulent dispersion force on the characteristics of the oxygen dissolution were negligible. Only the drag force was considered as an interfacial force in our simulations. The combined effects of the flow field and the mass transfer from air to water were proven to be effective in the prediction of bubble size. The breakage and coalescence terms has hardly changed the oxygen

dissolution characteristics. The mean drag coefficient and the dissolved oxygen concentration were hardly influenced by the surface tension.

The simulations of hydrokinetic turbine were conducted at the design and off design operating conditions at the tip-speed ratio of 1.86, 1.2, and 2.7. It was demonstrated that the aeration via hydrokinetic turbine can improve the water quality in river streams. Air was introduced to the downstream of the unit from the hub surface in the axial direction. The lower tip-speed ratio of 1.2 represents the wet seasons while the higher tip-speed ratio of 2.7 represents the dry seasons when the water velocity is lower. The turbine performance and dissolved oxygen distribution was predicted at each tip-speed ratio and compared with the single-phase predictions and the results obtained at other tip-speed ratios.

At the tip-speed ratio of 1.2, flow separation was observed from the blade edges. The flow separation, and more intense hub and root vortices observed at λ = 1.2 and λ = 1.86 improved the momentum mixing and resulted in the radial dispersion of air. The higher dissolution efficiency at λ = 1.2 and λ = 1.86 might be related to the presence of air in the radially expanded region of the wake.

The results obtained with and without the aeration were compared to reveal the influence of aeration. The aeration resulted in 1.9% reduction in the nominal value of power generation at λ = 1.2 and 1.6% and 3.1% improvement at λ = 1.86 and λ = 2.7, respectively. The aeration hardly influenced the nominal value of thrust for all three operating conditions. The standard deviation of power and thrust increased 56% and 47%, respectively, when the aeration is applied at λ = 1.2. However, the level of standard deviation after the aeration is still below the standard deviation obtained at λ = 1.86 and λ

= 2.7. At the design point, the fluctuation amplitude in the power and thrust reduced by 9% and 18%, respectively with the aeration. Similarly, at the tip-speed ratio of 2.7, 18% decrease was observed in the standard deviation of both performance parameters. During the design and higher tip-speed ratio operations, the blade tip vortices were dissipated earlier when the aeration was applied. The reduction in the standard deviation of power and thrust and the vortex suppression at λ = 1.86 and λ = 2.7 with aeration could translate as more stable turbine operation.

The central and two configurations of draft tube aeration methods were investigated at the design operating condition of the pump-turbine. Both single-phase and multiphase simulations were performed employing LES turbulence model. The volumetric flow rate of air was set to be 1% of the water flow rate. The air injection was applied during the turbine regime of the pump-turbine to provide required dissolved oxygen to the microorganisms which converts wastes into inorganic compounds. The aeration capability of the pump-turbine and the influence of aeration on the flow field, flow induced vibration, and power generation were evaluated.

The mean dissolved oxygen concentration inside the draft tube was computed to be 1.4 mg/l with the central aeration and 1.8 mg/l with both draft tube aerations. The dissolved oxygen level from 1.0 mg/l to 2.0 mg/l was reported to be sufficient for wastewater treatment [82]. It was demonstrated that the pump-turbine system studied here could be used effectively to treat the wastewater. The dissolution efficiency was calculated to be 25% with the central aeration and 80% with both draft tube aerations. Higher pressure, more intense vortical activities and swirling flows observed near the draft tube wall were

considered to be the primary reasons of better dissolution performance obtained with draft tube aeration. Moreover, the aeration caused 3.5% reduction in the pump-turbine power generation for all three aeration configurations.

Smaller eddies were observed in the single-phase flow as compared to multiphase flow with the central aeration. Air injection suppressed the vortical activities inside the draft tube. The time signature of pressure inside the draft tube revealed that the flow induced fluctuations was also reduced significantly with aeration. The vorticity suppression and the reduction in pressure fluctuation imply that aeration could aid in reducing vibration during the turbine operation. It must also be noted here that the higher level of dissolved oxygen was observed in regions with more intense vortical activities. This observation strongly suggests that momentum mixing promotes oxygen dissolution.

It is clearly detailed here that aeration can be applied for both hydrokinetic turbine and pump-turbine systems with minor penalty on system performance. The mathematical models and the numerical methods employed in this dissertation can be utilized to design and optimize ventilated turbines prior to costly experimental studies.

Future Work

The mathematical model employed here can be improved by calculating the bubble size with a higher fidelity inhomogeneous multiple size group (MUSIG) model. Here, the bubble size is predicted by solving single transport equation of interfacial area concentration including breakage and coalescence effects. In inhomogeneous MUSIG model, the dispersed secondary phase is divided into multiple size groups and the transport equation is solved for each size class by considering the mass transfer among the classes resulting from bubble breakage and coalescence effects. The forces applied on the bubble can vary based on the bubble size. Therefore, solving separate momentum equation for each size group might be required. In homogeneous form of the MUSIG model, there is only one velocity field for all size groups.

The equilibrium concentration of oxygen in the liquid phase is calculated based on the Henry's constant at 25 ℃ in this work. However, the temperature affects the equilibrium concentration significantly. For instance, as the temperature is reduced from 25 ℃ to 20 ℃ at 1 atm pressure, the equilibrium concentration of oxygen in water increases from 8.67 mg/l to 9.55 mg/l [55]. The temperature difference becomes significant for numerical simulations of ventilated Francis or Kaplan turbine when the dissolved oxygen concentration distribution in tailwater is desired to be predicted. Since the turbine intake is located at the deep regions of the reservoir where the temperature is relatively higher as compared to the temperature at the outlet of the turbine draft tube, there will be non-isothermal temperature distribution in the tailwater. In order to take the influence of temperature on oxygen dissolution, the van 't Hoff equation which describes the Henry

constant as a function of temperature can be employed and then the equilibrium concentration can be predicted locally inside the flow domain.

Distributed aeration technique which is not studied here can be applied for both hydrokinetic turbine and pump-turbine systems. In distributed aeration, lower static pressure on the blade trailing edge draws air from the atmosphere to the holes on the blade edge. Therefore, they are called auto-venting turbines and do not require additional power input for air injection. It is expected that the potential flow separation and highly turbulent flow near the blade trailing edges can improve the dissolution efficiency. Rohland et al. [83] reported that the distributed aeration is the most effective method to improve the oxygen dissolution and its influence on turbine efficiency is the lowest as compared to the central and the peripheral aeration. However, the refined mesh near the blade trailing edge may not comply with the Milelli condition. Further study addressing this issue should be performed as well.

APPENDIX

The UDF implemented into ANSYS-Fluent to calculate the volumetric mass transfer coefficient ($k_l \alpha_i$):

```
#include "udf.h"

#define D 1.9e-9     /* diffusivity of oxygen in water */
#define pi 3.14

DEFINE_MASS_TRANSFER(higbie, cell, thread, from_index,   from_species_index,
to_index, to_species_index) /* based on this line, the name of UDF is "higbie.c" */

{
real x_vel_g, x_vel_l, y_vel_g, y_vel_l, z_vel_g, z_vel_l, slip_x, slip_y, slip_z, mag_slip,
d, vof, kpq;

Thread *gas, *liq;
liq = THREAD_SUB_THREAD(thread, from_index);
gas = THREAD_SUB_THREAD(thread, to_index);
kpq = 0;     /* initialize vol. mass. tr. coeff. */

      /* CALCULATE VOLUMETRIC MASS TRANSFER COEFFICIENT */

x_vel_g = C_U(cell, gas);     /* gas vel. in x dir. */
y_vel_g = C_V(cell, gas);     /* gas vel. in y dir. */
z_vel_g = C_W(cell, gas);     /* gas vel. in z dir. */

x_vel_l = C_U(cell, liq);     /* liquid vel. in x dir. */
y_vel_l = C_V(cell, liq);     /* liquid vel. in y dir. */
z_vel_l = C_W(cell, liq);     /* liquid vel. in z dir. */

slip_x = x_vel_g - x_vel_l;   /* calculate slip vel. in x dir. */
slip_y = y_vel_g - y_vel_l;   /* calculate slip vel. in y dir. */
slip_z = z_vel_g - z_vel_l;   /* calculate slip vel. in z dir. */

mag_slip = sqrt(slip_x*slip_x + slip_y*slip_y + slip_z*slip_z);        /* magnitude of slip
vel. */

d = C_PHASE_DIAMETER(cell, gas);  /* bubble size */

vof = C_VOF(cell, gas);          /* gas phase volume fraction */
```

```
kpq = (vof)*6./(d)*2.*sqrt(D*mag_slip/d/pi); /* calculate vol. mass. tr. coeff. /*

return (kpq);
}
```

REFERENCES

[1] F. Bunea, D. M. Bucur, G. D. Ciocan and G. Dunca, "Aeration solution of water used by hydraulic turbines to respect the environmental policies," in *International Conference and Exposition on Electrical and Power Engineering (EPE)*, Iasi, Romania, 2014.

[2] P. March and P. Jacobson, "Industry experience with aerating turbines," in *HydroVision International 2015*, Oregon, USA, 2015.

[3] EPA, "Primer for municipal wastewater treatment systems," Document No. EPA 832-R-04-001, Washington, D.C., 2004.

[4] X. Jia, Q. Yuan, J. Wen and W. Feng, "Fluid flow modeling of a gas-induced pulsating flow bubble column," *Chemical and Biochemical Engineering Quarterly*, vol. 25, no. 1, pp. 27-36, 2011.

[5] Z. Zhou, Q. Yuan, X. Jia, W. Feng and J. Wen, "Experimental study and CFD simulation of mass transfer characteristics of a gas-induced pulsating flow bubble column," *Chemical and Biochemical Engineering Quarterly*, vol. 27, no. 2, pp. 167-175, 2013.

[6] K. Akita and F. Yoshida, "Bubble size, interfacial area, and liquid-phase mass transfer coefficient in bubble columns," *Industrial & Engineering Chemistry Process Design and Development*, vol. 13, no. 1, pp. 84-91, 1974.

[7] F. Kerdouss, A. Bannari and P. Proulx, "CFD modeling of gas dispersion and bubble size in a double turbine stirred tank," *Chemical Engineering Science*, vol. 61, no. 10, pp. 3313-3322, 2006.

[8] J. Min, Y. Bao, L. Chen, Z. Gao and J. M. Smith, "Numerical simulation of gas dispersion in an aerated stirred reactor with multiple impellers," *Industrial & Engineering Chemistry Research*, vol. 47, no. 18, pp. 7112-7117, 2008.

[9] A. Karn, S. Shao, R. E. Arndt and J. Hong, "Bubble coalescence and breakup in turbulent bubbly wake of a ventilated hydrofoil," *Experimental Thermal and Fluid Science*, vol. 70, pp. 397-407, 2016.

[10] A. Karn, C. R. Ellis, C. Milliren, J. Hong, D. Scott, R. E. Arndt and J. S. Gulliver, "Bubble size characteristics in the wake of ventilated hydrofoils with two

aeration configurations," *International Journal of Fluid Machinery and Systems,* vol. 8, no. 2, pp. 73-83, 2015.

[11] A. Karn, G. M. Monson, C. R. Ellis, J. Hong, R. E. Arndt and J. S. Gulliver, "Mass transfer studies across ventilated hydrofoils: A step towards hydroturbine aeration," *International Journal of Heat and Mass Transfer,* vol. 87, pp. 512-520, 2015.

[12] A. Karn, C. Ellis, J. Hong and R. E. Arndt, "Investigations into the turbulent bubbly wake of a ventilated hydrofoil: Moving toward improved turbine aeration techniques," *Experimental Thermal and Fluid Science,* vol. 64, pp. 186-195, 2015.

[13] P. A. March and R. K. Fisher, "It's not easy being green: Environmental technologies enhance conventional hydropower's role in sustainable development," *Annual Review of Energy and the Environment,* vol. 24, no. 1, pp. 173-188, 1999.

[14] P. March, "Hydraulic and environmental performance of aerating turbine technologies," in *EPRI Conference on Environmentally Enhanced Hydropower Turbines*, 2011.

[15] E. D. Harshbarger, B. Herrold, G. Robbing and J. C. Carter, "Turbine Venting for Dissolved Oxygen Improvements at Bull Shoals, Norfork, and Table Rock Dams," in *Waterpower'99: Hydro's Future: Technology, Markets, and Policy*, 1999.

[16] L. B. Moore, "Increasing Dissolved Oxygen with a Draft Tube Aeration System," *Hydro Review*, pp. 32-38, 2009.

[17] B. Papillon, M. Sabourin, M. Couston and C. Deschenes, "Methods for air admission in hydro turbines," in *21st IAHR Symposium on Hydraulic Machinery and Systems*, Lausanne, Switzerland, September, 2002.

[18] W. Water Environment Federation, Design of Municipal Wastewater Treatment, 4 ed., vol. 2, Alexandria, Virginia, 1998.

[19] E. Environmental Protection Agency, "Wastewater Technology Fact Sheet Oxidation Ditches," Washington, D.C., 2000.

[20] K. H. Hong, C. D., H. J. M. and S. B. Han, "Novel phased isolation ditch system for enhanced nutrient removal and its optimal operating strategy," *Journal of*

Environmental Science and Health, Part A, vol. 38, no. 10, pp. 2179-2189, 2003.

[21] Y. Yang, J. Yang, J. Zuo, Y. Li, S. He, X. Yang and K. Zhang, "Study on two operating conditions of a full-scale oxidation ditch for optimization of energy consumption and effluent quality by using CFD model," *Water research,* vol. 45, no. 11, pp. 3439-3452, 2011.

[22] V. Turkmenoglu, "The vortex effect of Francis turbine in electric power generation," *Turkish Journal of Electrical Engineering and Computer Science,* vol. 21, no. 1, pp. 26-37, 2014.

[23] K. Nakanishi and T. Ueda, "Air supply into draft tube of Francis turbine," *Fuji Electric Rev,* vol. 10, no. 3, pp. 81-91, 1964.

[24] A. Yu, X. W. Luo and B. Ji, "Numerical simulation and analysis of the internal flow in a Francis turbine with air admission," in *IOP Conference Series: Materials Science and Engineering*, 2015.

[25] Z. D. Qian, J. D. Yang and W. X. Huai, "Numerical simulation and analysis of pressure pulsation in Francis hydraulic turbine with air admission," *Journal of Hydrodynamics, Ser. B,* vol. 19, no. 4, pp. 467-472, 2007.

[26] F. R. Menter, "Zonal two-equation k-ω turbulence models for aerodynamic flows," *AIAA Paper 93-2906.*

[27] F. R. Menter, "Two-equation eddy-viscosity turbulence models for engineering," *AIAA journal,* vol. 32, no. 8, pp. 1598-1605, 1994.

[28] "ANSYS Fluent theory guide release 15.0," ANSYS, Inc., Canonsburg, 2013.

[29] J. O. Hinze, Turbulence, New York: McGraw-Hill Publishing Co., 1975.

[30] D. C. Wilcox, Turbulence modeling for CFD, La Canada, California: DCW Industries, Inc., 2010.

[31] F. Nicoud and F. Ducros, "Subgrid-scale stress modelling based on the square of the velocity gradient tensor," *Flow, Turbulence and Combustion,* vol. 62, no. 3, pp. 183-200, 1999.

[32] A. Tomiyama, "Struggle with computational bubble dynamics," in *Third International Conference on Multiphase Flow*, Lyon, France, 1998.

[33] T. Frank, J. Shi and A. D. Burns, "Validation of Eulerian multiphase flow models for nuclear safety applications," in *Third International Symposium on Two-Phase Flow Modeling and Experimentation*, Pisa, Italy, 2004.

[34] S. P. Antal, R. T. Lahey and J. E. Flaherty, "Analysis of phase distribution in fully developed laminar bubbly two-phase flow," *International Journal of Multiphase Flow,* vol. 17, no. 5, pp. 635-652, 1991.

[35] M. L. De Bertodano, "Turbulent bubbly flow in a triangular duct," Troy, New York, 1991.

[36] L. Schiller and Z. Naumann, "A drag coefficient correlation," *Z Ver Deutsch Ing,* vol. 77, p. 318, 1935.

[37] M. Manninen, V. Taivassalo and S. Kallio, "On the mixture model for multiphase flow," VTT Publications 288, 1996.

[38] "ANSYS Fluent theory guide release 15.0," ANSYS, Inc., Canonsburg, PA, 2013.

[39] T. Hibiki and M. Ishii, "One-group interfacial area transport of bubbly flows in vertical round tubes," *International Journal of Heat and Mass Transfer,* vol. 43, no. 15, pp. 2711-2726, 2000.

[40] Q. Wu, S. Kim, M. Ishii and B. S. G., "One-group interfacial area transport in vertical bubbly flow," *International Journal of Heat and Mass Transfer,* vol. 41, no. 8-9, pp. 1103-1112, 1998.

[41] M. Ishii and S. Kim, "Micro four-sensor probe measurement of interfacial area transport for bubbly flow in round pipes," *Nuclear engineering and design,* vol. 205, no. 1, pp. 123-131, 2001.

[42] M. J. Prince and H. W. Blanch, "Bubble coalescence and break-up in air-sparged bubble columns," *AIChE Journal,* vol. 36, no. 10, pp. 1485-1499, 1990.

[43] D. Hillel, Environmental soil physics: Fundamentals, applications, and environmental considerations, Academic press, 1998.

[44] W. G. Whitman, "A preliminary experimental confirmation of the two-film theory of gas absorption," *Chemical and Metallurgical Engineering,* vol. 29, no. 4, pp. 146-148, 1923.

[45] P. S. Liss, "Processes of gas exchange across an air-water interface," *In Deep Sea Research and Oceanographic Abstracts,* vol. 20, no. 3, pp. 221-238, 1973.

[46] S. D. Faust and O. M. Aly, Chemistry of water treatment, CRC Press, 1998.

[47] R. Higbie, "The rate of absorption of a pure gas into still liquid during short periods of exposure," *Transactions of the American Institude of Chemical Engineers,* vol. 35, pp. 365-389, 1935.

[48] P. V. Danckwerts, "Significance of liquid-film coefficients in gas absorption," *Industrial and Engineering Chemistry,* vol. 43, pp. 1460-1467, 1951.

[49] P. Ranganathan and S. Sivaraman, "Investigations on hydrodynamics and mass transfer in gas–liquid stirred reactor using computational fluid dynamics," *Chemical engineering science,* vol. 66, no. 14, pp. 3108-3124, 2011.

[50] S. S. Alves, C. I. Maia and J. M. T. Vasconcelos, "Gas-liquid mass transfer coefficient in stirred tanks interpreted through bubble contamination kinetics," *Chemical Engineering and Processing: Process Intensification,* vol. 43, no. 7, pp. 823-830, 2004.

[51] J. C. Lamont and D. S. Scott, "An eddy cell model of mass transfer into the surface of a turbulent liquid," *AIChE Journal,* vol. 16, no. 4, pp. 513-519, 1970.

[52] J. Gimbun, C. D. Rielly and Z. K. Nagy, "Modelling of mass transfer in gas–liquid stirred tanks agitated by Rushton turbine and CD-6 impeller: a scale-up study," *Chemical Engineering Research and Design,* vol. 87, no. 4, pp. 437-451, 2009.

[53] P. Calderbank, Gas absorption from bubbles, Chemical Engineering CE2 09, 1957.

[54] C. Daskiran, I. -H. Liu and A. Oztekin, "Computational study of multiphase flows over ventilated translating blades," *International Journal of Heat and Mass Transfer,* vol. 110, pp. 262-275, 2017.

[55] R. Sander, "Compilation of Henry's law constants (version 4.0) for water as solvent," *Atmospheric Chemistry & Physics,* vol. 15, no. 8, p. 4399–4981, 2015.

[56] J. W. Lengeler, G. Drews and H. G. Schlegel, Biology of the Prokaryotes, Georg Thieme Verlag, 1999.

[57] C. E. Boyd, Water quality: an introduction, Springer, 2015.

[58] T. Miyahara, Y. Matsuba and T. Takahashi, "The size of bubbles generated from perforated plates," *International Chemical Engineering,* vol. 23, pp. 517-523, 1983.

[59] M. Milelli, B. L. Smith and D. Lakehal, "Large-eddy simulation of turbulent shear flows laden with bubbles," in *Direct and Large-Eddy Simulation IV*, 2001, pp. 461-470.

[60] D. Law, F. Battaglia and T. J. Heindel, "Numerical simulations of gas-liquid flow dynamics in bubble columns," in *ASME 2006 International Mechanical Engineering Congress and Exposition*, Chicago, IIIinois, 2006.

[61] J. U. Brackbill, D. B. Kothe and C. Zemach, "A continuum method for modeling surface tension," *Journal of computational physics,* vol. 100, no. 2, pp. 335-354, 1992.

[62] I. -H. Liu, B. Attiya and A. Oztekin, "Transient flows past arrays of yawed finite plates," *Canadian Journal of Physics (Under Review),* 2017.

[63] G. C. Layek, C. Midya and A. S. Gupta, "Influences of suction and blowing on vortex shedding behind a square cylinder in a channel," *International Journal of Non-Linear Mechanics,* vol. 43, no. 9, pp. 979-984, 2008.

[64] A. K. Saha and A. Shrivastava, "Suppression of vortex shedding around a square cylinder using blowing," *Sadhana,* vol. 40, no. 3, pp. 769-785, 2015.

[65] J. C. Hunt, A. A. Wray and P. Moin, "Eddies, streams, and convergence zones in turbulent flows," in *Proceedings of the Summer Program, Center for Turbulence Research,* 1988.

[66] W. Schleicher, J. Riglin, A. Oztekin and R. Klein, "Numerical optimization of a portable hydrokinetic turbine," in *Proceedings of the 2nd Marine Energy Technology Symposium,* Seattle, WA, 2014.

[67] W. C. Schleicher, J. D. Riglin and A. Oztekin, "Numerical characterization of a preliminary portable micro-hydrokinetic turbine rotor design," *Renewable Energy,* vol. 76, pp. 234-241, 2015.

[68] S. Kang, X. Yang and F. Sotiropoulos, "n the onset of wake meandering for an axial flow turbine in a turbulent open channel flow," *Journal of Fluid Mechanics,* vol. 744, pp. 376-403, 2014.

[69] C. Santoni, K. Carrasquillo, I. Arenas-Navarro and S. Leonardi, "Effect of tower and nacelle on the flow past a wind turbine," *Wind Energy,* vol. 20, no. 12, pp. 1927-1939, 2017.

[70] J. Riglin, C. Daskiran, J. Jonas, W. C. Schleicher and A. Oztekin, "Hydrokinetic turbine array characteristics for river applications and spatially restricted flows," *Renewable Energy,* vol. 97, pp. 274-283, 2016.

[71] S. Kang, I. Borazjani, J. A. Colby and F. Sotiropoulos, "Numerical simulation of 3D flow past a real-life marine hydrokinetic turbine," *Advances in water resources,* vol. 39, pp. 33-43, 2012.

[72] L. P. Chamorro, C. Hill, S. Morton, C. Ellis, R. E. A. Arndt and F. Sotiropoulos, "On the interaction between a turbulent open channel flow and an axial-flow turbine," *Journal of Fluid Mechanics,* vol. 716, pp. 658-670, 2013.

[73] L. P. Chamorro, C. Hill, V. S. Neary, B. Gunawan, R. E. A. Arndt and F. Sotiropoulos, "Effects of energetic coherent motions on the power and wake of an axial-flow turbine," *Physics of Fluids,* vol. 27, no. 5, p. 055104, 2015.

[74] C. Daskiran, J. Riglin, W. Schleicher and A. Oztekin, "Transient analysis of micro-hydrokinetic turbines for river applications," *Ocean Engineering,* vol. 129, pp. 291-300, 2017.

[75] C. Daskiran, J. Riglin, W. C. Schleicher and A. Oztekin, "Computational study of aeration for wastewater treatment via ventilated pump-turbine," *International Journal of Heat and Fluid Flow,* vol. 69, pp. 43-54, 2018.

[76] W. C. Schleicher and A. Oztekin, "Hydraulic design and optimization of a modular pump-turbine runner," *Energy Conversion and Management,* vol. 93, pp. 388-398, 2015.

[77] F. Bunea, G. D. Ciocan, G. Oprina, G. Băran and C. A. Băbuţanu, "Hydropower impact on water quality," *Environmental Engineering and Management Journal,* vol. 9, no. 11, pp. 1459-1464, 2010.

[78] X. Gong, S. Takagi and Y. Matsumoto, "The effect of bubble-induced liquid flow on mass transfer in bubble plumes," *International Journal of Multiphase Flow,* vol. 35, no. 2, pp. 155-162, 2009.

[79] International Electrotechnical Commission, Hydraulic turbines, storage pumps and pump-turbines—model acceptance tests, 2nd edition ed., 1999.

[80] J. Anderson, Computational fluid dynamics: the basics with applications., McGraw Hill International, 1995.

[81] N. Kolekar and A. Banerjee, "Performance characterization and placement of a marine hydrokinetic turbine in a tidal channel under boundary proximity and blockage effects," *Applied Energy,* vol. 148, pp. 121-133, 2015.

[82] N. F. Gray, Biology of wastewater treatment, London, U.K.: Imperial College Press, 2004.

[83] K. M. Rohland, J. M. Foust, G. D. Lewis and J. C. Sigmon, "Equipment: Aerating turbines for duke energy's new bridgewater powerhouse," *Hydro Review,* vol. 29, no. 3, p. 58, 2010.

Vita

Cosan Daskiran was born in Zonguldak, Turkey on March 22, 1990. His father is Erol Daskiran, mother is Aynur Daskiran and sister is Merve Daskiran. After attended Zonguldak Ataturk Anatolian High School, he entered mechanical engineering department of Istanbul Technical University. He received his Bachelor of Science degree in Mechanical Engineering in February 2012. After that, he enrolled Lehigh University in August 2013 and completed his Master of Science under his advisor Dr. Alparslan Oztekin in May 2016 with a 3.96 grade point average. In November 25th, 2014, he got married with Burcu Daskiran.

Cosan then continued for his doctorate studies at Lehigh University under his advisor Dr. Alparslan Oztekin and worked for multiphase simulations of ventilated micro-hydrokinetic turbine and pump-turbine. He has successfully defended his dissertation and graduated with the degree Doctor of Philosophy in Mechanical Engineering on August 1st, 2018.